

VUV Spectroscopy of Atoms, Molecules and Surfaces

Merete K. Raarup

Institute of Physics and Astronomy
Aarhus University, Denmark

August 2001

Contents

Preface	iii
1 VUV light generation: possibilities and limitations	1
1.1 Introduction	1
1.2 Frequency mixing	4
1.3 High-harmonic generation	6
1.4 Comparison with other methods of VUV light- and X-ray generation	13
2 Negative ions	23
2.1 Introduction	23
2.2 Negative-ion structure	24
2.3 Status on negative-ion knowledge	26
2.4 Theoretical approaches to negative-ion structure	29
2.4.1 Computational methods	29
2.4.2 The hyperspherical-coordinate approach	32
3 High-resolution VUV spectroscopy of H⁻	43
3.1 Introduction	43
3.2 Experimental approach	46
3.3 Results and discussion	50
3.4 Conclusion	56
4 Lifetimes of molecular negative ions	61
4.1 Introduction	61
4.2 Notation and molecular quantum numbers	63
4.3 Experimental setup	64
4.4 N ₂ ⁻	65
4.5 CO ₂ ⁻	68

4.6	Conclusion	74
5	Femtosecond VUV core-level spectroscopy of surface dynamics	79
5.1	Introduction	79
5.2	Laser-induced desorption	82
5.2.1	The adsorbate-substrate bond	83
5.2.2	Direct laser-induced desorption	83
5.2.3	Substrate-mediated laser-induced desorption	86
5.3	The technique of core-level spectroscopy	89
5.4	Core-level spectroscopic tests at ASTRID	93
5.4.1	Experimental setup	93
5.4.2	CO/Pt(111)	95
5.4.3	Oxidation of Al(111)	98
5.5	The VUV light source of high-order harmonics	105
5.6	Future prospects	113
6	Two-colour pump-probe experiments on He using high-order harmonics	127
6.1	Introduction	127
6.2	Experimental approach	131
6.3	Results and discussion	134
6.3.1	Lifetime measurements and the role of the spike	134
6.3.2	Photoionization cross-section measurements	139
6.4	Conclusion	141
	Summary	147

Preface

The present thesis, submitted to the Faculty of Natural Sciences, describes the experiments in which I have been involved during four years of Ph.D. studies at the Institute of Physics and Astronomy, Aarhus University. The experiments have been performed partly in the negative-ion group of Professor Torkild Andersen and partly in the combined femto- and surface physics group of Peter Balling which was started when I initiated my Ph.D studies. Being a part of a new group has given me a unique opportunity of being closely involved in the construction and establishment of a new laboratory with all the technical, financial and political considerations making up such a puzzle.

A common theme of the thesis are the spectroscopic investigations of the structure and dynamics of atoms and molecules in the gas phase and at surfaces. Most of the studies have been performed with light in the vacuum-ultraviolet (VUV) part of the electromagnetic spectrum on energy levels where the amount of relevant new information that can be obtained requires the time- or frequency resolution to be pushed to the limit of present capability. Chapter 1 presents an overview of the current possibilities and limitations in VUV and X-ray spectroscopy and, intervening with this, methods for the generation of light in this wavelength range.

The following three chapters deal with spectroscopy of negative ions, starting with a general introduction and overview in chapter 2. The field of negative ions has matured significantly within the last decade, but much work still needs to be done if a satisfactory description of such systems is to be obtained. An important example is the intensively studied H^- ion whose existence relies on electron correlation. An experimental technique for Doppler-tuned VUV spectroscopy of high-lying doubly-excited states of H^- with unprecedented spectral resolution has previously been implemented at the storage ring ASTRID. A description of the experiments performed with an improved energy resolution obtained by the application of electron cooling is given in chapter 3.

Experimental and theoretical studies have mainly concentrated on atomic negative ions with the knowledge about molecular negative ions lacking behind. The electronic structure of a neutral molecule can be predicted with much less accuracy than that of a neutral atom due to the lack of spherical symmetry, and proceeding to molecular negative ions implies further difficulties. Previous successful studies of autodetachment lifetimes of atomic negative ions at ASTRID have therefore been extended to measurements on molecular negative ions, as outlined in chapter 4.

Dynamical processes like phase transitions and chemical reactions proceed on the atomic level on a femtosecond timescale. Femtosecond laser pulses provide the time resolution required to follow such processes but only indirect information about the structural changes can be obtained with the visible laser light available at present. A femtosecond X-ray source would allow such processes to be followed on the atomic level in time as well as in space and a large effort is at present directed towards this goal. A promising approach is that of high-harmonic generation which will be used in the experiment described in chapter 5 for femtosecond time-resolved VUV core-level spectroscopy of dynamical processes at surfaces.

Finally, chapter 6 is devoted to a study of the radiative lifetime of the $1s2p$ state of He in a pump-probe experiment, using picosecond VUV high-order harmonics to populate the state which is subsequently ionized with an optical laser pulse. The focus is not on the already well-known lifetime but on some coherent effects present under certain experimental conditions. In addition, the feasibility of using the technique for photoionization cross-section measurements on excited states is investigated.

Acknowledgements

In the course of my Ph.D. studies I have had the pleasure of becoming acquainted with a broad range of disciplines within atomic- and surface physics, working in an "ordinary" laboratory with my "own" setup as well as at our storage ring ASTRID during beam times with ions as well as synchrotron radiation. My first experimental experience, during the fall of 1997, was obtained by synchronizing the pulses from an old picosecond Nd:YAlG laser with the synchrotron-radiation pulses from ASTRID. Peter and I then attempted to study laser-assisted core-level photoionization from an Al surface at the SGM I beamline at ASTRID, helpfully assisted by Jakob H. Pedersen. However, no matter how many dodges we made and—to Jakobs frustration—how hard we burned the surface, it was impossible to discriminate a single laser-induced event from the background.

After that event we decided to aim at high-order harmonics as a femtosecond VUV light source for our planned studies of surface dynamics. Awaiting the grant for a femtosecond laser, we made an attempt, together with Jon Merrison, to study multiphoton ionization of positronium with nanosecond laser pulses, eventually realizing that no positronium atoms could be generated by the applied method. By January 1999 we were lucky to receive the femtosecond laser system with a regenerative amplifier in addition to half the space of a laboratory, in which the system was installed and aligned from scratch. In the fall of 1999 Martin Hansen, Peter's first master student, started out trying to do femtosecond laser-induced desorption of CO molecules from a Cu surface mounted in an ultrahigh vacuum chamber donated by Erik Bøgh. In the mean time I spent three months at Lund Laser Center, Sweden, in the group of Professor Anne L'Huillier and Professor Claes-Göran Wahlström, learning about high-harmonic generation by participating in, e.g. the He-experiment described in chapter 6. In Lund I had a pleasant time in the laboratory with the company of Allan Johansson, Zhongshan Li, Vladimir Lokhnygin, Johan Mauritsson, Michael Meyer and Johan Norin.

In the spring of 2000 Martin and I made a final attempt to observe laser-induced desorption, but for some reason we never succeeded and we have many times agreed on the incapability of the laser system and the antique equipment. In addition, I finally finished fitting the H^- data recorded at ASTRID in May 1999 after almost two years of struggles at the half-yearly beamtimes to get the electron cooler work as intended. During these beam times I had the encouraging and experienced company of Henrik H. Andersen, Ulrik V. Pedersen and Victor V. Petrunin and, for our last beam time in November 2000, the additional company of our bachelor student Randi G. Mortensen with whom I did the preparations. Henrik in addition introduced

me to the principle of negative-ion lifetime measurements at ASTRID which was applied to CO_2^- and N_2^- during 1997–1998. All of these beam times would not have been possible without the assistance of the ring operators Niels Hertel, Jørgen S. Nielsen and Søren P. Møller.

In August 2000 Jakob S. Nielsen, our second bachelor student, and I generated the first high-order harmonics after Rune Lausten, Peter’s second master student, had finished an amplifier for the femtosecond laser system. The high-harmonic chamber and the other vacuum parts needed for the surface dynamics experiments were constructed by Vagn Toft and Henrik J. Jensen. Although Rune concentrated on a different project I have often benefitted from his (as opposed to mine) patience with the delicate laser system. In the fall of 2000 and the spring of 2001, I had my second encounter with the SGM I beamline, studying the CO/Pt and O/Al systems with Peter, helpfully assisted by the beamline operators Søren V. Hoffman and Zheshen Li. In the spring of 2001 Peter, Rune, Kasper Vestentoft—Peter’s third master student—and I finally moved into a new laboratory of our own and I finally got the time to test the multilayer mirrors that were made for the surface dynamics experiments by Jacques Chevallier (who had then been awaiting my opinion on his work for almost a year).

Thanks to all of you and to everybody else that I have interacted with at the institute; Karsten Rasmussen, Erik Søndergaard and the other people from the vacuum-, electronics- and computer departments, Torben Thomsen, Uffe Simonsen and the other people from the workshops—and I could continue. Thanks to Jan Thøgersen for proof reading the manuscript and to my friends, office mates, parents and—not least—my dogs Claire and Jackie for encouragement and support during good as well as bad times.

During all of these years Torkild and Peter have been there, pulling the strings and giving me all the encouragement, help and support that I could wish. Thanks for all this and for your tolerance and patience with my stupid questions and mistakes in the laboratory.

Finally, the financial support from the Aarhus Center of Advanced Physics (ACAP) is gratefully acknowledged.

List of publications

The thesis is based on the following publications:

Metastable state of CO_2^- with millisecond lifetime,
M. K. Raarup, H. H. Andersen and T. Andersen,
J. Phys. B **32**, L659 (1999).

Long-lived States of N_2^- : Formation, Lifetimes and Identity,
T. Andersen, K. A. Bertelsen, M. K. Raarup, N. Rud, J. Olsen and
L. Veseth,
Phys. Rev. A **60**, 3627 (1999).

*High-Resolution Vacuum-Ultraviolet Spectroscopy of an
Electron-Cooled D^- Beam,*
M. K. Raarup, U. V. Pedersen, V. V. Petrunin, P. Balling and
T. Andersen,
Phys. Rev. Lett. **85**, 4028 (2000).

*Two-photon, two-color resonant ionisation of He atoms using
high-order harmonics,*
A. Johansson, A. L'Huillier, Z. S. Li, V. Lokhnygin, M. Meyer,
M. K. Raarup and C.-G. Wahlström,
Manuscript in preparation for J. Phys. B

In addition, I have contributed to the following papers:

Electron cooling of D^- at the ASTRID storage ring,
J. S. Nielsen, S. P. Møller, L. H. Andersen, P. Balling and
M. K. Raarup,
Nucl. Inst. Meth. A **441**, 150 (2000).

*High-resolution VUV Spectroscopy of H^- in the Region near the
 $H(n=2)$ Threshold,*
P. Balling, H. H. Andersen, C. Brodie, V. V. Petrunin, M. K. Raarup,
P. Steiner and T. Andersen,
Phys. Rev. A **61**, 022702 (2000).

Chapter 1

VUV light generation: possibilities and limitations

1.1 Introduction

Investigating the structure and dynamics of atoms and molecules in the gas phase and in solids are major disciplines of atomic and condensed-matter physics. For an atom in the gas phase, the structure usually refers to the distribution of the stationary states in an energy-level diagram, reflecting the various possibilities for spatial arrangements of the electrons with respect to the nucleus. For a gas-phase molecule, in addition to these electronic levels there are also energy levels arising from the vibrational- and rotational motions of the individual atoms constituting the molecule. The latter are usually accessible with light in the infrared- and microwave parts of the electromagnetic spectrum, respectively, while the electronic levels, which are of main interest in the present context, can be reached with visible, ultraviolet (UV) or vacuum-ultraviolet (VUV) photons. While the energy-level diagram of an atom may be considered one-dimensional in the sense that the atom is spherical symmetric, the electronic energies of a molecule will depend on bond lengths and (possibly) bend angles and are depicted on a potential-energy curve or -surface. Considering the combined system of a molecule bound to a surface, this picture is carried on by introducing potential-energy surfaces for the interaction of the molecule with the surface. For a collection of atoms constituting a solid, the discrete electronic energy levels of the in-

dividual atoms are broadened into bands with the bands being more narrow the more tightly bound the electrons.

Associated with each electronic energy level (or band) is a spectral width or, equivalently, a lifetime, implying two ways of determining it: by scanning the energy spectrum with laser light of a comparatively narrower bandwidth, or by measuring the decay rate of the level using, e.g., laser pulses with a duration shorter than the lifetime. The decay of such energy levels is usually referred to as the dynamics of the system, and the two methods supplement and complement each other with the first being applicable to spectrally broad- (short-lived) and the latter to spectrally narrow (long-lived) energy levels. The lifetime of an energy level depends on the decay possibilities and is thus in general expected to decrease, the higher lying the level is. There are, however, significant deviations from this rule depending on the orbital- and spin angular momenta of the state and the selection rules governing its decay. The widths of atomic- and molecular electronic energy levels are typically in the μeV – meV range but may be much narrower, while the width of a core-hole in a solid is in the meV – eV range.

All of the above-mentioned energy levels could be called stationary in the sense that they are characteristic of an isolated or undisturbed system. For a molecule or a solid undergoing a dynamical, structural transition associated with re-arrangements of the atomic positions with respect to each other, the energy levels will change accordingly. Examples of structural dynamical transitions are the dissociation of a molecule following its excitation to a repulsive state, a chemical reaction or a solid-liquid phase transition. Structural dynamics proceeds on the atomic level on a femtosecond timescale, and information about the evolution of the intermediate state can only be obtained with a probe of comparable time resolution. Femtosecond lasers provide the time-resolution required to follow such processes, and the pump-probe technique where the reaction or transition of interest is initiated by a laser pulse (the pump) and after a time delay probed by another laser pulse is widely used. At present femtosecond lasers only generate light in the visible part of the spectrum which interacts with the valence electrons and only indirectly probes the atomic motion. For direct information about structural changes, i.e. the atomic positions, as a function of the time delay, shorter wavelength probes, ideally X-rays, are usually required. An exception is the pump-probe technique of Coulomb explosion applied to gas-phase chemical reactions where the (visible) probe pulse is sufficiently intense to induce multiple ionization of the molecule [1]. The Coulomb repulsion in the resulting positively charged system leads to dissociation, and by measuring the energies of the resulting fragments the molecular bond length at the time of presence of the probe laser pulse can be determined.

The studies presented in this thesis are concerned with the spectroscopic investigations of stationary, electronic states of gas-phase atoms and molecules (chapters 3, 4 and 6) in addition to the structural dynamical transitions of femto-second laser-excited molecules bound to solid surfaces (chapter 5). Obviously, the very large range of wavelengths, bandwidths and pulse durations spanned by these applications cannot be covered by a single light source. However, everything else equal, moving from the visible towards the VUV- or X-ray part of the spectrum imposes further limitations on desirable light-source properties such as tunability, bandwidth, pulse duration, pulse energy and coherence. Among the different techniques in use for generation of light in the UV-, VUV- or X-ray part of the spectrum, different variants of harmonic generation or frequency mixing have proven particularly useful in the UV and VUV, while other approaches have been attempted for the X-ray range as will be outlined below.

First, however, since the main focus of the thesis is on the application of VUV light for spectroscopy of high resolution in the time- and frequency domains, I would like to briefly discuss the present state of definitions on this subject. When it comes to the division of the electromagnetic spectrum into ranges of UV, VUV, XUV (eXtreme UltraViolet), soft X-rays and X-rays there is at present no clear-cut distinction as pointed out by Stark and Smith [2]. There is, however, more or less agreement among different encyclopaedia [2, 3, 4] that the range between 10 nm and 200 nm should be called the VUV or XUV, so I will let that region be my definition of VUV and then refer to the shorter- and larger wavelengths as X-rays and UV, respectively. At least the 200 nm boundary seems a reasonable choice since molecular oxygen becomes opaque at 185 nm, thus prohibiting light propagation in air below this wavelength [4]. A further division of the 10–200 nm range into regions of VUV and XUV separated by the ~ 120 nm limit for the performance of transmittive optics could be justified but will not be used here. The only attempt towards a definition of high frequency resolution, that I have been able to find, is one of Connerade, proposing that a resolving power higher than ~ 100 times the wavelength expressed in \AA should be regarded a high resolution [5]. This implies resolutions of $80 \mu\text{eV}$ and 8meV for 10eV and 100eV photons, respectively. The argument assumes wavelength selection by a spectrometer and is not applicable to the case of VUV light generation by frequency mixing of laser light, where the bandwidth may be much smaller [5]. Thus, for example, Eikema *et al.* have created 58.4nm light with a bandwidth of $3 \mu\text{eV}$ by frequency tripling the frequency-doubled 584nm amplified output from a continuous wave ring dye laser [6]. This is equal to the bandwidth of the nanosecond pulses from a state-of-the art dye laser operating in the visible. The above definition is certainly given with reference

to the current limitations to light generation since energy-level widths may be several order of magnitudes smaller. For example, the width of the $1s$ - $2s$ transition of the neutral hydrogen atom is 1.3 Hz (5×10^{-15} eV) and can be studied with at best a 1 kHz resolution [7]. Proceeding along these lines, and lacking a more intelligent proposal, I will define a high time resolution as one of a few femtoseconds since this is the shortest duration in use for practical applications at present [8]. With such short pulses it is possible to follow the motion of most atoms while the resolution of electronic motion will have to await a further development in the attosecond regime (see section 1.4).

1.2 Frequency mixing

The applicability of lasers has expanded tremendously since the observation in 1961 that sufficiently intense laser light passing through a non-linear crystal gave rise to the generation of light at twice the frequency of the incoming light [9]. Third- and fourth harmonic generation in crystals and higher orders in gases as well as sum- and difference frequency mixing of two laser beams of differing frequencies are now routine operations for the generation of coherent, narrow-bandwidth light far into the VUV. The principle of harmonic generation is often explained in terms of the classical Lorentz model where the bonding of an electron to the atomic nucleus is visualised by a spring, which to a first approximation, i.e. for small displacements of the electron away from its equilibrium position with respect to the nucleus, gives rise to a harmonic binding potential [10]. An electron bound this way and experiencing an oscillating monochromatic electric field will, if the field is sufficiently weak, respond by carrying out a harmonic motion which, by Maxwell's equations, will give rise to emission of light at the driving frequency. If the magnitude of the driving field amplitude is large enough for the electronic motion to become anharmonic, the light emitted by this oscillating dipole will, in addition to the driving (or fundamental) frequency component, contain the second-, third- or higher order multiple of this frequency. In a simplified picture, frequency doubling may be visualized as the electron moving further up the walls of the potential well as the field amplitude increases. This gives rise to an additional dipole moment perpendicular to the light polarization, oscillating at twice the frequency of the driving field [11].

Formally, the macroscopic polarization P of the medium can be written in the dipole-approximation in terms of the electric field amplitude E as

$$P = \chi^{(1)}E + \chi^{(2)}E^2 + \chi^{(3)}E^3 + \dots, \quad (1.1)$$

where $\chi^{(1)}$ and $\chi^{(n)}$, $n \geq 2$, are the linear and n th order non-linear optical susceptibilities, respectively. The expansion is valid in the time- as well as

the frequency domain with the susceptibilities being equal and $\chi^{(n)}$ providing the connection between the frequency generated in the n th order non-linear process and that of the driving field [12]. In principle, the third- or higher order harmonic radiation could just as well result from sum-frequency mixing of the second harmonic with the fundamental and in general, the $(n-1)$ th harmonic generation process is considered a special case of n -wave mixing of n different driving fields.

From the above expansion and Maxwell's equations the field amplitudes and intensities as a function of propagation length of the generated harmonic radiation can be calculated. This assumes a knowledge of the frequency, intensity and focusing conditions for the driving field (or fields) and of the dispersion properties of the medium. The intensity I_{VUV} of the generated field depends on the density of the medium N , the non-linear susceptibility $\chi^{(n)}$, the focusing conditions and the intensities of the driving fields in a manner indicated by stating it for the case of four-wave sum- and difference frequency mixing, $\omega_{\text{VUV}} = 2\omega_1 \pm \omega_2$, with driving fields of frequencies ω_1 and ω_2 and intensities I_1 and I_2 , respectively [13]:

$$I_{\text{VUV}} \propto N^2 [\chi^{(3)}]^2 I_1^2 I_2 F(b\Delta k). \quad (1.2)$$

Here, b is the confocal parameter, assuming Gaussian beams, and $\Delta k = k_{\text{VUV}} - (2k_1 \pm k_2)$ is the wavevector mismatch with k_{VUV} , k_1 and k_2 denoting the wavevectors of the generated- and driving fields, respectively. $F(b\Delta k)$ is the so-called phase-matching factor which is maximum for $b\Delta k = -2$ and $\Delta k = 0$ for sum- and difference frequency mixing, respectively [14]. The difference between the two phase-matching relations originates from the difference in driving polarizations and the Gouy phaseshift $\phi(z)$ experienced along the direction of propagation z of a Gaussian beam traversing a focal point [15]. Since the polarizations responsible for sum- and difference frequency mixing are proportional to $E_1^2 E_2$ and $E_1^2 E_2^*$ (* denoting complex conjugate), respectively, the phase differences between the polarizations and the generated (Gaussian) fields will be $3\phi - \phi = 2\phi$ and $\phi - \phi = 0$, respectively, assuming Gaussian beams of the form $E_j(z) \propto \exp(i\phi(z))$, $j = 1, 2$ [10]. The Gouy phaseshift thus introduced in sum-frequency mixing must be compensated by a negative dispersion as expressed by the phase-matching conditions given above [16].

Frequency mixing can be performed in non-linear crystals down to ~ 190 nm, below which most materials become absorbing [17]. The simplest of the mixing processes, second-harmonic generation, works down to ~ 200 nm, with the cut-off being dictated by the phase-matching conditions [18]. This limit may be pushed closer to the absorption edge by the application of sum-frequency mixing [19]. The current short-wavelength limit of ~ 170 nm

has been reached in LBO [20] as well as LiBO [21], both of which have absorption edges at ~ 160 nm. Moving towards shorter wavelengths means switching to gases which are isotropic media and by symmetry considerations can be shown to prohibit the generation of even-order harmonics [11]. The most popular choices are the rare gases and metal vapours, the latter being more difficult to handle experimentally but providing broad autoionizing, i.e. doubly-excited, states appropriate for resonant enhancement [22]. Gases and wavelengths for four-wave mixing are preferentially chosen such that the frequency of either the driving- or generated light fields are closest possible to a resonant (multi-photon) transition in the non-linear medium. In the vicinity of such a transition the dispersion varies considerably, being negative (positive) above (below) the atomic level, thus making it easier to fulfil the phase-matching requirements. As an example, the $5p$ - $5d$ transition of Xe at 119.2 nm is often used to enhance the amount of 118 nm light generated by frequency-tripling of 355 nm, with the phase-matching condition being tuned by varying the Xe gas pressure (cf. chapter 3). It should be noted that the phase-matching conditions in general are easier fulfilled by difference- as opposed to sum-frequency mixing, because the negative dispersion required in the latter case only can be obtained on the upper side of a resonant transition. On the other hand, sum-frequency generation is possible down to ~ 60 nm while difference-frequency mixing becomes difficult below ~ 110 nm [13, 19]. Typically, 10^9 - 10^{11} photons/pulse are generated [23] in a $\sim 10^{-6}$ relative bandwidth [24, 25] with the higher value obtained in the case of resonant enhancement.

For wavelength generation effectively down to ~ 160 nm and possibly ~ 130 nm, the alternative technique of stimulated Stokes and anti-Stokes Raman shifting may also be applied [26, 27]. Here, light is generated with a frequency which is equal to that of the driving field shifted up (anti-Stokes) or down (Stokes) by n times the frequency of a characteristic transition in the applied medium. Typically, H_2 with its relatively large vibrational $\nu = 0 \leftrightarrow \nu = 1$ transition frequency is employed. The anti-Stokes process assumes a population in the $\nu = 1$ level which is provided by the Stokes process. The generation efficiency decreases rapidly with increasing order, with $n = 2$ being a typical choice for practical applications [28].

1.3 High-harmonic generation

Proceeding to intensities where the light field can no longer be considered a perturbation to the Coulomb field exerted on an atomic electron, the perturbative expansion of the polarization no longer converges [29]. This is usually considered the strong-field regime and corresponds to intensities in the 10^{13} -

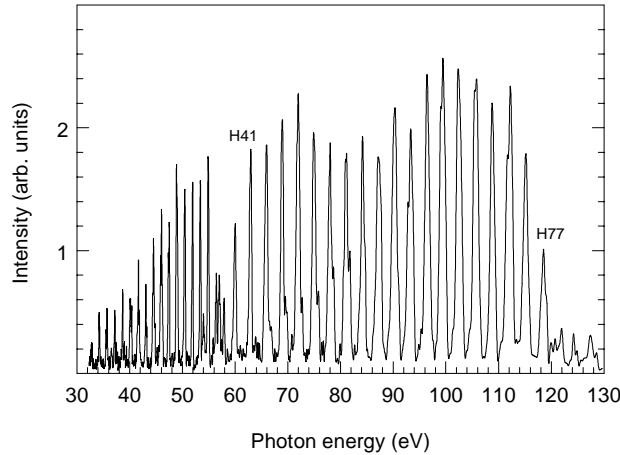


Figure 1.1: A typical harmonic spectrum generated in our laboratory with ~ 7 mJ, 800 nm, 100 fs laser pulses in Ne. A Zr foil with a ~ 55 eV absorption edge has been inserted in the beam path to prevent stray laser light from entering the spectrometer.

10^{15} W/cm 2 range. The upper limit represents a typical barrier-suppression intensity corresponding to a (static) electric field strength at which the barrier imposed on the atomic Coulomb potential is sufficiently suppressed that an electron can escape freely. In this regime harmonic generation results in a spectrum extending far beyond the third- or fifth orders accounted for by perturbation theory. The harmonic yield decreases with the first few orders and then levels off to a plateau extending to a characteristic cut-off frequency. Figure 1.1 shows an example of such a spectrum recorded in our laboratory by focusing ~ 7 mJ, 800 nm, 100 fs pulses from a Ti:Sapphire laser to an intensity of $\sim 10^{15}$ W/cm 2 in a Ne-gas jet. The low-frequency cut-off at order 35th (~ 55 eV) reflects the absorption edge of a Zr foil inserted in the beam path after the gas jet in order to prevent stray laser light from reaching the spectrometer. The high-frequency cut-off appears at order 77th while a contracted, second-order replica of the spectrum is visible below the low-frequency cut-off.

For an appropriate description of this regime, theoretical approaches such as the strong-field approximation [30] and numerical integration of the time-dependent Schrödinger equation [31] have been developed. The strong-field approximation can be considered a quantum-mechanical realization of a classical two-step model introduced by Corkum [32] and Schafer *et al.* [33], providing a unified picture of the competing processes of above-threshold ionization (ATI) and high-harmonic generation (HHG). ATI is the proces of

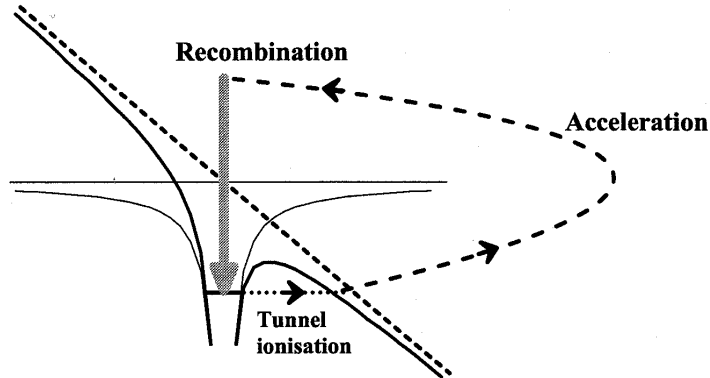


Figure 1.2: A schematic of the tunneling picture, or two-step model, used to describe the mechanism of high-harmonic generation for a single atom. From [34].

multi-photon ionization with the absorption of more photons than required for ionization, giving rise to peaks in the photoelectron kinetic-energy spectrum separated by one photon energy [35]. In the two-step model the electric light field is assumed to vary sufficiently slowly that it makes sense to consider an electron tunneling through the barrier created in the atomic Coulomb potential by the field. Since the Coulomb potential is most strongly bent at the field extrema, the ionization probability is strongly peaked in time. The possibility exists that an electron released this way is pushed back towards the residual ion, following the sign change of the electric field vector, as shown in figure 1.2. Upon re-scattering the electron may acquire additional kinetic energy, recognized as a plateau in the ATI spectrum extending from $\sim 3U_p$ to $\sim 10U_p$ [36, 37, 38] where U_p is the average quiver energy of the free electron oscillating in the field. The electron may also recombine with the ion, thereby releasing a photon with a frequency which is an odd multiple of the laser frequency (HHG). The maximum instantaneous kinetic energy of a returning electron turns out to be equal to $3.2U_p$, and adding the ionization potential I_p —the energy released upon recombination to the ground state—yields the cut-off energy, $E_{cut} = I_p + 3.2U_p$, observed in high-harmonic radiation spectra [32].

The average quiver energy of a free electron with charge $-e$ and mass m depends on the frequency ω and peak intensity I of the light field through the relation $U_p = e^2 I / 4m\omega^2 = 9.33 \times 10^{-14} I [\text{W}/\text{cm}^2] \lambda [\mu\text{m}]^2$ and is often called the ponderomotive energy. This originates from the fact that the time-average of the Lorentz force, also called the ponderomotive force, in the case of a light field with slowly varying electric- and magnetic field amplitudes,

can be expressed as the negative gradient of a term equal to U_p [39, 40]. Although a wiggle energy, U_p in this case acts as a potential energy because it is converted to translational kinetic energy of an electron leaving the optical field [41]. In a real experiment utilizing laser pulses the intensity will always be time-dependent but U_p can be considered a potential energy in the long-pulse limit (ns range), where the electron escapes the interaction region before the intensity changes significantly. In this regime the kinetic energy of an ATI electron leaving the laser focus is given by $E_{kin} = N\hbar\omega - I_p$, where I_p is the field-free ionization potential and N the number of absorbed photons [42, 43]. The ponderomotive energy manifests itself in the ATI spectrum as a suppression of peaks corresponding to kinetic energies less than U_p . In the short-pulse limit (picosecond–femtosecond range), where the electron does not accelerate significantly before the pulse is gone, U_p is not converted to translational kinetic energy and a kinetic energy $E_{kin} = N\hbar\omega - I_p - U_p$ is detected [42]. Since U_p is proportional to I , this effect becomes more pronounced the higher the intensity and for an intensity of 10^{15} W/cm², typical for HHG, U_p is equal to 60 eV for 800 nm light [44]. Such an intensity implicitly assumes a pulse duration in the femtosecond regime since the rise time of the pulse must be sufficiently short that the gas is not fully ionized before HHG can occur.

According to the cut-off formula, the highest possible harmonic order is generated by using the highest possible intensity and wavelength in addition to a medium with a high ionization potential, favouring the lighter noble gases (He and Ne). Attempts have been made to enhance the cut-off frequency by using the rare-gas like ions Na⁺ and K⁺ but with limited success due to defocusing effects arising from the presence of free electrons [45]. Focusing instead on the generation efficiency, this may be enhanced orders of magnitude by using a shorter wavelength [46] or by choosing a medium with a lower ionization potential, e.g. Ar or Xe, corresponding to a higher polarizability [47]. Since the time spent by the electron in the continuum is proportional to the wavelength, the spread in the associated wavepacket will, upon its return to the nucleus, be larger the longer the wavelength. As a consequence, the recombination probability is reduced and the harmonic yield lowered [34]. With the two-step model in mind it is also easily realized why harmonics are generated much more efficiently with linearly than with elliptically polarized light: in the latter case the emitted electron misses the nucleus upon returning from its excursion to the continuum [48].

One usually distinguishes between two regimes of ATI or HHG, depending on the value of the Keldysh parameter $\gamma = \omega/\omega_t$, which is the ratio between the optical field frequency ω and the frequency ω_t for tunneling of an electron through the barrier induced to the Coulomb potential by the electric field [49].

The situation covered by the two-step model is called the tunneling regime and is characterized by a value $\gamma < 1$. The other regime, characterized by a value $\gamma > 1$, is called the "ordinary ATI" regime, for which the process of ATI dominates that of HHG [35]. In this regime the fast oscillations of the electric field prevent an atomic electron from escaping by tunneling. It sees on the average a zero field, resulting in an ionization probability that is uniform in time [50]. In the tunneling regime the periodicity of maximum ionization, i.e. harmonic generation, equal to half an electric field cycle, explains the periodicity in the frequency spectrum of the emitted harmonic radiation, being equal to twice the frequency of the fundamental laser light [50]. The two ways of ionization may be compared with emptying a bowl of water by shaking it at a high frequency or by tilting it at a low frequency, respectively [51]. Tunneling may be recognized as a smearing of the ATI peak structure, but the boundary between the two regimes, on which most studies have been performed, is not well defined [35].

In practice, the high-harmonic photon-energy cut-off is often limited by the saturation intensity at which the medium is fully ionized rather than by the intensity that is physically provided by the laser. This means that in order to obtain the highest possible harmonic orders, the rise time (in most cases equivalent to the duration) of the laser pulses must be shortest possible. As a consequence of the Fourier transform limit, imposing a minimum value to the product of the laser bandwidth and pulse duration [52], and the fact that the harmonic generation process introduces additional bandwidth broadening [53], there is an upper (lower) limit to the pulse duration (bandwidth) of the harmonics that can be generated at a desired minimum photon energy. Or stated the other way around: there is an upper limit to the photon energy that can be reached with a desired maximum bandwidth. The saturation intensity may be determined experimentally from a measurement of the yield of high-order harmonics of a given order as a function of laser intensity, resulting in an increase which levels off when ionization becomes dominant [44]. Such measurements have only been performed for a few different combinations of pulse durations and wavelengths and only a very limited effort has been directed towards establishing eventual scaling relations [54]. Theoretically, saturation intensities can be calculated in the perturbative regime from a knowledge of the N -photon generalized photoionization cross sections, which, however, are not easily calculated [55]. An attempt to estimate the generalized cross sections of heavier atoms by scaling from those known for the neutral hydrogen atom resulted in an order of magnitude disagreement with experimental data [56]. As a consequence, a relation for the photon energy that can be obtained as a function pulse duration and wavelength is at present not readily available.

To the single-atom picture, outlined in its simplest form above, must be added the phase-matching effects arising from the propagation of the generated harmonic radiation through the gas medium. The medium most often has the shape of a gas jet generated by supersonic expansion through a ~ 1 mm diameter cylindrical nozzle. In the strong-field regime the phase shift from the dispersion of the gas medium is entirely dominated by the Gouy phase shift ($N\pi$ radians along the focus for the N th harmonic) and a strong intensity-dependent variation of the phase of the non-linear polarization along the laser focus (~ 100 radians) [57]. Combining these two effects it can be shown that optimum phase-matching may be obtained by focusing either a few millimeters in front of or behind the gas jet. By focusing in front of the gas jet harmonics will be generated with regular Gaussian spatial profiles while focusing at or behind the jet results in distorted annular profiles [58, 59]. Another consequence of the phase-matching conditions is a modification of the cut-off formula to $E_{cut} = I_p + 2U_p$ [60].

The interest in generation and applications of high-order harmonics has grown tremendously since the initial indications in the 80's that very short wavelengths could be obtained by focusing of intense laser light into noble-gas jets without the need for resonant enhancement [61, 62, 63]. The fundamental properties of the radiation have been thoroughly characterized [64] and advanced optimization procedures utilizing gas-filled hollow waveguides [65] and pulse-shaping of the driving field [66] are now being explored. Harmonics have been generated with many different laser sources and almost any kind of medium that one can think of: in molecular gases [67], atom clusters [68], carbon nanotubes [69] and at solid surfaces [70]. In the latter case both even- and odd orders are obtained because the inversion symmetry is broken at the surface. At present the shortest wavelengths generated are 7.8 nm with 1 ps, 1053 nm Nd:Glass pulses [47], 7.5 nm with 100 fs, 800 nm Ti:Sapphire pulses [71], 6.7 nm with 380 fs, 249 nm KrF pulses [72], and < 4.4 nm [73] and 2.7 nm [74] with 5 fs and 25 fs Ti:Sapphire pulses, respectively. With such short pulses the harmonics become very broad, with the spectrum merging into a continuum for the highest orders. A systematic study of the variation of the bandwidth with harmonic order has recently been performed with 70 fs, 800 nm pulses [75] corresponding to a bandwidth of 26 meV, assuming a Fourier-transform limited Gaussian pulse. The bandwidth was observed to increase from 0.11 eV to 0.37 eV when going from the 7th to the 45th harmonic, then stabilizing at a value of ~ 0.43 eV for the 47–55th. This corresponds to relative widths $\Delta\lambda/\lambda$ of 1×10^{-2} , 5×10^{-3} and 5×10^{-3} respectively. For comparison, the bandwidth of the 13th harmonic of a 80 ps dye laser operated at 760 nm has been measured to be 0.01 nm ($\Delta\lambda/\lambda = 1 \times 10^{-4}$) while that of the 27th harmonic of a 140 fs, 825 nm Cr:LiSAF laser was found

to be 0.1 nm ($\Delta\lambda/\lambda = 3 \times 10^{-3}$ [64]). The bandwidth is largely determined by the Fourier-transform principle with additional broadening introduced by the time-dependent variation of the refractive index due to ionization of the gas medium [53, 64]. The pulse duration τ_q and divergence θ_q are comparable to, and in general expected to be smaller than, those of the driving field, τ_o and θ_o , behaving approximately as $\tau_q \sim \tau_o/\sqrt{p}$ and $\theta_q \sim \theta_o\sqrt{p}/q$ where q and $p \sim 8$ are the harmonic order and an effective order of non-linearity, respectively [76]. From this the bandwidth may be expected to behave approximately as $\Delta\lambda_q \sim \Delta\lambda_o\sqrt{p}/q^2$ with $\Delta\lambda_o$ being the bandwidth of the driving field. This yields a relative bandwidth of 1×10^{-3} for the 47th harmonic of a 70 fs, 800 nm laser pulse, somewhat smaller than the value measured in [75].

The harmonic pulse duration may be measured by a cross-correlation technique based on the process of laser-assisted photoionization [77, 78]. By this method, the fundamental field is separated into two parts with one part being used for the generation of a high-order harmonic beam (the pump) which is collinearly overlapped with the other part (the probe) in a gas jet. If the pump and probe pulses overlap temporally, a small fraction of the gas-jet atoms ionized by the pump will, in addition, absorb or stimulated emit one or more laser photons from the probe. A monitored photoelectron spectrum will thus, around the peak corresponding to the ionization of a particular atomic level by the harmonic alone, exhibit small side-peaks. By measuring the amplitudes of the side-peaks as a function of the pump-probe delay, the duration of the X-ray pulse can be determined by a deconvolution procedure. Applying this technique, Bouhal *et al.* have found reasonable agreement with theory when including ionization effects which were observed to shorten the pulses temporally [77]. On the other hand, Glover *et al.* observed the harmonic pulse durations to approach that of the driving field when increasing the laser intensity to enhance the ionization [78]. This was explained by a time delay in the harmonic emission due to the intensity variations across the laser focal spot. Using different variants of this technique, Drescher *et al.* have shown the duration of ~ 90 eV harmonics generated by 7 fs, 770 nm laser pulses to be 1.8 fs (shorter than an optical cycle of the driving field) [79], while Paul *et al.* have provided evidence that harmonics generated by ~ 40 fs, 800 nm pulses, without spectral filtering, are phaselocked in time and make up a train of 250 attosecond pulses separated by half an optical cycle [80]. This result was predicted by theory and paves the way for a low-repetition rate attosecond light source, provided the phase-relations can be manipulated in a way that allows the train within each femtosecond pulse to add up coherently to form a single spike. This is analogous to the principle of modelocking known from lasers which, however, relies on a phase-relationship in the frequency- as opposed to the time domain [81].

Although harmonics have been generated up to 460 eV (order 183th or 2.7 nm) in He, the number of photons at such high energies—around 100 within a 1 % bandwidth of the continuous spectrum [73]—is too low for realistic applications. In general, there is a tendency for a slight decrease of the harmonic yield with increasing order in the plateau region. On average, on the order of 10^4 and 10^5 photons/pulse are typically generated in He and Ne, respectively, for orders in the range 50–100 (78–124 eV) [46, 47, 53, 82]. For Ar and Xe the corresponding numbers are 10^8 and 10^9 photons/pulse, respectively for orders below the 25th (40 eV) with the Xe value corresponding to a conversion efficiency on the order of 10^{-6} [47, 53]. These values are consistent with the numbers of 10^9 – 10^{11} photons/pulse stated for the 50–200 nm region of four-wave mixing. The uncertainty on the above values is probably around an order of magnitude, reflecting the scatter among the values stated in the literature, and is due to differing experimental conditions and the difficulties involved in absolute measurements. Setting a lower limit of 10^4 photons/pulse/0.1 % bandwidth for a realizable experiment, HHG should be considered a useful technique for photon energies below ~ 120 eV.

1.4 Comparison with other methods of VUV light- and X-ray generation

As may be evident from the above, high-order harmonics constitute a useful source of VUV light, competitive to synchrotron radiation for many applications. Spatial [83] and temporal [84] coherence and automatic synchronization with the generating laser field can be added to the properties listed in the previous section. The limitations to the photon energies and bandwidths that can be obtained at present do, however, justify a search for alternative sources, especially for studies of structural dynamics where synchrotron-radiation sources cannot provide the required temporal resolution. A comparison of the presently available sources of VUV light and X-rays for high-resolution studies in the frequency- and time domains are given in tables 1.1 and 1.2, respectively. The listed parameters are only intended as a guide, and in practice significant deviations may occur from the stated values. For the synchrotron-radiation sources (ASTRID, ALS and SSRL) the spectral bandwidth may be reduced at the expense of photon flux and still be practically applicable. For example, the cross section of doubly-excited states in He at ~ 64 eV has been measured at the ALS with a resolution of 1 meV corresponding to a 1.5×10^{-5} relative bandwidth [85]. Also, as exemplified by the 1.4×10^{-7} relative bandwidth obtained for 58.4 nm radiation by Eikema *et al.* (cf. section 1.1), harmonic radiation may be spectrally nar-

rower than stated in table 1.1. In the low-energy part of the 40 eV region it is likely that the bandwidth may be decreased significantly below the stated value of 5×10^{-3} by increasing the pulse duration from the femtosecond to the picosecond regime as is currently being investigated [86]. As stated in section 1.3, it is at present uncertain how long the pulses can be made while still being able to reach a given harmonic order and synchrotron radiation should thus be considered the superior spectral source at present. Obviously, for high-resolution frequency measurements where the time structure of the radiation is irrelevant, the high photon flux implied by the high repetition rate of synchrotron-radiation sources can be fully exploited, making them advantageous in this respect also.

Narrow-bandwidth laser radiation is commercially available only down to 157 nm, provided by a non-tunable F_2 laser. Proceeding to shorter wavelengths becomes difficult because of the lack of neutral atoms and molecules with electronic transition frequencies that are large enough for the required population inversion. One has to resort to stimulated emission from excited states of multiply charged ions in laser-produced plasmas, or from the recombination of electron-ion pairs in such plasmas [87]. X-ray lasers are favourable in terms of the (Doppler-limited) bandwidth and the number of photons per shot but the lack of tunability and the very low repetition rate imposed by the power demands to the plasma-producing laser make them useless for most applications at the present stage of development.

For studies of structural dynamics where a pump-probe configuration is desired, the high repetition rate of the synchrotron-radiation sources cannot be exploited and in addition, the pulse duration is limited to ~ 100 ps [88] by the electronic bunch length. The bunch length is difficult to reduce further due to Coulomb scattering among the electrons, causing a momentum redistribution and subsequent time broadening and loss of confinement in the storage ring [89]. For the same reason electron diffraction experiments are limited to the picosecond regime [90, 91] with the current record being 1 ps [90]. Further compression to the femtosecond regime is, though, possible by acceleration through a very long (\sim km) linac, and terminating with a ~ 100 m undulator results in a mirror-less X-ray free-electron laser (X-FEL). The operation is based on the coherent amplification of spontaneously emitted synchrotron radiation which interacts with the electrons wiggling along the undulator [92, 93, 94]. Such a device, superior in all respects to other sources, is planned to become operational at DESY in Hamburg as well as at the SSRL in Stanford by ~ 2010 [95]. The DESY project is divided into three parts, of which phase I—a FEL operating at 109 nm—was completed in the fall of 2000 [96]. The parameters for the VUV-FEL and X-FEL listed in table 1.2 are referring to the subsequent phases II and III.

Table 1.1: A comparison of parameters for existing VUV light sources with the highest available frequency resolution. Bandwidth refers to the relative bandwidth.

Source	Energy	Bandwidth	Photons/s	Rep. rate
<40 eV				
ASTRID (SGMII) [97]	12–40 eV	$<1 \times 10^{-4}$	2×10^{11}	$\sim 10^8$ Hz
ALS (10.0.1) [98]	17–340 eV	$<1 \times 10^{-4}$	$< 1 \times 10^{13}$	$\sim 10^8$ Hz
HHG ^a	10–40 eV	$\geq 1 \times 10^{-6}$	10^9 – 10^{10}	10 Hz
>40 eV				
ASTRID (Miyake) [97]	15–180 eV	5×10^{-4}	2×10^{11}	$\sim 10^8$ Hz
ALS (10.0.1) [98]	17–340 eV	$<1 \times 10^{-4}$	$< 10^{13}$	$\sim 10^8$ Hz
SSRL (5-3) [99]	90–450 eV	2 – 5×10^{-4}	1.2×10^{11}	$\sim 10^8$ Hz
HHG	40–120 eV	$\leq 5 \times 10^{-3}$	10^5 – 10^6	10 Hz
X-ray laser [100, 101]	<200 eV	7×10^{-5}	10^7 – 10^{11}	10^{-3} Hz

^aincluding lower orders and four-wave mixing

Table 1.2: A comparison of parameters for existing or planned VUV light- and X-ray sources with the highest available time resolution. Thomson, Slicing and LPP refer to Thomson scattering, slicing of synchrotron-radiation bunches, and laser-produced plasma, respectively.

Source	Energy	Duration	Photons/s ^a	Rep. rate
VUV				
HHG	<120 eV	<100 fs	10^5 – 10^6	10 Hz
VUV-FEL (DESY) [102]	60–200 eV	300 fs	3×10^{18}	75 kHz
X-ray				
Thomson [103, 104]	5–30 keV	300 fs	5×10^3	5 Hz
Slicing ^c [103, 104]	0.3–10 keV	100 fs	3×10^6	1 kHz
LPP [105, 106]	1–10 keV	<300 fs	5×10^{5b}	10 Hz
X-FEL (DESY) [102]	0.8–12.4 keV	90 fs	$\sim 8 \times 10^{17}$	55 kHz
X-FEL (SSRL) [92]	0.8–8.0 keV	233 fs	$\sim 5 \times 10^{13}$	120 Hz

^awithin a 0.1 % bandwidth

^bafter refocusing mirror with a collection angle of 7.4×10^{-3} steradians [105, 107]. The flux emitted into 4π steradians may approach $\sim 10^{11}$ photons/s [106, 107].

^cassuming separation of the slices in an undulator

Until the realization and availability of X-ray free-electron lasers, experiments will have to rely on alternative and less ambitious approaches such as X-ray emission from a laser-produced plasma, Thomson scattering or gating of the synchrotron-radiation pulses or electron bunches from existing storage rings. A plasma is generated when an intense (10^{13} – 10^{15} W/cm²) laser pulse interacts with a solid, giving rise to an instantaneous electronic heating, approaching several keV. As a result, pulsed X-rays are emitted in a

broad spectrum consisting of bremsstrahlung from free-electron-ion interactions and line emissions from bound-bound electronic transitions of various ion states [87]. The pulse duration is longer than but comparable to that of the plasma-producing laser, being determined by the thermalization process of the fast electrons which happens on a sub-picosecond time-scale (cf. chapter 5) [105, 106]. In addition to being spectrally very broad and inhomogeneous, a beam of laser-produced X-rays is incoherent and suffers from a very large divergence (2π steradians). In addition, the liberation of material during the laser-solid interaction makes the method less compatible with ultrahigh vacuum conditions. Among the sources of femtosecond VUV- and X-rays listed in table 1.2, high-order harmonics and laser-produced plasma X-rays, covering complementary energy regimes, are the least demanding in terms of experimental equipment and furthermore have the advantage of being inherently synchronized with the generating laser.

By the application of a streak camera which acts as an ultrafast detector, effectively gating the synchrotron-radiation pulses, the temporal resolution has been improved to 3 ps [108]. The limit is set by the response time of the camera and, more importantly, the temporal jitter associated with the triggering of the device [109]. A further improvement in time resolution may be obtained by gating the electron bunches themselves by letting them interact with femtosecond laser pulses in an undulator [104]. This results in energy-modulated electron slices of femtosecond duration, spatially distinguishing themselves from the main bunches in a subsequent bend magnet or undulator and giving rise to femtosecond pulses of synchrotron radiation. On the subsequent turn of the main bunches around the ring the original electron-bunch structure is recovered and thus ready for slicing immediately afterwards. The method of Thomson scattering utilizes the two times relativistic Doppler shift experienced by laser photons scattered elastically off a relativistic electron beam. [103, 104]. The first Doppler shift arises when transforming the laser photon energy to the rest frame of the electron beam and the second from the transformation of the photon energy of the scattered radiation back into the laboratory frame.

References

- [1] H. Stapelfeldt *et al.*, Phys. Rev. A **58**, 426 (1998).
- [2] G. Stark and P. L. Smith, in *Atomic, Molecular and Optical Physics Handbook*, edited by G. W. F. Drake (AIP Press, New York, 1996).
- [3] *McGraw-Hill Encyclopedia of Science and Technology* (McGraw-Hill, New York, 1971), Vol. 14.
- [4] *van Nostrand's Scientific Encyclopedia*, edited by D. M. Considine and G. D. Considine (Van Nostrand Reinhold, New York, Seventh Edition, 1989).
- [5] J.-P. Connerade, J. Phys. II France **2**, 757 (1992).
- [6] K. S. Eikema *et al.*, Phys. Rev. Lett. **76**, 1216 (1996).
- [7] A. Huber *et al.*, Phys. Rev. A **59**, 1844 (1999).
- [8] S. Backus *et al.*, Rev. Sci. Instrum. **69**, 1207 (1998).
- [9] P. A. Franken *et al.*, Phys. Rev. Lett. **7**, 118 (1961).
- [10] P. W. Milonni and J. H. Eberly, *Lasers* (John Wiley & Sons, New York, 1988).
- [11] R. Finley and E. Mazur, in *Ultrafast Dynamics of Quantum Systems: Physical Processes and Spectroscopic Techniques*, edited by B. D. Bartolo (Plenum, NATO ASI Series, 1998).
- [12] J. F. Reintjes, *Nonlinear Optical Parametric Processes in Liquids and Gases* (Academic Press, Orlando, 1984).
- [13] K. Yamanouchi and S. Tsuchiya, J. Phys. B **28**, 133 (1995).

-
- [14] C. R. Vidal, in *Tunable Lasers*, edited by L. F. Mollenauer *et al.* (Springer, Berlin, 1992).
- [15] S. Feng and H. G. Winful, *Opt. Lett.* **26**, 485 (2001).
- [16] J. Larsson, *Laser Spectroscopy on Atoms and Ions using Short-Wavelength Radiation* (Ph.D. thesis, Department of Physics, Lund Institute of Technology, Sweden, 1994).
- [17] V. G. Dmitriev *et al.*, *Handbook of Nonlinear Optical Crystals* (Springer, Berlin, 1999).
- [18] T.-J. Chen *et al.*, *Phys. Rev. A* **51**, 706 (1995).
- [19] J. Larsson, *Physica Scripta* **49**, 173 (1994).
- [20] F. Seifert *et al.*, *Opt. Lett.* **19**, 1538 (1994).
- [21] V. Petrov *et al.*, *J. Appl. Phys.* **84**, 5887 (1998).
- [22] W. Jamroz and B. P. Stoicheff, *Progress in Optics* **XX**, 327 (1983).
- [23] V. G. Arkhipkin and A. K. Popov, *Sov. Phys. Usp.* **30**, 952 (1987).
- [24] A. H. Kung and Y. T. Lee, in *Vacuum Ultraviolet Photoionization and Photodissociation of Molecules and Clusters*, edited by C. Y. Ng (World Scientific, Singapore, 1991).
- [25] J. W. Hepburn, in *Vacuum Ultraviolet Photoionization and Photodissociation of Molecules and Clusters*, edited by C. Y. Ng (World Scientific, Singapore, 1991).
- [26] Y. K. Shen, *The Principles of Nonlinear Optics* (John Wiley & Sons, New York, 1984).
- [27] H. Wallmeier and H. Zacharias, *Appl. Phys. B* **45**, 263 (1988).
- [28] Z. Li, *Time-resolved Laser Spectroscopic Studies of Atoms, Ions and Molecules* (Ph.D. thesis, Department of Physics, Lund Institute of Technology, Sweden, 2000).
- [29] P. Balcou and A. L'Huillier, *Phys. Rev. A* **47**, 1447 (1993).
- [30] M. Lewenstein *et al.*, *Phys. Rev. A* **49**, 2117 (1994).
- [31] M. B. Gaarde *et al.*, *Phys. Rev. A* **57**, 4553 (1998).
- [32] P. B. Corkum, *Phys. Rev. Lett.* **71**, 1994 (1993).

-
- [33] K. J. Schafer *et al.*, Phys. Rev. Lett. **70**, 1599 (1993).
- [34] C. Lyngå, *High-Order Harmonics—Characterization, Optimization and Applications* (Ph.D. thesis, Department of Physics, Lund Institute of Technology, Sweden, 1999).
- [35] L. F. DiMauro and P. Agostini, Adv. At. Mol. Phys. **35**, 79 (1995).
- [36] G. G. Paulus *et al.*, Phys. Rev. Lett. **72**, 2851 (1994).
- [37] G. G. Paulus *et al.*, J. Phys. B **27**, L703 (1994).
- [38] A. Lohr *et al.*, Phys. Rev. A **55**, R4003 (1997).
- [39] T. W. B. Kibble, Phys. Rev. Lett. **16**, 1054 (1966).
- [40] R. R. Freeman and P. H. Bucksbaum, J. Phys. B **24**, 325 (1991).
- [41] P. H. Bucksbaum *et al.*, J. Opt. Soc. Am. B **4**, 760 (1987).
- [42] R. R. Freeman *et al.*, in *Atoms in Intense Laser Fields*, edited by M. Gavrilá (Academic Press, New York, 1992).
- [43] H. G. Müller *et al.*, in *Atoms in Intense Laser Fields*, edited by M. Gavrilá (Academic Press, New York, 1992).
- [44] C.-G. Wahlström, Physica Scripta **49**, 201 (1994).
- [45] C.-G. Wahlström *et al.*, Phys. Rev. A **51**, 585 (1995).
- [46] T. Ditmire *et al.*, Phys. Rev. A **51**, R902 (1995).
- [47] A. L’Huillier and P. Balcou, Phys. Rev. Lett. **70**, 774 (1993).
- [48] K. S. Budil *et al.*, Phys. Rev. A **48**, R3437 (1993).
- [49] L. V. Keldysh, Sov. Phys. JETP **20**, 1307 (1965).
- [50] H. G. Müller, Comments At. Mol. Phys. **24**, 355 (1990).
- [51] H. G. Müller, in *Atomic Physics 15*, edited by H. B. van Linden van den Heuvell *et al.* (World Scientific, Singapore, 1996).
- [52] C. Rullière, *Femtosecond Laser Pulses* (Springer, Berlin, 1998).
- [53] C.-G. Wahlström *et al.*, Phys. Rev. A **48**, 4709 (1993).
- [54] L. A. Lomprè *et al.*, in *Abstracts of the International Conference on Multiphoton Processes ICOMP V* (Paris, France, 1990).

- [55] C. J. G. Uiterwaal *et al.*, Phys. Rev. A **57**, 392 (1998).
- [56] P. Lambropoulos and X. Tang, J. Opt. Soc. Am. B **4**, 821 (1987).
- [57] P. Salières *et al.*, Adv. At. Mol. Phys. **4**, 83 (1999).
- [58] P. Balcou *et al.*, Phys. Rev. A **55**, 3204 (1997).
- [59] P. Salières *et al.*, J. Phys. B **29**, 4771 (1996).
- [60] A. L’Huillier *et al.*, Phys. Rev. A **48**, R3433 (1993).
- [61] J. Bokor *et al.*, Opt. Lett. **8**, 217 (1983).
- [62] A. McPherson *et al.*, J. Opt. Soc. Am. B **4**, 595 (1987).
- [63] M. Ferray *et al.*, J. Phys. B **21**, L31 (1988).
- [64] A. L’Huillier *et al.*, J. Nonlinear Opt. Phys. Mat. **4**, 467 (1995).
- [65] A. Rundquist *et al.*, Science **280**, 1412 (1998).
- [66] R. Bartels *et al.*, Nature **406**, 164 (2000).
- [67] C. Lyngå *et al.*, J. Phys. B **29**, 3293 (1996).
- [68] T. D. Donnelly *et al.*, Phys. Rev. Lett. **76**, 2472 (1996).
- [69] G. Y. Slepyan *et al.*, Phys. Rev. A **60**, R777 (1999).
- [70] P. A. Norreys, Phys. Rev. Lett. **76**, 1832 (1996).
- [71] J. J. Macklin *et al.*, Phys. Rev. Lett. **70**, 766 (1993).
- [72] S. G. Preston *et al.*, Phys. Rev. A **53**, R31 (1996).
- [73] C. Spielmann *et al.*, Science **278**, 661 (1997).
- [74] Z. Chang *et al.*, Phys. Rev. Lett. **79**, 2967 (1997).
- [75] L. Nugent-Glandorf *et al.*, Phys. Rev. A **62**, 023812 (2000).
- [76] J. E. Muffett *et al.*, J. Phys. B **27**, 5693 (1994).
- [77] A. Bouhal *et al.*, Phys. Rev. A **58**, 389 (1998).
- [78] T. E. Glover *et al.*, Phys. Rev. A **63**, 023403 (2001).
- [79] M. Drescher *et al.*, Science **291**, 1923 (2001).

- [80] P. M. Paul *et al.*, *Science* **292**, 1689 (2001).
- [81] I. P. Christov *et al.*, *Phys. Rev. Lett.* **86**, 5458 (2001).
- [82] G. Sommerer *et al.*, *Opt. Comm.* **146**, 347 (1998).
- [83] R. Zerne *et al.*, *Phys. Rev. Lett.* **79**, 1006 (1997).
- [84] M. Bellini *et al.*, *Phys. Rev. Lett.* **81**, 297 (1998).
- [85] K. Schulz *et al.*, *Phys. Rev. Lett.* **77**, 3086 (1996).
- [86] S. Schiemann *et al.*, *IEEE J. Quantum Electronics* **33**, 358 (1997).
- [87] D. Attwood, *Soft X-rays and Extreme Ultraviolet Radiation, Principles and Applications* (Cambridge University Press, United Kingdom, 2000).
- [88] F. Schotte *et al.*, in *Third Generation Hard X-Ray Synchrotron Radiation Sources: Source Properties, Optics, and Experimental Techniques*, edited by D. M. Mills (John Wiley & Sons, New York, in press, 2001).
- [89] H. Winick, *J. Synchrotron Rad.* **5**, 168 (1998).
- [90] H. Ihee *et al.*, *Science* **291**, 458 (2001).
- [91] X. Z. Zeng *et al.*, *Phys. Rev. B* **59**, 14907 (1999).
- [92] *Linac Coherent Light Source (LCLS) Design Study Report, The LCLS Design Study Group, SLAC-R-521, UC-414, Stanford, USA* (available from <http://www-ssrl.slac.stanford.edu/LCLS/lcls-pubs.html>, 1998).
- [93] *Conceptual Design Study Report of a 500 GeV e^+e^- Linear Collider with Integrated X-ray Laser Facility, DESY, Germany*, edited by R. Brinkman *et al.* (available from <http://www.desy.de/~wroblewt/scifel/scifel.html>, 1997).
- [94] P. G. O'Shea and H. P. Freund, *Science* **292**, 1853 (2001).
- [95] G. Materlik, *The TESLA XFEL Project* (available from http://www-hasylab.desy.de/science/annualreports/1999_report/partI/, 1999).
- [96] J. Andruszkow *et al.*, *Phys. Rev. Lett.* **85**, 3825 (2000).
- [97] *Parameters from the homepage of the beamlines of the ASTRID storage ring, Denmark* (<http://www.isa.au.dk/SR/sr-facilities.html>, 2001).

-
- [98] *Parameters from the homepage of the 10.0.1 beamline of the ALS storage ring, Berkeley, USA* (available from http://www-als.lbl.gov/als/als_users_bl/bl_table.html, 2001).
- [99] *Parameters from the homepage of the 5-3 beamline at the Stanford Synchrotron Radiation Laboratory, USA* (available from http://www-ssrl.slac.stanford.edu/beamlines/bl_characteristics.html, 2001).
- [100] P. Jaeglè, *Experimental Methods in the Physical Sciences* **31**, 101 (1998).
- [101] J. Zhang *et al.*, *Science* **276**, 1097 (1997).
- [102] *Parameters of the VUV-FEL and X-FEL at DESY, Hamburg, Germany* (see <http://www-hasyllab.desy.de/workshops/cluster.html>, 2001).
- [103] W. P. Leemans *et al.*, *IEEE J. Quantum Electronics* **33**, 1925 (1997).
- [104] R. W. Schoenlein *et al.*, *Appl. Phys. B* **71**, 1 (2000).
- [105] A. Rousse *et al.*, *Rev. Mod. Phys.* **73**, 17 (2001).
- [106] C. Rose-Petruck *et al.*, *Nature* **398**, 310 (1999).
- [107] A. Rousse *et al.*, *J. Appl. Cryst.* **32**, 977 (1999).
- [108] A. M. Lindenberg *et al.*, *Phys. Rev. Lett.* **84**, 111 (2000).
- [109] J. Larsson *et al.*, *Opt. Lett.* **22**, 1012 (1997).

Chapter 2

Negative ions

2.1 Introduction

Compared with their neutral- and positively charged counterparts, negatively charged atoms and molecules have until recently been studied to a much lesser extent [1, 2, 3, 4]. Obvious reasons are their minor abundance in nature and the challenges that they impose to experiment and theory. Experimentally, negative ions can only be generated in limited amounts and are more fragile than neutral systems. In addition, detachment thresholds and excited electronic states are often located in the far infrared and UV/VUV parts of the spectrum, respectively, where laser light is not readily available. Theoretically, calculations of negative-ion properties are complicated by the electron-correlation effects introduced by the presence of the extra electron, and for molecules the lack of spherical symmetry induces further difficulties.

Negative ions are thus interesting in their own right as systems which are representative of new challenges to theory and experiment. In addition, understanding their properties adds to our feeling of moving towards a completion of the periodic table by knowing not only the properties of the neutral atoms and molecules but also those of the singly charged positive- and negative ions. Proceeding a step further, one might be interested in the properties of doubly-charged positive- and negative ions [5] or even more exotic systems like positronic atoms [6] and -molecules [7] obtained by adding a positron to the corresponding neutral system. Apart from these fundamental aspects, negative ions are interesting from the point of view of their role in different physical processes in nature as well as in technical applications. For example, H^- has long been recognized as the main source of opacity in the infrared part of the solar spectrum, due to its detachment by photon energies exceed-

ing the binding energy of 0.75 eV [8]. H^- is also speculated to play a role in the mechanism of formation of molecular hydrogen in the interior of the interstellar medium [9]. Due to the absence of a dipole moment in the ground state, H_2 cannot simply be formed by the radiative association of two ground-state H atoms; another type of particle is needed to carry away the excess energy required for the binding [10, 11]. This particle could, for example, be an electron emitted in a H^- -H collision and it has recently been proposed to look for signatures of H^- in the VUV part of the absorption spectra of interstellar clouds [9]. Also heavier atomic- and molecular negative ions have been considered to play a role in the chemistry of the stars [12] and the interstellar medium [13]. Recently, absorption spectra of small, linear carbon-chain anions obtained by laboratory laser-spectroscopic measurements were found to compare remarkably well with astrophysically observed diffuse interstellar bands [14]. Negative molecular ions are, in addition, abundant 20–120 km above the surface of the Earth in the form of O_2^- , OH^- , ClO^- , O_3^- , NO_2^- , O_4^- , NO_3^- , CO_3^- etc. [15] and must be included in theoretical models of the atmosphere [16, 17]. In the laboratory, negative ions are the key ingredients in accelerator mass spectroscopy which has proven a very sensitive technique in terms of detection efficiency and mass resolution for, e.g., carbon 14 dating [18] and investigations of rare- or heavy negative ions [19]. Negative ions are also abundant in plasmas and discharges [20] where they play a role in laser action and semiconductor device processing [21].

2.2 Negative-ion structure

From the above it is hopefully evident that negative ions are worth further investigations, but one could start by asking whether the binding of an electron to a neutral atom or -molecule is at all possible. Indeed, the structure of a negative ion is very different from that of a neutral system, especially for small atoms where the ratio of negative- to positive charge is large and electron-correlation effects therefore more pronounced. The binding of an extra electron to the ground state of a neutral atom is accomplished by it inducing to the atom an electric dipole moment which acts back on it as an attractive $1/r^4$ short-range potential [20, 22]. In a classical picture the neutral atom (or molecule) feels an electric field $\vec{E} \propto \vec{r}/r^3$ from the electron approaching a distance r away. This induces to the atom a dipole moment $\vec{P} \propto \alpha \vec{E}$, α being the dipole polarizability, which gives rise to the attractive $\Phi \propto \vec{P} \cdot \vec{r}/2r^3 \propto 1/r^4$ potential [23]. Unlike the long-range Coulomb potential acting on an electron of a neutral atom, the short-range potential implies a finite number of bound states. In general, only a single bound state exists, but the single-electron continuum may reveal a rich structure of doubly-excited

states, or resonances, that are often associated with excited states of the neutral parent atom. The doubly-excited states usually decay by emission of an electron, leaving the resulting neutral atom in its ground state or a lower-lying excited state. This process is called auto-detachment and is analogous to the autoionization mechanism known for neutral systems. Resonances can be excited by photon absorption from the ground state of the negative ion or by collisions of the corresponding neutral atom or molecule with, e.g., electrons. Laser spectroscopy is superior to electron scattering in terms of energy resolution but is—because of radiative selection rules—restricted to angular momentum states that can be reached by one- or two-photon absorption from the ground state or a metastable state of the negative ion.

In the case of H^- an extra electron may be bound with respect to an excited state of the neutral atom by the long-range $1/r^2$ dipole potential resulting from a mixing of the degenerate angular momentum states by the electric field of the approaching electron. This leads to series of doubly-excited states, resonances, converging exponentially to the thresholds defined by excited states of the neutral hydrogen atom [24]. The neutral hydrogen atom is the only element exhibiting such a degeneracy, and in general resonances of negative ions cannot be characterized by such a systematic behaviour. Even for the hydrogen atom the degeneracy is not exact due to the relativistic fine structure and QED splitting of the excited states, implying a deviation from the ideal dipole potential and a termination of the exponential series.

Traditionally, doubly-excited states are divided into the idealized classes of Feshbach- and shape resonances [25, 26, 27]. A shape resonance is considered the result of trapping the extra electron behind a barrier formed by the short-range potential and the centrifugal barrier of the neutral atom, thus existing for non-zero orbital angular momenta. The bound state is energetically located above an excited state of the neutral atom and decays by tunneling of the electron through the barrier, resulting in a relatively short lifetime ($\sim 10^{-15}$ s), or a width on the order of an eV. A Feshbach resonance may be considered the result of attaching the extra electron to an electronically excited state of the neutral atom or molecule with the electrons on average sharing the total available energy. By arbitrary energy fluctuations one of the electrons will eventually become energetic enough that the system autodetaches with a relatively long lifetime (10^{-11} – 10^{-13} s), corresponding to a width in the μeV – meV range. A doubly-excited state may, however, live for considerably longer time (microseconds) if its decay is forbidden by autodetachment selection rules. Such a state is considered metastable [28] and can only be observed in a time-of-flight measurement (cf. chapter 4). For molecular negative-ion resonances the additional possibility exists that the electron can be associated with a vibrationally- or rotationally excited state

located energetically above the detachment threshold of the neutral molecule [29, 30]. The autodetachment process then implies a conversion of the excess rotational or vibrational energy into electronic energy and represents a violation of the adiabatic, or Born-Oppenheimer, approximation. In this approximation the molecular electronic structure is calculated by assuming the electronic motions to be decoupled from those of the nuclei, as justified by the fast electronic response to changes in the nuclear coordinates [31]. According to Fano, the photo-absorption- or scattering cross section for energies E in the vicinity of a Feshbach resonance located in a single-electron continuum can be written as

$$\sigma(E) = \sigma_o \frac{(q + \epsilon)^2}{1 + \epsilon^2} \quad (2.1)$$

with $\epsilon = 2(E - E_o)/\Gamma$ [32]. E_o and Γ are the energy and width of the resonance, σ_o the non-resonant contribution to the cross section and q the so-called asymmetry parameter, the square of which is the probability of excitation of the resonance followed by autodetachment relative to the probability of direct excitation of a continuum state. The higher lying the resonance, the less is the probability of its excitation (less overlap between the resonance and ground-state wavefunctions), causing the resonances to show up more and more like dips than like peaks in the cross section. In case of several close-lying resonances the above formula must be modified as suggested by Ueda [33].

2.3 Status on negative-ion knowledge

Since a ground-state negative ion is stabilized by an incoming electron causing a spatial rearrangement of the electronic charge distribution in order to "absorb" the extra charge, one may expect binding to be more likely the larger the atom or molecule. This is to some extent true, but a significant role is played by the quantum-mechanical energetic distribution of charge over atomic- or molecular orbitals. Neutral atoms with a closed outer valence shell are very unlikely to form negative ions while the reverse is expected for atoms lacking an electron in having such a configuration. Thus, the noble-gas negative ions are unstable in the ground state apart from element 118 which is slightly stabilized due to relativistic effects [34]. With a closed s^2 sub-shell, the alkaline-earth atoms were for a long time considered unable to bind an extra electron. In 1987, however, evidence was provided for the stability of the Ca^- ion, accomplished by the binding of the extra electron in a p orbital by a few tens of meV. This was unexpected from a comparison with the iso-electronic Sc atom, for which the outermost bound electron occupies a

d-orbital [35]. Since then, the stability of the heavier negative ions, Sr⁻ and Ba⁻, of this group has been established, as expected on account of the larger dipole polarizability exhibited by their neutral parent atoms [35, 36]. Although heavier than Ca, the elements of the alkaline-earth subgroup, Zn, Cd and Hg, are unable to bind an extra electron in the ground state [3]. Apart from nitrogen the rest of the most common elements of the periodic table are able to form negative ions with electron affinities in the 0.1-3.6 eV range, the highest values being attained by the halogens [3, 37]. The instability of nitrogen originates from its half-filled outer *p*³ shell with parallel spins of all the electrons; adding an extra electron with anti-parallel spin increases the Coulomb repulsion energy between the electrons above that of the neutral atom, due to the Pauli exclusion principle [38].

Considering the doubly-excited states of negative atomic ions and restricting the discussion to levels accessible by one-photon absorption, most information is available about H⁻, He⁻ and the negative ions of the alkali- and alkaline earth atoms. These are the most interesting from a theoretical point of view, especially H⁻ which has been the subject of the largest number of experimental and theoretical studies as described in chapter 3. He⁻ is known to exist in a metastable $1s2s2p\ ^4P$ state with a $\sim 350\ \mu\text{s}$ lifetime, bound with respect to the excited $1s2s\ ^3S$ state 19.8 eV above the $1s^2\ ^1S$ ground state of He [39]. By photon absorption from the 4P state a total of 15 4S and 4P resonances, located 22.7–24.0 eV above the He ground state and encompassing the He($n=3,4,5$) thresholds, have been investigated by the group of Hanstorp [40, 41]. In addition, a lower-lying $1s2p^2\ ^4P$ shape resonance associated with the $1s2p\ ^3P$ state of He has been observed by Walter and Peterson [42]. Most of these resonances have been predicted by theory [41], which in addition predicts a very weak, broad 4S resonance, not amenable to experimental observation [43]. Ar⁻ exists in a metastable $\dots 3p^54s4p\ ^4S$ state with a 260 ns lifetime, bound by 32.5 meV with respect to the $\dots 3p^54s\ ^3P$ state 11.6 eV above the $\dots 3p^6$ ground state of Ar [44]. A similar state has been predicted for Xe⁻ but not yet experimentally observed [45].

Among the alkali negative ions Li⁻ is particularly interesting due to the similarity of its electronic structure with that of H⁻ [46]. For the lower-lying Li⁻ resonances the number of available decay channels is larger—causing the resonances to become broader—than those of H⁻ due to the non-degeneracy of the Li(*nl*) thresholds implied by the non-hydrogenic Li⁺ core [47]. For the higher-lying Li⁻ resonances the influence of the core is less pronounced and the Li⁻ spectrum becomes increasingly similar to that of H⁻ [46]. Dellwo *et al.* have studied the energy region corresponding to the $1s^22p\ ^2P$ excited state of Li, 1.85 eV above the $1s^22s\ ^2S$ ground state of Li, giving no clear indications of resonance structure [48]. The majority of experimental information

available has been provided by Hanstorp *et al.* who have observed a total of 17 1S and 1P resonances in the region 3.7–5.0 eV above the Li ground state, encompassing the Li($4p,5p,6p$) thresholds [47, 49, 50, 51]. The agreement with the theoretically calculated cross section covering this energy range is very good [46]. Hanstorp *et al.* have, in addition, recently observed four and seven resonances of Na $^-$ [52] and K $^-$ [53], respectively, associated with the Na($4d$) and K($5d,7s,5f$) thresholds. Prior to these studies two K $^-$ resonances had previously been observed at the K($4p$) threshold, ~ 1.6 eV above the K ground state [54]. Two analogous resonances have been observed in Rb $^-$ and Cs $^-$ by Patterson *et al.* [55] while a $\dots 6s6p$ 3P shape resonance just above the $\dots 5p^66s$ 2S ground state of Cs has been observed by Scheer *et al.* [56]. No further predictions of resonances accessible by one-photon absorption are available for these elements.

Common to the lighter alkaline-earth negative ions is the existence of an optical transition from a 4S state to a lower-lying 4P state [35, 57] which for Be $^-$ has a lifetime of 42 μs and is the lowest-lying metastable state of this ion [58]. For Mg $^-$, the optical transition remains to be observed experimentally, and a lifetime in the ns– μs range is expected for the 4P level [35]. An analogous 4P state with a ps lifetime has been observed for Sr $^-$ [35]. Finally, a shape resonance of Ca $^-$ has been observed by Walter and Peterson [59] while additional resonances of Be $^-$, Mg $^-$ and Ca $^-$ have been predicted by, e.g., Zeng *et al.* [60] but not yet observed experimentally.

The amount of information available about doubly-excited states for the remaining elements of the period table is scarce, encompassing experimental studies on individual resonances in C $^-$ [61], Si $^-$ [62], Cu $^-$ [63] and Au $^-$ [64], and theoretical studies of C $^-$ [65], Si $^-$, Ge $^-$ [66] and Cr $^-$ [67]. Common to all the experimental studies referred to above is the application of laser light in the visible part of the spectrum, which suffices for studies where the ionization potential and the electron affinity of the neutral atom and the negative ion, respectively, are not too large. In the case of He $^-$ one is "rescued" by the highly metastable 4P state, but shorter-wavelength light is obviously required for the observation of eventual resonances of the halogen negative ions and of H $^-$ (cf. chapter 3).

Proceeding to molecular negative ions, the information is even more limited considering the vast number of ways in which the elements can bind to each other to form stable molecules. Even when limiting the discussion to di- or triatomic species, getting an overview of what is known and what could be interesting for further investigation is a formidable task which will not be attempted here. According to Kalcher "the vast majority of diatomic molecules, homo- as well as heteronuclear species, can form stable ground-state negative ions in the gas phase" [68]. Remarkable exceptions are H $_2^-$,

He_2^- , N_2^- and CO^- [68], of which the latter three have been formed in long-lived (i.e. exceeding microseconds) metastable states as discussed in chapter 4. For systems with a heavier mass the excess electronic charge is more easily distributed within the electronic cloud, and the only unstable three-atomic molecules that I know of, are H_2O^- , H_3^- and CO_2^- (cf. chapter 4). Surveys of molecular negative ions with emphasis on ground-state stabilities and electron affinities have been given by Bates [69] and Rienstra-Kiracofe *et al.* [70] while a graph of the electron affinities as a function of the number of valence electrons can be found in [5]. A large amount of molecular electron affinities have been obtained from photoelectron spectroscopic studies by the groups of Neumark (see, e.g., [71, 72]) and of Bowen, Ellison, Hotop and Lineberger as stated in the introduction to the molecular electron-affinity list given in the CRC Handbook of Chemistry and Physics [73]. Resonances of molecular negative ions have mostly been studied in electron-scattering experiments and investigations have mainly concentrated on the short-lived states of diatomic molecules [74, 75]. In addition, a few laser-spectroscopic studies of vibrational autodetaching states excited from the ground states of stable molecular negative ions have been performed by the group of Lineberger as reviewed by Andersen [29].

2.4 Theoretical approaches to negative-ion structure

2.4.1 Computational methods

Theoretical models of neutral atoms are usually based on the central-field approximation, according to which each electron moves in a spherical symmetric potential representing the interaction with the nucleus and the average effect of the interaction with the remaining electrons [31]. The Schrödinger equation is then separable into single-electron equations, and the atomic antisymmetrized wavefunction, a Slater determinant, can be written in a basis of products of single-electron wavefunctions, orbitals, associated with the principal- and orbital quantum numbers n and l . The spherical symmetric potentials are in the Hartree-Fock-, or Self-Consistent Field (SCF), approach determined self-consistently by variational minimization, and the total atomic energy is determined by the distribution of electrons over values of n and l , the configuration of the system. If the electronic motions are weakly coupled, i.e. if by the introduction of spherical symmetric potentials the major part of the electron-electron interaction term of the Hamiltonian has been accounted for, the remaining part can be treated as a perturbation. The configuration

assignment will then still make sense, but the energy level associated with a given configuration will split into a multiplet of fine-structure components.

For negative ions in the ground- or doubly-excited states and for neutral atoms and molecules in highly excited states, the electron correlation is so large that the above perturbative approach no longer applies. The energy levels can, however, always be associated with a mixture of different configurations and the wavefunction written as a linear combination of Slater determinants. This is the idea behind the configuration interaction (CI) and multi-configurational Hartree-Fock (MCHF) approaches which can be considered natural extensions of the Hartree-Fock method. The additional configurations are often chosen to represent singly-, doubly-, triply- or higher excited states of the dominant configuration applied in the Hartree-Fock procedure, as indicated by an additional labelling S, SD, SDT etc. [76, 77]. Since the singly-excited states do not add to the correlation energy, one has to start out from at least the SD level. In the MCHF approach the radial wavefunctions of the single-electron orbitals are optimized variationally in addition to the coefficients entering the configuration expansion of the total wavefunction. In the CI approach the radial functions are kept fixed [78].

At a higher level of calculation the configurations (or Slater determinants) may be chosen independently, i.e. without representing excitations of the same basic configuration, and the method is then called a multi-reference (MR) MCHF or -CI (e.g. MRCI). In the frozen-core approximation the excitations are limited to the outermost bound valence electrons which are then said to belong to a Complete Active Space (CAS). The method is then called CASSCF, the MC character being implicitly implied by the presence of the CAS. In some situations the interactions between the core electrons or between the valence- and core electrons cannot be ignored, as illustrated by the importance of these contributions for an accurate (to within a few meV) prediction of the Ca^- binding energy [35, 78]. In principle, energy levels can be calculated numerically to arbitrarily high accuracy by inclusion of an arbitrary number of configurations but the calculations quickly become cumbersome and a large number of configurations is required for reasonable convergence. The computational efforts may be minimized by including in the expansion of the total wavefunction terms which depend on the inter-electronic distances, thus from the outset accounting for a larger part of the electron correlation. This is the idea behind the two-electron Hylleraas wave-functions and the elaborations towards the development of possible candidates of correlated wavefunctions applicable to larger systems [79].

The MCHF and MRCI approaches can be applied for calculations of resonance parameters, in addition to bound state properties, by the inclusion of continuum states in the configuration expansion [80]. Of widely use, espe-

cially for smaller atoms, are, in addition, the complex-scaling and R -matrix methods [27] of which in particular the complex-scaling approach has provided very accurate results for H^- as discussed in the following chapter. By this method the resonance energies and -widths are extracted directly as the real- and imaginary parts of the complex eigen-energies obtained from a diagonalization of the total Hamiltonian in a basis of square-integrable orbitals, following a complex scaling of the particle coordinates [81]. The R -matrix method is based on the close-coupling expansion of the total wavefunction in a basis of continuum- and correlation functions [82], treating the resonance as an electron-atom scattering phenomenon and inferring the resonance parameters from a calculation of the scattering cross section [27]. In the R -matrix approximation to the close-coupling expansion, the negative ion is enclosed in a sphere outside which the probability of localizing more than one electron is small. The region within the sphere is treated by the CI procedure while a variational minimization of the close-coupling expansion is performed for the outer region.

In molecular electronic structure calculations, the MCHF and MRCI methods are the most widely used in addition to many-body perturbation theory and the coupled-cluster (CC) approach which represents a higher level of theory. In CC theory the total wavefunction is expanded as a sum of a basic Slater determinant and its excitations as in the CI and MCHF approaches but the excitations are performed by means of a cluster operator, generating additional, so-called disconnected, excitations. For example, the CCSD (S and D denoting single- and double excitations) expansion includes, for a system with more than two electrons, pairs of "co-existing" non-interacting single- or double excitations or one or more single-excitations co-existing with a number of double excitations. These types of excitations become the dominant contributors of electron correlation as the number of electrons increases and are not accounted for by the CI expansion—not even when performed to the highest possible order. At present, calculations become computationally very demanding beyond the CCSD(T) level where the triple excitations are evaluated perturbatively as indicated by the bracket. An even higher level of theory would be obtained by implementing a MR wavefunction in the CC approach but this remains a challenge to theorists.

Comparing the different approaches one should consider not only their level of approximation but also their ability to account for the two types of electron correlation encountered; a static correlation arising from the configuration interaction and a dynamic correlation arising from the instantaneous mutual Coulomb repulsion among the electrons [77]. In reality the two effects are intermingled and the distinction originates from the fact that a correlation prevails even when the electrons are so far apart that they do not

feel the repulsion of each other [77]. In the CI approach both types of correlation are accounted for, but in the MCHF and CC approaches only the static and dynamic correlations, respectively, are included [83]. By the inclusion of static correlation only, one is limited to qualitative predictions of the electronic structure, while quantitative predictions to a ~ 0.1 eV accuracy can be obtained for small molecules when accounting for the dynamic correlation [76, 83].

The accuracy that can be obtained is, though, not only limited by the level of approximation applied in the expansion of the total many-electron wavefunction. Also the molecular orbitals, replacing the atomic orbitals when building the configurations, must be expanded in a basis set which must include an infinite number of functions in order to form a complete set. The path towards the exact solution of the Schrödinger equation is thus one of a two-dimensional optimization of this one-electron basis set on the one hand and the total wavefunction expressed in terms of Slater determinants on the other. Just as there is a hierarchy of many-body models starting at the Hartree-Fock level, there is a hierarchy of one-electron basis sets starting with the atomic-like Slater-type orbitals (STO) and proceeding to Gaussian-type orbitals (GTO) and the numerically more tractable contracted GTO's representing linear-combinations of such functions. Using the contracted GTO's one can proceed from a minimum basis set, in which the number of one-electron functions is chosen in accordance with the actual number of electrons, to a double- or triple zeta (DZ or TZ) type basis including two- or three times as many functions. Often, only the functions representing the valence electrons are doubled or tripled, giving valence double- or triple zeta basis sets (VDZ or VTZ), respectively. In calculations on highly correlated systems the inclusion of polarization functions, i.e. functions representing higher orbital angular momentum, is essential, as denoted by a "p" (e.g. pVTZ), and further correlation consistency, denoted by a cc (e.g. cc-pVTZ) is obtained by including at the same stage of expansion functions that contribute equal amounts of correlation energy. Finally, especially when dealing with negative ions, additional diffuse functions may be of relevance, resulting in an augmentation of the basis set, denoted by AUG (e.g. AUG-cc-pTVZ) [76].

2.4.2 The hyperspherical-coordinate approach

The numerical methods discussed above are more or less reminiscent of the independent-particle approximation and not tailored to deal with the electron correlation. They are, in principle, capable of predicting a negative-ion spectrum to an arbitrarily high accuracy, but they do not provide the link to an understanding, or a visualization, of the underlying electronic struc-

ture responsible for this spectrum. A qualitative understanding and classification of the negative-ion structure, especially the doubly-excited states, in terms of quantum numbers must be accomplished by models that from the outset take the electron correlation into account. Such a model is the hyperspherical-coordinate approach which has been developed for two-electron systems by Lin and Rau, based on group-theoretical work of Herrick and Sinanoglu [84, 85, 86]. A description of this approach will be given here, intended to be sufficiently detailed to give a taste of the origin of the quantum numbers used for the labelling of the H^- resonances discussed in the following chapter.

In the hyperspherical-coordinate approach the 6 coordinates required to describe the two electrons are chosen to be the hyper-radius $R = (r_1^2 + r_2^2)^{1/2}$ reflecting the size of the system (\vec{r}_i is the position of the i th electron with respect to the nucleus), the hyper-angle $\alpha = \arctan(r_2/r_1)$, the angle θ_{12} between \vec{r}_1 and \vec{r}_2 and three Euler angles for localization of the triangle of nucleus and electrons in space. When expressed in terms of these coordinates, the two-electron Schrödinger equation is separable into a set of hyper-radial equations that can be solved in the adiabatic approximation where the motion in the hyper-radius is assumed to be much slower than that in the angles. Adiabatic potential-energy curves obtained this way, giving the electronic energy as a function of the hyper-radius, are shown in figure 2.1 for the $^1P^o$ states of H^- associated with the $\text{H}(n=2)$ threshold. As indicated in the figure, the shapes of the potential-energy curves reflect the symmetry of the total wavefunction, denoted by the radial quantum number A . A can attain the values $+1$ and -1 , corresponding to the electrons moving radially in- and out of phase, respectively, in analogy with the vibrational stretch modes of a linear triatomic molecule. States with $A = +1$ are less stable (i.e. more short-lived) than states with $A = -1$, because the symmetry, in a classical picture, is more easily broken by one electron hitting the nucleus slightly before the other [87]. States with $A = 0$ correspond to one electron being very close to and the other very far away from the nucleus, and the corresponding potential-energy curves are repulsive for all R (curve pd in the figure). For a given n , a manifold of $+$ and $-$ curves exist but only the lowest-lying curve of each type is apparently excited by single-photon absorption [88].

The total potential-energy surface of the system evaluated as a function of α and θ_{12} is singular at $\alpha = 45^\circ$, $\theta = 90^\circ$ corresponding to the two electrons sitting on top of each other and is symmetric with respect to α , exhibiting a saddle shape with a saddle point at $\alpha = 45^\circ$, $\theta = 0^\circ$ (see figure 3 in [85]). The associated ridge states with $r_1 \sim r_2$ are of the $A = +1$ symmetry while the valley states along the θ_{12} axis at $\alpha = 0^\circ$ and $\alpha = 90^\circ$ are of the $A = -1$

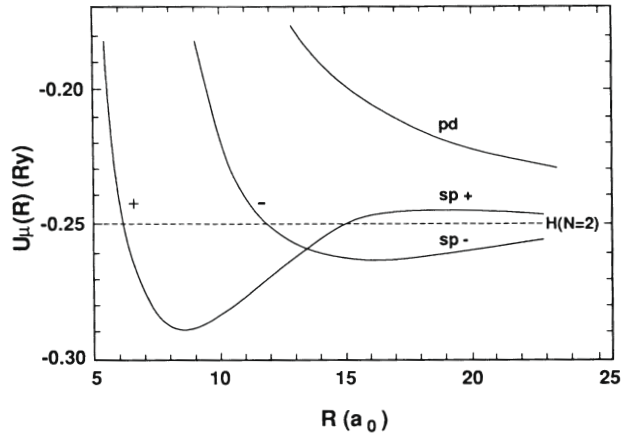


Figure 2.1: Adiabatic potential-energy curves for the $1P^o$ states of H^- associated with the $H(n=2)$ threshold. From [89].

symmetry.

It can be shown that the quantity $\vec{B} \propto \vec{A}_1 - \vec{A}_2$ is a constant of the motion where \vec{A}_i is the so-called Runge-Lenz vector of the i th electron—the quantum mechanical equivalent of the vector directed along the semimajor axis of a classical Kepler ellipse [86]. Due to their commutation, L^2 , B^2 and $(\vec{B} \cdot \vec{L})^2$ can be simultaneously diagonalized, yielding the well-known L quantum number for the total orbital angular momentum in addition to the quantum numbers K and T given by

$$T = 0, 1, 2, \dots, \min(L, n-1) \quad (2.2)$$

and

$$K = n-1-T, n-3-T, \dots, -(n-1-T), \quad (2.3)$$

where $T = 0$ is forbidden if the total parity $\pi = (-1)^{L+1}$. Given the total spin S , A is determined by

$$A = \pi(-1)^{S+T} \quad K > L-n \quad (2.4)$$

$$A = 0 \quad K \leq L-n. \quad (2.5)$$

The angular correlation is contained in the quantum number K which is given approximately by $\langle r_{<} \cos \theta_{12} \rangle$ with $r_{<}$ denoting the radius of the inner electron. The radial correlation is contained in T which can be interpreted

as the projection of \vec{L} onto the inter-electronic axis $\vec{r}_1 - \vec{r}_2$. The resonances can, accordingly, be designated terms of the form ${}_n(K, T)_m^A$, where n denotes the main quantum number of the excited state towards which a series of resonances labelled by m converges ($m \geq n$ for $A = +1$ and $m \geq n + 1$ for $A = -1$). Since redundant information is contained in the ${}_n(K, T)_m^A$ term, the notation ${}_n\{\nu\}_m^A$ is often used instead with $\nu = 1/2(n - 1 - K - T)$ being the so-called rovibrational quantum number. Considering, for example, the ${}^1P^o$ resonances of H^- converging towards the $\text{H}(n=2)$ threshold, T can attain the values $T = 0, 1$ with K being -1 or 1 for $T = 0$ and equal to zero for $T = 1$. For $(K, T) = (1, 0)$ and $(-1, 0)$ the A quantum number becomes -1 and 0 , respectively, while for $(K, T) = (0, 1)$ $A = +1$. There are thus the three possible series ${}_2(0, 1)^+$, ${}_2(1, 0)^-$ and ${}_2(-1, 0)^0$, or ${}_2\{0\}^+$, ${}_2\{0\}^-$ and ${}_2\{1\}^0$, of which the latter corresponds to the repulsive potential (cf. figure 2.1). For the states belonging to the ${}_2(0, 1)^+$ and ${}_2(1, 0)^-$ series the electrons will, in the classical simplification, move in- and out of phase with $\theta_{12} \sim 90^\circ$ ($K \propto \langle r < \cos \theta_{12} \rangle$) and $\theta_{12} \sim 180^\circ$, respectively. For the repulsive states belonging to the ${}_2(-1, 0)^0$ series the electrons are on the same side of the nucleus but at very unequal distances. The three series can be considered analogous to the mixed configurations $2snp + 2pns$, $2snp - 2pns$ and $2pnd$, respectively, as originally proposed by Madden and Codling [90].

Attempts have been made to extend the hyperspherical approach to doubly- and triply-excited states of three-electron atoms, showing that the two-electron quantum numbers carry on to the three-electron doubly-excited states while the triply-excited states require further investigations [91]. It should be noted that the hyperspherical approach with the adiabatic approximation is unable to compete with the computational methods in terms of numerical accuracy but can be cast into a numerically tractable form by means of the close-coupling approach to produce fairly accurate results [92].

References

- [1] L. H. Andersen *et al.*, *Adv. At. Mol. Phys.* **38**, 155 (1997).
- [2] T. Andersen, in *Photonic, Electronic and Atomic Collisions*, edited by F. Aumayr and H. Winter (World Scientific, Singapore, 1998).
- [3] T. Andersen *et al.*, *J. Phys. Chem. Ref. Data* **28**, 1511 (1999).
- [4] J. Kalcher, *Ann. Rev. Prog. Chem. C* **93**, 147 (1997).
- [5] M. K. Scheller *et al.*, *Science* **270**, 1160 (1995).
- [6] G. G. Ryzlikh *et al.*, *J. Phys. B* **31**, 3965 (1998).
- [7] M. Mella *et al.*, *J. Chem. Phys.* **114**, 10579 (2001).
- [8] A. J. Deutsch, *Rev. Mod. Phys.* **20**, 388 (1948).
- [9] D. Field, *Astron. Astrophys.* **362**, 774 (2000).
- [10] T. W. Hartquist and D. A. Williams, *The chemically controlled cosmos* (Cambridge University Press, England, 1995).
- [11] S. Lepp and P. C. Stancil, in *The Molecular Astrophysics of Stars and Galaxies*, edited by T. W. Hartquist and D. A. Williams (Clarendon Press, Oxford, 1998).
- [12] L. M. Branscomb and B. E. J. Pagel, *Mon. Not. R. Astron. Soc.* **18**, 258 (1958).
- [13] S. Petrie *et al.*, *Astrophys. J.* **491**, 210 (1997).
- [14] R. Terzieva and E. Herbst, *Int. J. Mass Spect.* **201**, 135 (2001).
- [15] E. Kopp, in *The upper Atmosphere*, edited by W. Dieminger *et al.* (Springer, Berlin, 1996).

-
- [16] E. Kopp, *Adv. Space Res.* **25**, 173 (2000).
- [17] D. K. Chakrabarty, *Adv. Space Res.* **20**, 2191 (1997).
- [18] L. K. Fifield, *Rep. Prog. Phys.* **62**, 1223 (1999).
- [19] D. Berkovits *et al.*, *Nucl. Inst. Meth. B* **123**, 515 (1997).
- [20] H. Massey, *Negative Ions* (Cambridge University Press, England, 1976).
- [21] W. Ding *et al.*, *J. Appl. Phys.* **84**, 3051 (1998).
- [22] A. R. P. Rau, *Com. At. Mol. Phys.* **14**, 285 (1984).
- [23] P. Kristensen, *Laser spectroscopy of negative ions* (Ph.D. thesis, Institute of Physics and Astronomy, Aarhus University, Denmark, 1997).
- [24] M. Gailitis and R. Damburg, *Proc. Phys. Soc.* **82**, 192 (1963).
- [25] G. J. Schulz, *Rev. Mod. Phys.* **45**, 378 (1973).
- [26] M. A. Biondi *et al.*, *Physics Today* (October 1979, p. 44).
- [27] S. J. Buckman, *Rev. Mod. Phys.* **66**, 539 (1994).
- [28] C. Blondel, *Physica Scripta* **T58**, 31 (1995).
- [29] T. Andersen, *Physica Scripta* **T34**, 23 (1991).
- [30] J. Simons, in *Photoionization and Photodetachment, part II*, edited by C.-Y. Ng (Advanced Series in Physical Chemistry, World Scientific, Singapore, 2000).
- [31] B. H. Bransden and C. J. Joachain, *Physics of Atoms and Molecules* (John Wiley & Sons, New York, 1994).
- [32] U. Fano, *Phys. Rev. A* **124**, 1866 (1961).
- [33] K. Ueda, *Phys. Rev. A* **35**, 2484 (1987).
- [34] E. Eliav *et al.*, *Phys. Rev. Lett.* **77**, 5350 (1996).
- [35] T. Andersen *et al.*, *J. Phys. B* **30**, 3317 (1997).
- [36] J. Kalcher, *Chem. Rev.* **94**, 2291 (1994).
- [37] M.-J. Nadeau *et al.*, *Nucl. Inst. Meth. B* **123**, 521 (1997).

-
- [38] W. P. Wijesundera and A. E. Litherland, Nucl. Inst. Meth. B **123**, 527 (1997).
- [39] T. Andersen *et al.*, Phys. Rev. A **47**, 890 (1993).
- [40] A. E. Klinkmüller *et al.*, J. Phys. B **31**, 2549 (1998).
- [41] I. Y. Kiyani *et al.*, Phys. Rev. Lett. **81**, 2874 (1998).
- [42] C. W. Walter *et al.*, Phys. Rev. A **50**, 2257 (1994).
- [43] N. Brandefelt and E. Lindroth, Phys. Rev. A **59**, 2691 (1999).
- [44] U. V. Pedersen *et al.*, Phys. Rev. A **58**, 258 (1998).
- [45] A. V. Glushkov, JETP Lett. **55**, 97 (1992).
- [46] C. Pan *et al.*, Phys. Rev. A **53**, 840 (1996).
- [47] U. Berzinsh *et al.*, Phys. Rev. Lett. **74**, 4795 (1995).
- [48] J. Dellwo *et al.*, Phys. Rev. A **46**, 3924 (1992).
- [49] U. Ljungblad *et al.*, Phys. Rev. Lett. **77**, 3751 (1996).
- [50] G. Haefliger *et al.*, Phys. Rev. A **57**, 2216 (1998).
- [51] G. Haefliger *et al.*, Phys. Rev. A **63**, 053409 (2001).
- [52] G. Haefliger *et al.*, Phys. Rev. A **59**, 3655 (1999).
- [53] I. Y. Kiyani *et al.*, Phys. Rev. Lett. **84**, 5979 (2000).
- [54] J. Slater *et al.*, Phys. Rev. A **17**, 201 (1978).
- [55] T. A. Patterson *et al.*, Phys. Rev. Lett. **32**, 189 (1974).
- [56] M. Scheer *et al.*, Phys. Rev. Lett. **80**, 684 (1998).
- [57] V. V. Petrunin *et al.*, Phys. Rev. A **63**, 030701 (2001).
- [58] L. Knoll *et al.*, Phys. Rev. A **60**, 1710 (1999).
- [59] C. W. Walter and J. R. Peterson, Phys. Rev. Lett. **68**, 2281 (1992).
- [60] J. Zeng and Q. Lu, Phys. Rev. A **62**, 022713 (2000).
- [61] G. Haefliger *et al.*, J. Phys. B **29**, 3017 (1996).
- [62] P. Balling *et al.*, J. Phys. B **26**, 3531 (1993).

-
- [63] P. Balling *et al.*, J. Phys. B **25**, L565 (1992).
- [64] R. J. Champeau *et al.*, J. Phys. B **31**, 741 (1998).
- [65] G. Y. Kashenock and V. K. Ivanov, Phys. Lett. A **245**, 110 (1998).
- [66] L. Veseth, J. Phys. B **32**, 5725 (1999).
- [67] V. K. Ivanov *et al.*, J. Phys. B **29**, L313 (1996).
- [68] J. Kalcher, Trends in Chem. Phys. **7**, 87 (1999).
- [69] D. R. Bates, Adv. At. Mol. Phys. **27**, 1 (1990).
- [70] J. C. Rienstra-Kiracofe *et al.*, to appear in Chem. Rev. (2001).
- [71] S. E. Bradforth *et al.*, J. Chem. Phys. **98**, 800 (1993).
- [72] I. Yourshaw *et al.*, J. Chem. Phys. **109**, 5247 (1998).
- [73] *CRC Handbook of Chemistry and Physics*, edited by D. R. Lide (CRC Press, Boca Raton, 1992).
- [74] G. J. Schulz, Rev. Mod. Phys. **45**, 423 (1973).
- [75] S. J. Buckman *et al.*, Australian J. Phys. **52**, 473 (1999).
- [76] F. Jensen, *Introduction to Computational Chemistry* (John Wiley & Sons, Chichester, England, 1999).
- [77] T. Helgaker *et al.*, *Molecular Electronic-structure Theory* (John Wiley & Sons, Chichester, England, 2000).
- [78] C. F. Fischer, in *Atomic, Molecular and Optical Physics Handbook*, edited by G. W. F. Drake (AIP Press, New York, 1996).
- [79] L. Bertini *et al.*, J. Phys. B **34**, 257 (2001).
- [80] J. Xi and C. F. Fischer, J. Phys. B **32**, 387 (1999).
- [81] Y. K. Ho, Phys. Rep. **99**, 1 (1983).
- [82] J. Yuan, Phys. Rev. A **61**, 012704 (1999).
- [83] J. Olsen, private communication (2001).
- [84] D. R. Herrick, Adv. Chem. Phys. **52**, 1 (1983).
- [85] C. D. Lin, Adv. At. Mol. Phys. **22**, 77 (1986).

-
- [86] A. R. P. Rau, Rep. Prog. Phys. **53**, 181 (1990).
- [87] P. G. Harris *et al.*, Phys. Rev. A **42**, 6443 (1990).
- [88] H. R. Sadeghpour and C. H. Greene, Phys. Rev. Lett. **65**, 313 (1990).
- [89] C. D. Lin, Phys. Rev. Lett. **35**, 1150 (1975).
- [90] R. P. Madden and K. Codling, Phys. Rev. Lett. **10**, 516 (1963).
- [91] T. Moris and C. D. Lin, Phys. Rev. A **57**, 4268 (1998).
- [92] J.-Z. Tang *et al.*, Phys. Rev. A **49**, 1021 (1994).

Chapter 3

High-resolution VUV spectroscopy of H^-

3.1 Introduction

Apart from its interest in astrophysics H^- is particularly appealing from a fundamental point of view as reflected by the large number of investigations dealing with this system. In addition to being a three-body system, it is the smallest negative ion of the periodic table and thus particularly heavily governed by electron correlation. This is reflected by the failure of the independent-particle model to predict its stability [1]. H^- has a single bound state, the $^1S^e$ ground state, with a binding energy of 0.75419(2) eV as measured in a laser-photodetachment experiment by Lykke *et al.* [2] and calculated with an even higher accuracy [3]. In addition, the spectrum is dominated by series of doubly-excited states embedded in the single-electron continuum 10–12 eV above the H^- ground state and associated with excited states of the neutral hydrogen atom. Using the notation of hyperspherical quantum numbers introduced in the previous chapter, these doubly-excited states, or resonances, can be divided into classes of + and – resonances, each of which may exhibit a Feshbach or shape character. The + and – resonances have widths in the meV and μeV ranges, respectively, so an energy resolution of that order is necessary for their observation. This favours the laser-photodetachment technique, which, however, is not immediately applicable due to the lack of lasers with a photon energy tunable in the 10–12 eV range (cf. chapter 1). Besides, only $^1P^o$ resonances are accessible by single-photon absorption from the $^1S^e$ ground state of H^- .

Apart from a single two-photon absorption experiment addressing the

$^1D^e$ resonance just below the $\text{H}(n=2)$ threshold [4, 5], the $^1P^o$ resonances have been most intensively studied. In the period 1977–1993, Bryant *et al.* performed a unique series of experiments, measuring the single-photon absorption cross section of H^- as a function of photon energy from below the threshold for single-electron detachment to above the threshold for two-electron ejection [6, 7, 8, 9]. This large range of tunability was achieved by varying the angle of intersection of a 800 MeV H^- beam at LAMPF (Los Alamos Meson Physics Facility) with different laser beams of fixed frequency, utilizing the relativistic Doppler shift. The photon-energy resolution was limited to 5–10 meV (FWHM) by the energy spread of the ion beam and the angular divergence imposed by the crossed-beam configuration. Of interest for the present experiment is the observation of the first $^1P^o$ resonance in each of the series ${}_2\{0\}_m^-$ ($m=3,4 \dots$) and ${}_2\{0\}_m^+$ ($m=2,3,4 \dots$), respectively. The energy of the ${}_2\{0\}_3^-$ Feshbach resonance was determined to be 10.9264(6) eV relative to the H^- ground state while the width was limited to ~ 10 meV by the experimental resolution [8]. The ${}_2\{0\}_2^+$ resonance is located as a shape-like structure just above the $\text{H}(n=2)$ threshold and is the only member of this + series [8]. It thus distinguishes itself from the higher-lying + resonances which are members of regular series converging from below towards the respective thresholds.

The deviation of the ${}_2\{0\}_3^-$ resonance energy from values of 10.924 eV and 10.9245 eV calculated by Tang [10] and Lindroth [11], respectively, and the prospect of an even higher energy resolution stimulated the development of an alternative experimental technique at the storage ring ASTRID (Aarhus STorage RIng Denmark) in 1995 [12, 13]. Here, a fixed-frequency VUV laser beam was overlapped collinearly with a 1 MeV H^- beam at one of the straight sections of the ring, the effective photon energy being Doppler-tuned by adjustment of the ion-storage energy [12, 13]. By this method, implying an improvement in the energy resolution by more than two orders of magnitude, a measurement of the cross section in the vicinity of the $\text{H}(n=2)$ threshold yielded a resonance energy of 10.9243(2) eV for the ${}_2\{0\}_3^-$ state while the (deconvolved) width could be confined to the interval $20 \mu\text{eV} < \Gamma < 60 \mu\text{eV}$. Both results were in excellent agreement with theory but the large uncertainty in the width did not allow a critical test of various theoretical models, predicting values in the 28–65 μeV range [10, 14, 15]. The discrepancy with the resonance energy reported by Bryant *et al.* was attributed to the energy-calibration method applied in their experiment [12]. In addition, the ${}_2\{0\}_4^-$ resonance could be resolved for the first time at 10.9519(2) eV, likewise in agreement with theory. The width, predicted to be 2 μeV [16], was entirely dominated by the 180 μeV (FWHM) energy resolution. The measured ${}_2\{0\}_3^-$ and ${}_2\{0\}_4^-$ resonance cross sections are shown in figure 3.1 together with that

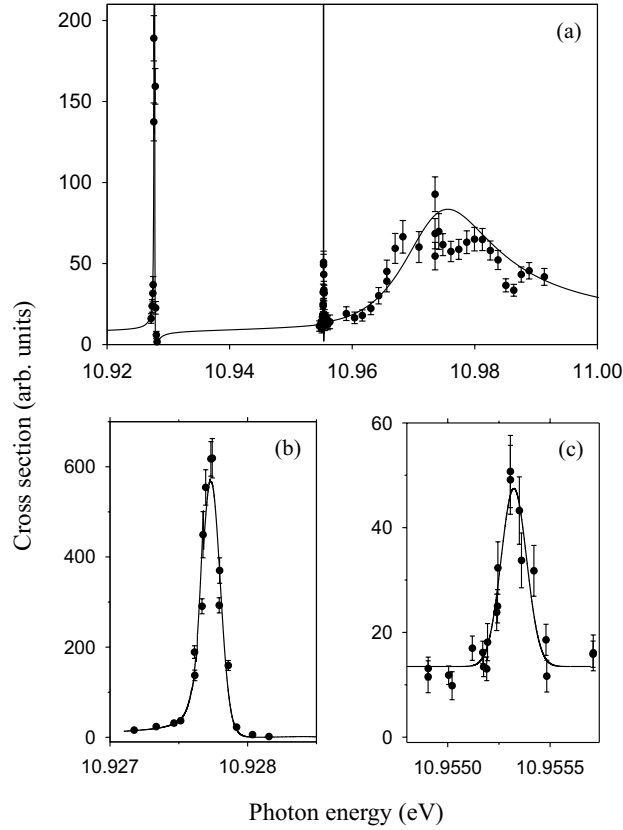


Figure 3.1: (a) Relative photodetachment cross section of D^- in the vicinity of the $D(n=2)$ threshold measured by Andersen *et al.* [13] and normalized to the theoretical results of Lindroth [13]. The scanned energy range includes the $2\{0\}_3^-$ and $2\{0\}_4^-$ Feshbach resonances and the $2\{0\}_2^+$ shape resonance. (b) The $2\{0\}_3^-$ resonance shown on an enlarged scale, fitted to a Fano profile convolved with a Gaussian function representing the experimental resolution. (c) The $2\{0\}_4^-$ resonance shown on an enlarged scale, fitted to a Gaussian function.

of the $2\{0\}_2^+$ shape resonance, which appears non-smooth due to variations in the laser- and ion-beam overlap. This is a consequence of the large scaling in ion-beam energy required to scan the relatively broad photon-energy range covered by this structure. The measured cross section is relative, and each of the three segments has been normalized to the cross section calculated by Lindroth and convolved with the experimental resolution (solid curve). The $2\{0\}_3^-$ and $2\{0\}_4^-$ resonances are shown on an enlarged scale in figures 3.1

(b) and (c), respectively, with the solid curves representing fits to a Fano profile (see chapter 2) convolved with a Gaussian function (representing the experimental resolution), and a pure Gaussian function, respectively. The asymmetry of the $2\{0\}_3^-$ resonance is clearly visible.

Measurements have also been performed on D^- , yielding energies of 10.9277(2) eV and 10.9553(2) eV for the $2\{0\}_3^-$ and $2\{0\}_4^-$ resonances, respectively [13]. The isotope shift of 3.4(0.2) meV thus observed for both resonances is consistent with the shift of 3.2 meV found by scaling the transition energies and the specific mass shift of the ground state according to the difference in reduced masses. The specific mass shift, implied by the mass-polarization term of the two-electron Hamiltonian, has been calculated to be 486 μeV for the H^- ground state but only 10 μeV and 0.33 μeV for the $2\{0\}_3^-$ and $2\{0\}_4^-$ resonances, respectively [17]. The size of this shift is very sensitive to the nature of the state, thus predicted to be 35 μeV for the $2\{0\}_2^+$ shape resonance [11] and -0.1 meV for the $1D^e$ resonance. A measurement of the shift for the $1D^o$ resonance has yielded a value of $-2.4(1.1)$ meV with a possible systematic error of 0.8 meV [4, 5].

One more resonance predominantly of $1P^o$ character, the $2\{0\}_5^-$ state, is predicted to exist very close to the $\text{H}(n=2)$ threshold, with the series then terminating due to the fine-structure and QED splittings of the $\text{H}(n=2)$ level [16, 18]. A fourth resonance, predominantly of $3P^o$ character, but with a predicted 17 % admixture of $1P^o$ configurations located even closer to the threshold should, however, in principle also be accessible by single-photon absorption [18]. Since the width and strength (the integrated cross section) decrease rapidly when going to higher-lying resonances, their observation becomes increasingly difficult; the $2\{0\}_5^-$ resonance with a ~ 0.07 μeV width [15] represents a challenge to experiment.

The present chapter reports the re-investigation of the photodetachment cross section in the vicinity of the $2\{0\}_3^-$ resonance with a factor of four improvement in resolution compared with the ASTRID measurements from 1996–97 [12, 13]. The improvement was accomplished by the application of electron cooling in order to reduce the velocity spread of the negative-ion beam which is the resolution-limiting factor.

3.2 Experimental approach

Figure 3.2 shows a schematic of the experimental setup with the ASTRID storage ring, the electron cooler and the VUV laser system. ASTRID is of 40 m circumference and consists of four straight sections connected by pairs of 45° bending magnets [19]. Each straight section is equipped with two times two focusing quadrupole magnets in addition to a number of correction

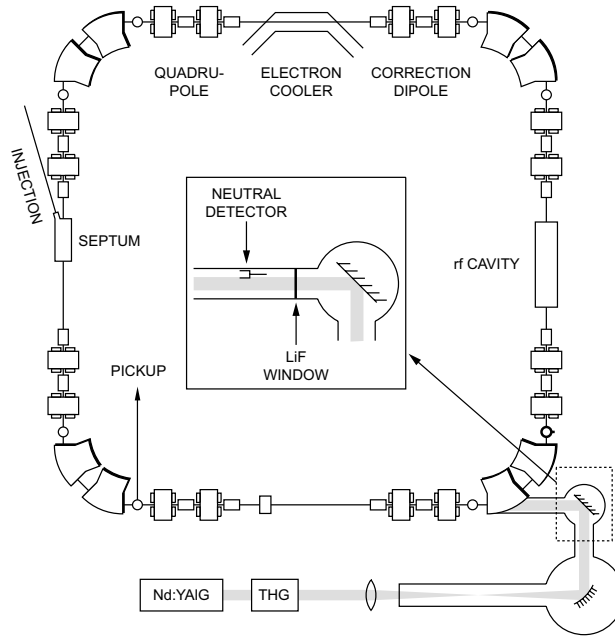


Figure 3.2: A schematic of ASTRID storage ring with the electron cooler and the laser system for Doppler-tuned VUV spectroscopy.

dipoles and sextupoles. The ring is operated at a pressure of $\sim 3 \times 10^{-11}$ Torr with H_2 and He being the dominant rest gas components, and 16 electrostatic pick-up's allow the beam to be positioned to within a few millimeters. A 150 keV D^- ion beam (easier to accelerate than H^-) produced by a duoplasmatron ion source was injected into the ring following mass- and charge-state analysis. Following further acceleration to ~ 1.6 MeV by a radio-frequency field, the $\sim 0.5 \mu\text{A}$ D^- beam was left to circulate in the ring. On one of the straight sections the D^- beam was overlapped almost collinearly with a 118 nm pulsed light beam, the $\sim 0.5^\circ$ angle leaving space for a neutral-atom detector. The yield of D atoms formed during the presence of laser pulses and the background yield originating from collisional detachment were monitored in two separate time gates. The photon flux exiting the other end of the straight section was measured with an Al plate, and a phosphor screen facilitated alignment and control of the 118 nm beam.

The 118 nm (10.48 eV) light was generated by frequency tripling the third harmonic (355 nm) of a 100 Hz, 3 ns pulsed, Nd:YAIG laser, focused to an in-

tensity of $\sim 2 \times 10^{13} \text{ W/cm}^2$ in a gas cell containing ~ 7 mB Xe. This pressure corresponds to optimum phase-matching conditions for the given focusing conditions, as verified by a maximum in the generated 118 nm signal. The conversion efficiency was resonantly enhanced by the proximity of the 118 nm wavelength to the $5p-5d$ electronic transition in Xe [20]. The 118 nm light was separated from the 355 nm beam by an astigmatically focusing spherical grating and subsequently collimated by a curved mirror before entering the ring through a LiF window as a $\sim 1 \text{ cm}^2$ diameter beam. In order to obtain the maximum possible signal in the cross section measurements, the 355 nm laser was operated at a pulse energy of 30–40 mJ which was on the edge of the damage threshold of the grating. In order to prevent an eventual damage implied by the presence of Xe gas, an additional LiF window could be installed in the beam path behind the laser focus to separate the grating from the Xe gas cell (not shown in the figure). Since the transmission of a LiF window, initially $\sim 30\%$, was found to decrease as a function of exposure time to the 355 nm light, 2–3 windows were typically used during two weeks of beamtime, and for the final measurements the LiF window was removed. Although water-cooled, the grating also exhibited a decrease in efficiency as a function of time, following the eventual development of a burned spot, and a new grating had to be used for each beam-time. As it turned out, the gratings bought after the successful beam-times of 1996–97 were down in efficiency by at least an order of magnitude, providing a reflectivity of at most 3%. Only very recently, just before our latest beam-time in November 2000, it was admitted to us that the coating procedure had been changed around 1997. The results presented in the present chapter, recorded in May 1999, have, accordingly, been obtained with an order-of-magnitude reduction in the number of 118 nm photons per pulse compared with the 1996–97 experiments but this was compensated by an one-order-magnitude increase in the repetition rate provided by a new laser. From an absolute measurement utilizing an NO ionization cell, the amount of 118 nm flux available immediately after the grating was estimated to $\sim 6 \times 10^9$ photons/pulse as verified by an order-of-magnitude reduction in the neutral-atom signal per pulse compared with the earlier experiments.

The effective photon energy seen by the ions travelling with mean longitudinal velocity v is given by the Doppler formula as $E_{ph} = \gamma E_L (1 + (v/c) \cos \alpha)$, where $\gamma = 1/\sqrt{1 - (v/c)^2}$, $E_L = 10.48 \text{ eV}$ is the photon energy in the laboratory system and α the angle of intersection, with $\alpha = 0^\circ$ corresponding to counter-propagating beams. With an ion-storage energy limited by the rigidity of the bending magnets to 160 MeV and 85 MeV, the effective photon energy can be varied up to 18.7 eV and 14.2 eV for H⁻ and D⁻, respectively. The spread δE in E , equal to the energy resolution, is determined by the

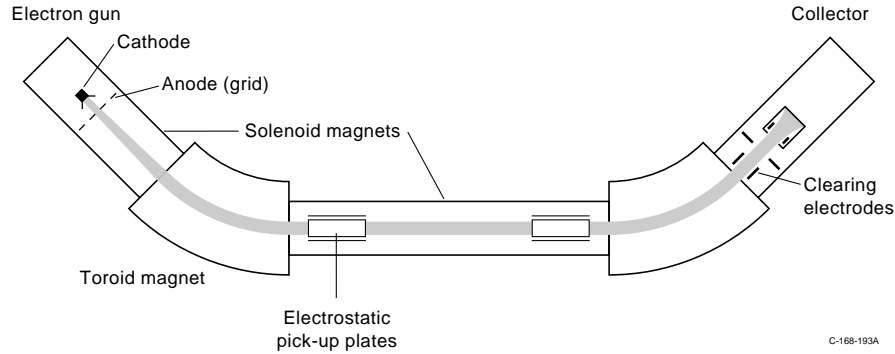


Figure 3.3: A schematic of the electron cooler mounted at ASTRID.

spread in α , E_L and v . Due to the almost collinear geometry, the contribution $\gamma(v/c)E_L \sin \alpha \delta \alpha$ to δE from the spread $\delta \alpha \approx 0.2^\circ$ (FWHM) in $\alpha \approx 0.5^\circ$ amounts to only $13 \mu\text{eV}$ for a 1.6 MeV D^- beam. With a bandwidth $\delta E_L < 1 \mu\text{eV}$ of the laser light, the contribution $(E_L \gamma/c)(\cos \alpha/\gamma^2 + v/c)\delta v$ to δE from the velocity spread δv is the resolution-limiting factor, amounting to $\sim 180 \mu\text{eV}$ for $\delta v/v \sim 4 \times 10^{-4}$ (typical of an uncooled beam, all values are FWHM). The energy spread is seen to increase with kinetic energy, thus attaining a value of 2.4 meV at the maximum effective photon energy available for H^- .

The electron cooler is mounted on the straight section of ASTRID opposite to that of the laser beam. It consists of an electron gun, a 1 m interaction region, and an electron collector as shown in figure 3.3. A 3.6 mA electron beam, corresponding to a density of $5 \times 10^6 \text{ cm}^{-3}$, is emitted by a 1-cm-diameter tungsten cathode and accelerated through an anode grid to 457 eV. The electron beam is guided in and out of the interaction region by solenoid magnetic fields of 100–200 G connected with two deflection toroids. Since the electrons are continuously renewed, the electron-cooling section may be considered a heat exchanger where the velocity spread of an ion beam with longitudinal velocity equal to that of the electron beam is reduced as the ions moving too fast (slow) are decelerated (accelerated) by collisional energy transfer [21]. By the cooling process an equilibrium situation with equal ion- and electron-beam temperatures is approached, implying a velocity spread of the ion beam which is reduced with respect to that of the electron beam by a factor $\sqrt{M/m}$, with M and m being the ion- and electron masses, respectively (assuming Maxwellian velocity distributions). The

longitudinal electron-beam temperature is reduced by the acceleration process to typically $kT_{\parallel} \sim 1$ meV [22] while the transverse temperature, initially equal to the cathode temperature, $kT_{\text{cath}} = 0.11$ eV, can be reduced by adiabatically expanding the electron beam [23]. In the present study, the solenoid magnetic field of the interaction region was reduced by a factor 4.3 with respect to that of the gun, implying an expansion to a $\sqrt{4.3} \times 1$ cm = 2.1 cm diameter electron beam and a factor 4.3 reduction in the transverse temperature to $kT_{\perp} = 26$ meV. For comparison, the effective ion-beam diameter, taking betatron oscillations into account, was ~ 1 cm and could be considered constant on the time scale relevant for longitudinal cooling.

The mean longitudinal velocity v and spread δv of the D^- beam were derived from the average revolution frequency ν and spread $\delta\nu$, monitored with a Schottky pick-up. Due to the large cross section for collisional destruction of a negative-ion beam, the lifetime of the stored beam was limited to a few seconds. Stable cooling, characterized by constant mean velocity and a constant, narrowed velocity spread, must thus be achieved on a similar timescale, and knowing the exact time when this occurs is important for separating out the corresponding neutral-atom signal in the data treatment. The frequency content of the Schottky signal mixed down to ~ 10 kHz was sampled by an analog-to-digital converter and analyzed with a fast Fourier-transform procedure every 0.16 s, allowing ν and $\delta\nu$ to be recorded as a function of time [24].

In order to obtain stable cooling and the lowest possible velocity spread, it is important that the electron- and ion beams are well aligned in the electron cooler [21]. This was achieved by means of a pair of horizontal and vertical pick-up plates placed in the interaction region as shown in figure 3.3. When not used for positioning, the latter were modulated with a 250 kHz AC sine voltage, 6 V peak-to-peak, in order to reach equilibrium within the lifetime of the ion beam. This procedure has been suggested by Marriner *et al.* as a method of reducing the amount of rest-gas ions trapped in the electron beam [25]. Trapped rest gas ions imply a reduction in the magnitude of the electrostatic space-charge potential and a corresponding increase in the electron-beam velocity. Without the modulation voltage the Schottky spectra exhibited significant drifts and stable cooling could not be obtained within several lifetimes of D^- beam storage.

3.3 Results and discussion

Figure 3.4 (a) and (b) show examples of the evolution of the mean longitudinal velocity and the relative velocity spread (FWHM) with time, respectively, for the cooled D^- beam, as obtained by fitting the Schottky spectra to a

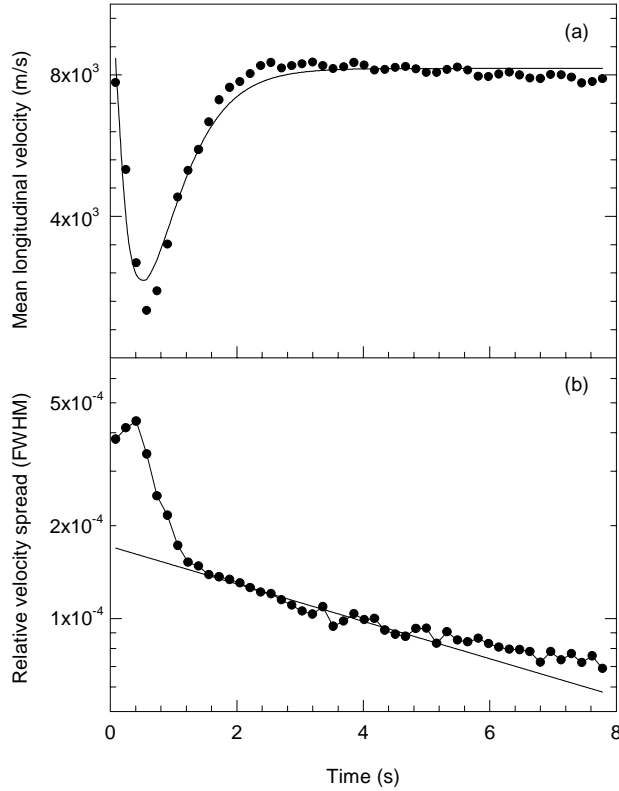


Figure 3.4: (a) Typical evolution of the mean longitudinal velocity with time after acceleration for the cooled D^- beam. A constant of 12454×10^3 m/s should be added to the values displayed on the vertical axis. The data represent an average over 20 injections. The solid curve indicates a fit to two exponentials as discussed in the text. (b) Typical evolution of the relative velocity spread with time after acceleration for the cooled D^- beam. The data represent an average over 20 injections. The solid curve indicates the predicted $I_D^{0.4}$ dependence.

Gaussian function. Initially (0–0.5 s), the velocity of the ion beam is higher than that of the electron beam and is dragged downwards with the ions apparently being slightly heated, as seen from the simultaneous increase in the velocity spread. Subsequently, trapping of rest-gas ions cause an increase in the electron-beam velocity which the D^- ions are forced to follow, thus being dragged to a higher mean velocity again (0.5–2 s). During this time interval, the D^- ion- and electron-beam velocities are equal, and the cooling is very efficient as reflected by the corresponding steep decrease in the D^-

velocity spread. As the velocity distribution narrows, the effect of intrabeam scattering, causing heating, becomes more and more pronounced, and the cooling rate decreases. Eventually an equilibrium situation is reached with equal cooling and intrabeam-scattering rates, as reflected by the slow decrease in the velocity spread and an almost constant mean velocity (2–8 s). In this regime the relative velocity spread is predicted to obey an $I_D^{0.4}$ dependence (equation 161 in [21]), with $I_D \propto \exp(-t/\tau)$ being the D⁻ beam current and τ the lifetime of the ion beam. This dependence is indicated by the solid curve in figure 3.4 (b) and is seen to agree with the data. After 8 s of cooling the relative velocity spread is 7×10^{-5} and thus reduced by a factor of ~ 6 with respect to that of an uncooled beam. The deviation from the $I_D^{0.4}$ law reflects the limit of equal D⁻ ion- and electron-beam temperatures.

The evolution of the mean longitudinal velocity of the D⁻ beam can be predicted from a simple one-dimensional model, disregarding magnetic fields and assuming monochromatic beams with no transverse velocity components. In the binary collision approach of Poth [21] the cooling force is then, with the present conditions, proportional to the difference between the ion- and electron-beam velocities, $F = K(v_D(t) - v_e(t))$ (equation 43c in [21]). The electron-beam velocity is given by $v_e(t) = \sqrt{2V_e(t)/m}$ where $V_e(t)$ is equal to the acceleration energy of the electrons supplied by the electron-cooler cathode voltage U_{cath} , corrected for a small but significant contribution from space-charge. The effect of rest-gas ion trapping is taken into account through this last contribution which, as explained qualitatively above, has a large influence on the time dependence of $v_D(t)$. Denoting by n_e and $n_{r_{gi}}(t)$ the density of electrons and of trapped rest-gas ions, respectively, $V_e(t)$ is given on axis, i.e. in the center of the beam, by

$$V_e(t) = eU_{\text{cath}} + \frac{e^2 r_o^2}{4\epsilon_o} (n_e - n_{r_{gi}}(t)) \left(-1 + 2 \ln \left(\frac{r_o}{R} \right) \right) \quad (3.1)$$

where r_o and R are the electron- and vacuum tube radii, respectively, ϵ_o the vacuum permittivity and e the elementary charge (equation 98 in [21]). Assuming $n_{r_{gi}}(t)$ to approach an equilibrium value n_∞ exponentially with a characteristic "trapping" time τ_t , i.e. writing $n_{r_{gi}}(t) = n_\infty(1 - \exp(-t/\tau_t))$, the time dependence of v_i can now be obtained by solving the Newtonian equation $Mdv_D/dt = K(v_D(t) - v_e(t))$. The result is an expression of the form

$$v_D(t) = A \exp(-t/\tau_c) - B \exp(-t/\tau_t) + C, \quad (3.2)$$

where $\tau_c = 1/K$ is the cooling time and A , B , and C are positive constants. The data of figure 3.4 (a) are fitted well with this expression as indicated by

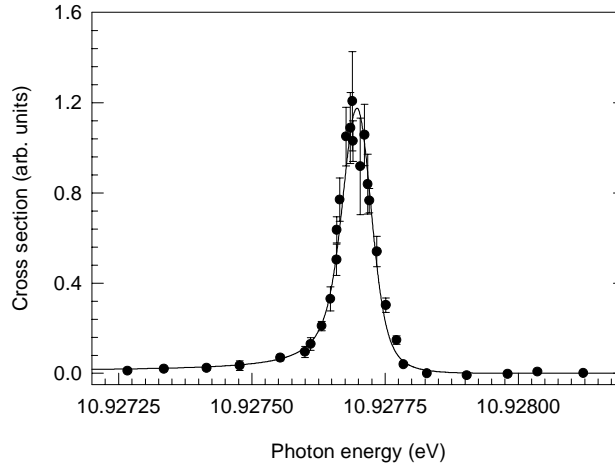


Figure 3.5: Relative photodetachment cross section vs. effective photon energy in the vicinity of the $2\{0\}_3^-$ resonance. The solid curve represents the best fit to a Fano profile convolved with the experimental resolution. The error bars indicate a statistical uncertainty of one standard deviation.

the solid curve, giving values $\tau_c \sim 0.4$ s and $\tau_t \sim 0.5$ s for the cooling- and "trapping" times, respectively.

When measuring the photodetachment cross section only neutral atoms detected within the time interval 3.8–8 s with relatively constant mean velocity and a relative velocity spread below 1×10^{-4} were considered. The contribution to the experimental resolution from the corresponding relative velocity spread averaged over this time interval amounts to $42 \mu\text{eV}$, and adding the (small) contribution from the angular divergence gives a total energy resolution of $44 \mu\text{eV}$. By choosing a smaller time interval corresponding to later times, one could obtain an even higher resolution but at the expense of statistics due to the decaying ion beam, and a trade-off has to be made. Figure 3.5 shows the relative photodetachment cross section in the vicinity of the $1P^o 2\{0\}_3^-$ resonance as deduced from the fitted amplitudes of the exponential decays of the photodetachment signal [20]. The clearly asymmetric resonance has been fitted to a Fano profile convolved with a Gaussian function of width $44 \mu\text{eV}$ (FWHM) as indicated by the solid curve. Representing a time average, this width in fact slightly overestimates the exponential resolution due to the small (oscillatory) drift of the mean velocity with time (figure 3.4 (a)). This was accounted for by including in the fit of the experimental amplitudes a time dependence of the cross section, reflecting the time dependencies of the mean velocity and the velocity spread. Since the cross

section in addition depends on the unknown resonance parameters which in turn depend on the distribution of the exponential amplitudes over photon energy (or, equivalently, velocity), the resonance was fitted iteratively: the exponential amplitudes were corrected in accordance with the small changes in the resonance parameters obtained from fitting the resonance while keeping the Gaussian width fixed at 44 μeV .

Quantitatively, the cross section was in the first approximation calculated as $\sigma_1 = (b_1/a - 1)/\Phi\tau$ where Φ is the 118 nm photon flux, τ the lifetime of the D⁻ beam, and a and b_1 the amplitudes obtained from fits to $a \exp(-t/\tau)$ and $b_1 \exp(-t/\tau)$ of the neutral-atom signal monitored in the background- and signal gates, respectively. The σ_1 values were plotted as a function of the photon energy E_{ph} and the resulting curve was fitted to a Fano profile convolved with a Gaussian function, as given by

$$\tilde{\sigma}_1 = \int K \frac{\left(q_1 + \frac{2(E-E_1)}{\Gamma_1}\right)^2}{1 + \left(\frac{2(E-E_1)}{\Gamma_1}\right)^2} \exp\left(-\left(\frac{E-E_{ph}}{\delta}\right)^2\right) dE. \quad (3.3)$$

Here, $\delta = 18.7 \mu\text{eV}$ is the experimental resolution (44 μeV FWHM), K a constant and E_1 , Γ_1 and q_1 the resonance energy, -width and -asymmetry parameter obtained from the fit, respectively. Corrected exponential amplitudes were accordingly calculated as $b_2 = a(\Phi\tau\tilde{\sigma}_1(E_1, q_1, \Gamma_1) + 1)$ and the neutral-atom signal of the signal gate fitted to $\tilde{b}_2(t) \exp(-t/\tau)$, where

$$\begin{aligned} \tilde{b}_2(t) &= a[1 + \Phi\tau x_1 \tilde{\sigma}_1(t)] \\ &= a\left[1 + \Phi\tau x_1 \int K \frac{\left(q_1 + \frac{2(E-E_1)}{\Gamma_1}\right)^2}{1 + \left(\frac{2(E-E_1)}{\Gamma_1}\right)^2} \exp\left(-\left(\frac{E-E_{ph}(t)}{\delta(t)}\right)^2\right) dE\right], \end{aligned} \quad (3.4)$$

to obtain a value for x_1 . $E_{ph}(t)$ and $\delta(t)$ were read from the data files with the Schottky measurements. If $E_{ph}(t)$ and $\delta(t)$ were constant in time, x_1 should be equal to 1, and the time-dependence of these parameters is thus transferred into a deviation of x_1 from this value. The measured cross sections were corrected according to $\sigma_2 = x_1\tilde{\sigma}_1(E_1, q_1, \Gamma_1)$ and again fitted to a Fano profile convolved with a Gaussian function to yield $\tilde{\sigma}_2(E_2, q_2, \Gamma_2)$, and so on. The resonance was fitted using the commercial programme PeakFit while the exponential amplitudes including the time drift could only be fitted with a programme made in Turbo Pascal, based on the routines described in the book "Numerical Recipes in Pascal" [26]. Both programmes are designed to perform a least-square χ^2 minimization, using the Levenberg-Marquardt method and should therefore be expected to yield exactly the same resonance

Table 3.1: A comparison of experimental- and theoretical results for the ${}^1P^o_2\{0\}_3^-$ resonance of D^- converging to the $D(n=2)$ threshold. The resonance energy E_R is given with reference to the D^- ground state.

	E_R/eV	$\Gamma/\mu eV$	q
Experiment			
Andersen <i>et al.</i> [13]	10.9277(2)	20–60	-30 – -10
Balling <i>et al.</i> [20]		57(15)	
Present		37(3)	-16(3)
Theory			
Ho ^a [27]	10.92773	35.9	
Sadeghpour ^a <i>et al.</i> [14]	10.9287	28.8	
Chang ^a [28]	10.9278	40.0	
Cortés and Martin ^a [29]	10.9278	32.4	-15.9
Tang <i>et al.</i> ^a [10]	10.927	65.3	
Venuti and Decleva ^a [30]	10.92774	37.2	-16.5
Lindroth <i>et al.</i> ^a [16]	10.92770	37.2	-17
Gien ^b [31]	10.92771	37.7	
Bürgers ^a [17]	10.92773	37.2	
Kuan <i>et al.</i> ^a [32]	10.92773	36.9	
Chen ^a [33]	10.92770	35.6	
Bylicki and Nicolaides ^a [15]	10.92773	37.0	

^a Converted from the total energy of the system (in a.u.) to the energy with respect to the ground state of D^- using a conversion factor of $27.211383 M/(M+m)$ eV [34]. A D^- ground-state energy of 14.356789 eV relative to the two-electron escape threshold is derived from [3], neglecting the small mass dependence of the relativistic- and QED corrections.

^b Converted from transition energies in Rydberg using a conversion factor of $13.605692 M/(M+m)$ eV.

parameters. The parameters obtained from the home-made programme did, however, deviate slightly from those of PeakFit and did not converge as the number of iterations was increased. The reason for this discrepancy is at present unclear but the PeakFit parameters should beyond doubt be considered the "best" ones since they exhibit the right convergence behaviour.

By the application of this iterative procedure a width Γ of $37(3)$ μeV and an asymmetry parameter q of $-16(3)$ was obtained for the ${}^1P^o_2\{0\}_3^-$ resonance. The result is listed in table 3.1 together with the existing experimental results for D^- and a number of recent theoretical predictions. The discrepancy of the width with the recently reported experimental value, regarded a preliminary result at the initial stage of applying electron cooling, is attributed to the pedestal observed in the Schottky spectra at that time [20]. The width measured in the present study agrees well with most of the calculated values listed in table 3.1, the most remarkable exception being the value obtained by Tang

et al. in a hyperspherical close-coupling calculation [10]. The inadequacy of this approach might have been expected on the basis of a comparison of the calculated cross section with the experimental results of Bryant *et al.* where the measured strength appeared to be much larger than predicted [10]. The widths obtained by Sadeghpour *et al.* [14], and Cortés and Martin [29], applying R -matrix- and L^2 methods, respectively, are outside the uncertainty of the present value. The calculation of Sadeghpour *et al.* in addition predicts a resonance energy that deviates from the experimental value which, within the quoted uncertainty, agrees with those of all the other approaches. It should be noted that the improved resolution of the present experiment does not allow a more accurate determination of the resonance energy than previously reported. The uncertainty of this parameter is limited by the uncertainty of the D^- beam orbit length [20]. The complex-rotation method applied in different variants by Ho [27], Lindroth *et al.* [16, 17], Kuan *et al.* [32], Chen [33] and Bylicki and Nicolaides [15] seems to provide a good description of the structure of the negative hydrogen ion. The measured magnitude of q agrees very well with the few theoretical predictions for this parameter [16, 29, 30] but this is to be expected since the q value couples to the width.

3.4 Conclusion

The natural width Γ and the asymmetry parameter q of the $^1P^o\ 2\{0\}_3^-$ resonance of D^- have been determined to a precision that, for the first time, has allowed a critical test of the various theoretical models applied to this system. The measurement was performed with the technique of Doppler-tuned VUV spectroscopy, for which the resolution was improved by a factor of ~ 4 with respect to previous experiments by electron cooling the D^- beam. The energy resolution obtained in the present experiment cannot be improved much further, given the machine properties of the storage ring and the electron cooler, and will make an observation of the last member of the $2\{0\}_m^-$ series, the $^1P^o\ 2\{0\}_5^-$ resonance, difficult. Figure 3.6 (a) shows the cross section in the vicinity of this resonance as predicted by Lindroth, with the $2p_{1/2}$, $2s$ and $2p_{3/2}$ thresholds of $\text{D}(n=2)$ indicated by vertical lines. In figure 3.6 (b) this cross section has been convolved with the present experimental resolution, and the ratio of the resonant to off-resonant contribution is seen to be ~ 1.4 with the $2p_{1/2}$ threshold being completely buried in the high-energy shoulder of the $2\{0\}_5^-$ resonance. Given the decrease in strength by a factor of ~ 700 when going from the $2\{0\}_3^-$ to the $2\{0\}_5^-$ state [16], this structure can only be verified beyond statistical uncertainty by increasing the data-collection time by at least a factor of 50, assuming a grating efficiency similar to that of the 1996–97 experiments. Since the collection time for each data point is

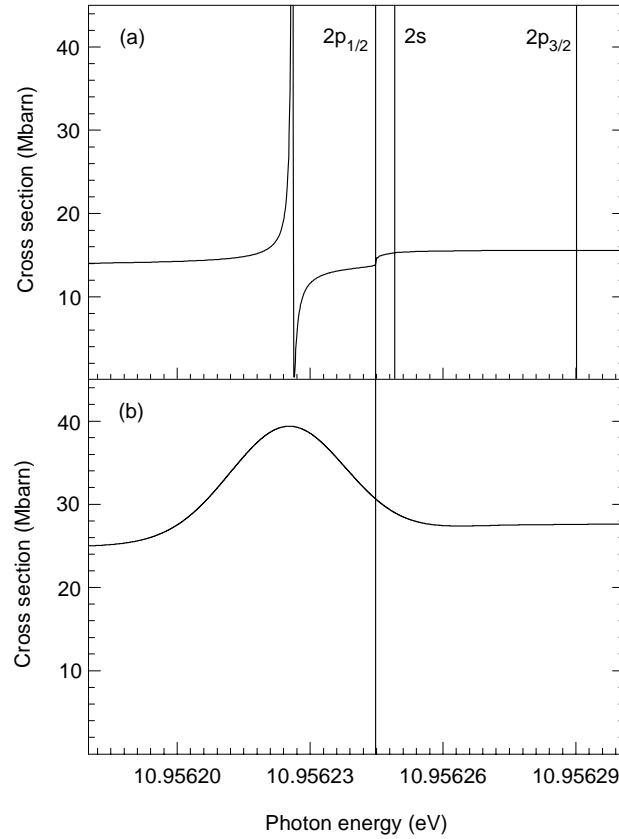


Figure 3.6: (a) Theoretically predicted photodetachment cross section of D^- in the vicinity of the $^1P^o \ 2\{0\}_5^-$ resonance of D^- , with the $2p_{1/2}$, $2p_{3/2}$ and $2s$ thresholds of $D(n=2)$ indicated by the vertical lines [16]. (b) A convolution of the cross section from (a) with the experimental resolution of $\sim 44 \mu\text{eV}$ (FWHM).

a few minutes with a favourable photon flux, this seems a somewhat unrealistic task considering the demands to experimental stability and the limited outcome expected from such an experiment. Although a grating with an improved 118 nm reflection efficiency had been provided for the November 2000 beamtime, a search for the $2\{0\}_5^-$ resonance was therefore not attempted. Instead, a re-investigation of the $2\{0\}_2^+$ shape resonance was performed, utilizing a newly developed, improved ion-beam positioning system which was expected to eliminate the drift in the laser- and ion-beam overlap when scanning the ion-beam energy (cf. the apparent strange shape of this resonance

in figure 3.1) [19]. The shape resonance has been investigated a couple of times by Bryant *et al.* yielding values for the width in the 20–30 meV range while recent theoretical predictions agree on a value around 20 meV [15]. The beam-positioning system appeared to work well but a further evaluation of the success of this experiment will have to await the data analysis which remains to be done.

Considering the series converging to the $\text{H}(n=3)$ threshold, the ${}_3\{0\}_3^+$ and ${}_3\{0\}_4^+$ Feshbach resonances have been observed by Bryant *et al.* at 12.650(1) eV and 12.837(4) eV, respectively, applying the doubtful energy calibration method mentioned previously [7, 35]. With widths of ~ 30 meV and ~ 2 meV and strengths comparable to those of the ${}_2\{0\}_3^-$ and ${}_2\{0\}_4^-$ resonances, these states should be easily observable at ASTRID. The intervening ${}_3\{0\}_4^-$ and ${}_3\{0\}_5^-$ resonances of widths ~ 20 μeV and ~ 6 μeV [16, 17] have never been observed, but even the lowest-lying one represents an experimental challenge since the strength is a factor of ~ 3 lower than that of the ${}_2\{0\}_5^-$ resonance.

As an alternative to—or extension of—the present technique, one could consider the use of a tunable VUV light source in an ordinary collinear beam-line setup with a low-energy ($\sim \text{keV}$) H^- beam. With such a setup the resolution would be limited by the spectral bandwidth of the VUV light source since the contribution from the velocity spread of the accelerated ion beam would be much smaller [36, 37]. The resolution could thus be improved by at least another factor of ~ 4 by the application of VUV light generated by, e.g., the 5th or 7th harmonic of a nanosecond dye laser. The one- or two-order-of-magnitude reduction in VUV flux implied by the off-resonant phase-matching conditions would likely be compensated by the improved resolution.

References

- [1] A. R. P. Rau, *J. Astrophys. Astron.* **17**, 113 (1996).
- [2] K. R. Lykke *et al.*, *Phys. Rev. A* **43**, 6104 (1991).
- [3] G. W. F. Drake, *Nucl. Inst. Meth B* **31**, 7 (1988).
- [4] D. C. Rislove *et al.*, *Phys. Rev. A* **58**, 1889 (1998).
- [5] D. C. Rislove *et al.*, *Phys. Rev. A* **59**, 906 (1999).
- [6] H. C. Bryant *et al.*, *Phys. Rev. Lett.* **38**, 228 (1977).
- [7] M. E. Hamm *et al.*, *Phys. Rev. Lett.* **43**, 1715 (1979).
- [8] D. W. MacArthur *et al.*, *Phys. Rev. A* **32**, 1921 (1985).
- [9] P. G. Harris *et al.*, *Phys. Rev. A* **42**, 6443 (1990).
- [10] J. Tang *et al.*, *Phys. Rev. A* **49**, 1021 (1994).
- [11] E. Lindroth, *Phys. Rev. A* **52**, 2737 (1995).
- [12] P. Balling *et al.*, *Phys. Rev. Lett.* **77**, 2905 (1996).
- [13] H. H. Andersen *et al.*, *Phys. Rev. Lett.* **79**, 4770 (1997).
- [14] H. R. Sadeghpour *et al.*, *Phys. Rev. A* **45**, 1587 (1992).
- [15] M. Bylicki and C. A. Nicolaides, *Phys. Rev. A* **61**, 052508 (2000).
- [16] E. Lindroth *et al.*, *Phys. Rev. A* **57**, R685 (1998).
- [17] A. Bürgers and E. Lindroth, *Eur. Phys. J. D* **10**, 327 (2000).
- [18] T. Purr and H. Friedrich, *Phys. Rev. A* **57**, 4279 (1998).

- [19] J. S. Nielsen and S. P. Møller, in *Proc. Sixth European Particle Accelerator Conf. (EPAC98)*, edited by S. Myers *et al.* (<http://www.cern.ch/accelconf/>, Stockholm, 1998).
- [20] P. Balling *et al.*, Phys. Rev. A **61**, 022702 (2000).
- [21] H. Poth, Phys. Rep. **196**, 135 (1990).
- [22] L. H. Andersen *et al.*, Phys. Rev. A **41**, 1293 (1990).
- [23] S. Pastuszka *et al.*, Nucl. Inst. Meth. A **369**, 11 (1996).
- [24] J. S. Nielsen, Nucl. Inst. Meth. A **441**, 150 (2000).
- [25] J. Marriner *et al.*, Part. Accel. **30**, 13 (1990).
- [26] W. H. Press *et al.*, *Numerical Recipes in Pascal* (Cambridge University Press, England, 1992).
- [27] Y. K. Ho, Chin. J. Phys **29**, 327 (1991).
- [28] T. N. Chang, Phys. Rev. A **47**, 705 (1993).
- [29] M. Cortés and F. Martin, Phys. Rev. A **48**, 1227 (1993).
- [30] M. Venuti and P. Declava, J. Phys. B **30**, 4839 (1997).
- [31] T. T. Gien, J. Phys. B **31**, L1001 (1998).
- [32] W. H. Kuan *et al.*, Phys. Rev. A **60**, 364 (1999).
- [33] M.-K. Chen, J. Phys. B **32**, L487 (1999).
- [34] P. J. Mohr and B. N. Taylor, J. Phys. Chem. Ref. Data **28**, 1713 (1999).
- [35] S. Cohen *et al.*, Phys. Rev. A **30**, 4728 (1987).
- [36] R. Neugart, Nucl. Inst. Meth. **186**, 165 (1981).
- [37] U. V. Pedersen, *Studies of Weakly Bound Atomic Negative Ions* (Master's thesis, Institute of Physics and Astronomy, Aarhus University, Denmark, 2000).

Chapter 4

Lifetimes of molecular negative ions

4.1 Introduction

Most of the negative ions that are unstable in the ground state exist in metastable states associated with excited parent states of the corresponding neutral system or, for molecules, with the ground state of the neutral molecule. At present no clear definition of metastability exists, and I will, following Blondel [1], regard a state as metastable if it is long-lived enough that it can be detected along a beam-line. By this definition, states with lifetimes as short nanoseconds may be considered metastable but the emphasis of the present chapter is on the μs – ms range. For a state to be that long-lived, decay via photon- and electron emission must be forbidden by the radiative- and autodetachment selection rules, imposing for molecular negative ions some restrictions on the electronic potential-energy curve associated with the metastable state. First, the minimum of the curve must be attained below the energy of a (possibly excited) electronic state of the neutral system evaluated at the same bond length and (eventual) bend angle, i.e. the vertical electron affinity must be positive. Second, unless the minimum of the potential-energy curve of the negative-ion state is energetically located below that of the neutral state (referred to as positive adiabatic electron affinity), the minima of the potential-energy curves must be located at sufficiently different bond lengths and/or bend angles that the detachment probability can be considered small. This means that a barrier must be surpassed in order for autodetachment to occur, or stated another way: the Frank-Condon overlap between the states must be small. Third, if the potential-energy curve

of the negative ion is associated with an excited electronic state of the neutral molecule, decay to lower-lying (less stable) states by photon- or electron emission must be prohibited. This is, for example, ensured by the spin of the metastable state being sufficiently different from that of any of the lower-lying neutral- or negative-ion states. Most of the metastable negative-ion states characterized so far are high-spin (≥ 4) states prevented from decaying to the singlet- or doublet ground state of the neutral atom or -molecule. One could, in principle, also imagine the reverse situation of a high-lying low-spin state being prevented from decaying to a high-spin ground state. Such a situation will, however, never be encountered since the high-spin state will always be accompanied by low-spin states derived from a common (dominant) parent electronic configuration [2, 3].

As discussed in chapter 2, He^- and Be^- exist as metastable quartet states with lifetimes in the μs range. In addition, a whole range of high-lying, high-spin states have been predicted for H^- through Ca^- , Al^- , Fe^- , Mn^- and Cu^- by Bunge *et al.* and Nicolaides *et al.* [4, 5, 6]. Some of these states can be grouped according to their open-shell structure with unpaired electronic spins, including the $2p^2\ ^3P$ state of H^- , the $2p^3\ ^4S$ state of He^- and the $1s2p^3\ ^5S$ state of Li^- [6]. The 3P state of H^- can only be created by the simultaneous absorption of a VUV photon and attachment of an electron to the neutral hydrogen atom and has never been experimentally observed. The 4S and 5S states of He^- and Li^- , respectively, have been experimentally verified by virtue of their radiative decay to lower-lying $1s2p^2\ ^4P$ and $1s2s2p^2\ ^5P$ states as observed in optical emission spectra of the beam-foil-excited negative ions [7, 8]. The $1s2s2p^2\ ^5P$ state of Li^- is predicted to be metastable with a lifetime that may be expected to be several μs by an extrapolation from the analogous state of the iso-electronic Be atom [9].

Considering molecular negative ions, recent mass-spectroscopic detections of long-lived CO^- and N_2^- ions [10] together with the studies of N_2^- and CO_2^- presented in the present chapter have stimulated theoretical interest in the sextet states of these systems as well as of CS^- which is stable in the ground state [11]. Prior to these studies, sextet states of negative molecular ions have, to my knowledge, never been considered. High-lying quintet states, which may be considered potential parents for anion sextet states, have been predicted for the neutral molecules of AlB [12], AlN [13], MgC [14], O_2 [15] and TiH_2 [16]. By the nature of such states, their identification represents a challenge to experimentalists since they can only be generated non-selectively in discharges or sputter-ion sources under rather un-controlled conditions.

The present chapter is concerned with measurements of autodetachment lifetimes of metastable states of N_2^- and CO_2^- , for which previous lifetime values were either absent (N_2^-) or poorly determined (CO_2^-). The exper-

iments have been performed by means of a time-of-flight technique at the storage ring ASTRID, which to a first approximation can be considered an infinitely long beam-line. Since the ions are confined by magnets to circulate in the ring until they decay, i.e. are neutralized, lifetimes in the μs – ms range, inaccessible to direct beam-line experiments, can be measured. ASTRID has previously been successfully applied for measurements of autodetachment lifetimes of the metastable quartet states of He^- [17], Be^- [18], Ba^- [19] and He_2^- [20] in the $50\ \mu\text{s}$ – $10\ \text{ms}$ range with an uncertainty of 5–10 %. Following the measurements reported here, uncertainties of $\leq 1\%$ have been demonstrated by measurements on He^- [21, 22] and Be^- [23], using the alternative approaches of an electrostatic ion trap [21, 23] and a newly developed electrostatic storage ring, ELISA, at Aarhus University [22]. ELISA is of only 7.6 m circumference which is an advantage, given the fact that the lower limit to the lifetimes which can be measured with the storage-ring technique is determined by the revolution time of the ions in the ring. In addition, ELISA is compact enough that it can be cooled to below -50°C , allowing the influence of black-body radiation-induced photodetachment to be investigated over a wide temperature range [22]. The capability of ELISA has already been demonstrated by lifetime measurements on He^- [22], Ba^- [24] and H_2CC^- [25], spanning the impressive range of $10\ \mu\text{s}$ – $110\ \text{s}$. In order to separate the 110 s autodetachment lifetime of H_2CC^- from that of collisional detachment, measurements were performed at different pressures by leaking H_2 gas into the ring [25].

4.2 Notation and molecular quantum numbers

Since the nomenclature for the labelling of molecular electronic states differs somewhat from that of atoms, especially for bent molecules, a brief introduction will be given here before proceeding to the experiments. The idea behind the quantum-number designation is indicated by considering the representative example of H_2O which has a bent $\text{H}-\text{O}-\text{H}$ ground-state geometry. It thus belongs to the symmetry point group C_{2v} , which has three symmetry elements—a two-fold rotation axis and two different mirror planes—two of which are independent [26]. The single-electron energy levels can be shown to be non-degenerate, implying the molecular orbitals to be symmetric or anti-symmetric with respect to the two independent symmetry operations [27]. Four different kinds of orbitals named a_1 , a_2 , b_1 and b_2 are thereby obtained, from which electronic configurations with total symmetry properties designated A_1 , A_2 , B_1 or B_2 can be build. Each of these configurations is a simultaneous eigenstate of an element of the symmetry group and the total molecular Hamiltonian (i.e. including the nuclear and electronic motions) and

is said to generate, or form the basis for, a one-dimensional representation of the symmetry group [28].

For linear molecules the two-dimensional spherical symmetry imposes on the energy levels a degeneracy given by the number of different m_l values allowed, where m_l is the quantum number associated with the projection L_z of the angular momentum operator L along the inter-nuclear axis [29]. The single-electron orbitals are now eigenfunctions of L_z and named σ , π , δ etc. in analogy with atomic orbitals (three-dimensional spherical symmetry). Disregarding spin, m_l attains the values $0, \pm 1, \pm 2 \dots$, corresponding to nondegenerate σ orbitals and doubly degenerate $\pi, \delta \dots$ orbitals. The orbitals are designated indices g (gerade) and u (ungerade) according to their parity, and, if nondegenerate (σ states), indices $+$ and $-$ referring to symmetry or antisymmetry with respect to reflection in any plane containing the internuclear axis [29]. Configurations with terms Σ, Π, Δ etc. can be build by application of the rules for coupling of angular momenta, again reflecting the geometrical symmetry of the molecule since angular momentum is the generator of rotation.

4.3 Experimental setup

The negative ions to be studied were formed either directly in a sputter-ion source [30] or from positive molecular ions produced in a plasma-type ion source [31] and passed through a charge-exchange cell with potassium vapour. In the sputter-ion source a chemical compound containing the constituent atoms of the molecule to be studied is sputtered with Cs^+ ions. The electrons needed for the negative-ion formation are provided by the electro-positive Cs atoms present in the source. For the CO_2^- measurements, a chemical compound containing C and O atoms was not readily available, and CO_2 gas was let in to a Ti cathode sputtered with Cs^+ ions. In the plasma-type ion source singly-charged positive molecules are created by electron bombardment of the corresponding neutral gas-phase molecules. All kinds of negative-ion states may be formed by sputtering, while restrictions on the spin and energy of the states are imposed by the charge-exchange process.

Following mass- and charge-state analysis, a 100 keV pulsed negative-ion beam was injected into the storage ring ASTRID, which has been briefly described in chapter 3. Neutral molecules generated on the preceding straight section and undeflected by the bending magnets were monitored by a micro-channel plate detector at one corner of the ring as a function of time after injection. The revolution time of ions in the ring, which for CO_2^- at 100 keV is 60 μs , sets the lower limit for the lifetimes that can be measured by this

method. The upper limit is determined by collisional detachment due to rest gas, resulting in 1–5 s mean lifetimes of stable negative ions with binding energies exceeding 150 meV [32]. Ions with smaller binding energy are, in addition, detached by black body radiation, limiting their lifetimes to ~ 100 ms [33].

4.4 N₂⁻

Short-lived resonance states of N₂⁻ have long been observed in electron-scattering experiments with the lowest-lying one, the ²Π_g shape resonance, energetically located ~ 2.4 eV above the ¹Σ_g⁺ ground state of N₂ [34]. Only recently a metastable state of N₂⁻ was detected in a mass spectrometer by Gnaser [35] and at a tandem accelerator by Middleton and Klein [10] upon sputtering of TiN and TiAlN surfaces, respectively. The conversion efficiency was estimated to one metastable N₂⁻ ion formed per 10⁷ sputtered N atoms [35] and a mean lifetime of 183(30) μs determined from a measurement of the decay rate on a 60 cm travel distance. This lifetime measurement did not account for an estimated ~ 20 % contamination of the N₂⁻ beam with Si⁻ (also mass 28) [10]. Subsequently, Sommerfeld and Cederbaum considered the ⁴Π_u and ⁴Σ_g⁻ states of N₂⁻ as possible candidates responsible for the observed long-lived ions [36]. The ⁴Π_u state of configuration $1\sigma_g^2 1\sigma_u^2 2\sigma_g^2 2\sigma_u^2 3\sigma_g^2 1\pi_u^3 1\pi_g^2$ is formed by attachment of a $1\pi_g$ electron to the lowest-lying ³Σ_u⁺ state of N₂, obtained by excitation of a $1\pi_u$ electron from the $1\sigma_g^2 1\sigma_u^2 2\sigma_g^2 2\sigma_u^2 3\sigma_g^2 1\pi_u^4$ ¹Σ_g⁺ ground state of N₂. The ⁴Σ_g⁻ state of configuration $\dots 3\sigma_g^1 1\pi_u^4 1\pi_g^2$ is formed by attachment of a $1\pi_g$ electron to the ³Π_g state of N₂ which has the configuration $\dots 3\sigma_g^1 1\pi_u^4 1\pi_g^1$. The potential-energy curves associated with these quartet states and their neutral triplet parent states, were calculated at the CCSD(T) level of theory, using a AUG-cc-pVTZ basis set (cf. chapter 2). The adiabatic electron affinities were deduced to be negative, -0.11 and -0.32 eV for the ⁴Π_u and ⁴Σ_g⁻ states, respectively, but with the possibility of stabilization of the ⁴Π_u state at a higher level of calculation (see figure 4.1). As argued by Sommerfeld and Cederbaum, even with a negative adiabatic electron affinity, the ⁴Π_u state may, in principle, be long-lived enough for a mass-spectroscopic observation due to a relatively poor Frank-Condon overlap.

The present experiment was stimulated by the prospect of providing evidence for or against the theory of a quartet state by investigating the possibility of generating long-lived N₂⁻ ions by sputtering or charge exchange. Besides, a lifetime measurement taking the Si⁻ contamination into account was aimed at.

No sign of long-lived N₂⁻ ions was observed by passage of a ~ 1 μA N₂⁺

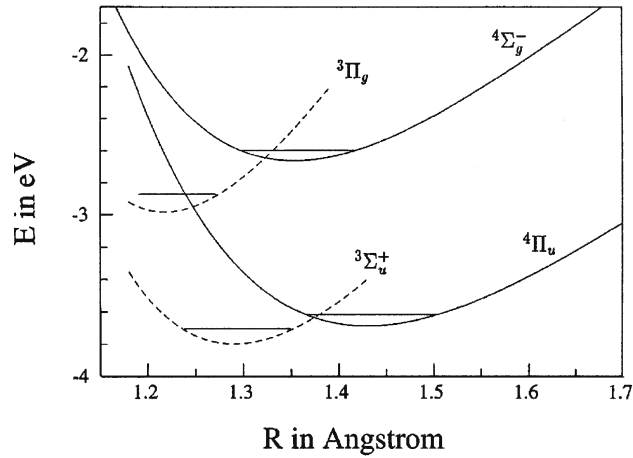


Figure 4.1: Potential-energy curves for the $4\Pi_u$ and $4\Sigma_g^-$ states of N_2^- and the associated $3\Sigma_u^+$ and $3\Pi_g$ parent states of N_2 calculated by Sommerfeld and Cederbaum [36].

beam through the charge-exchange-cell, in agreement with a negative result previously reported by Bae *et al.* [37]. From further investigations at the Aarhus Tandem Accelerator an upper limit of 5×10^{-10} for the conversion efficiency of N_2^+ ions to N_2^- ions could be estimated [38]. There, the N_2^- ion formation process was studied with a stripping technique which allowed the masses of N_2^- and Si^- to be separated. Long-lived N_2^- ions were detected upon sputtering of TiN and BN surfaces, but could not be generated from NaN_3 . Considering the differing chemical environment of N atoms bound in the three compounds, it seems likely that the long-lived N_2^- ions are formed by interaction between two sputtered N atoms and not from a precursor like, e.g., N_3^- present in NaN_3 .

A ~ 25 pA beam of N_2^- ions generated by sputtering of TiN was used for the lifetime measurement. Since the TiN compound was expected to be contaminated with Si from pump-oil deposits, a reference measurement was performed on a pure Si^- beam produced by sputtering of a pure Si surface. Present in the Si^- decay were a stable component and a short-lived component fitted to 2.0 ± 0.2 ms, with the stated uncertainty reflecting the span of lifetimes obtained when disregarding data-points corresponding to the first few round-trips in the ring. Since Si^- is known to possess the three stable states $4S$, $2D$ and $2P$ with binding energies of 1.39 eV, 0.53 eV and ~ 30 meV, respectively [39], the long-lived component must be attributed to the $4S$ and $2D$ states with the 2 ms component left for the $2P$ state. A typical decay for N_2^- is shown on a semilogarithmic scale on figure 4.2, illustrating a

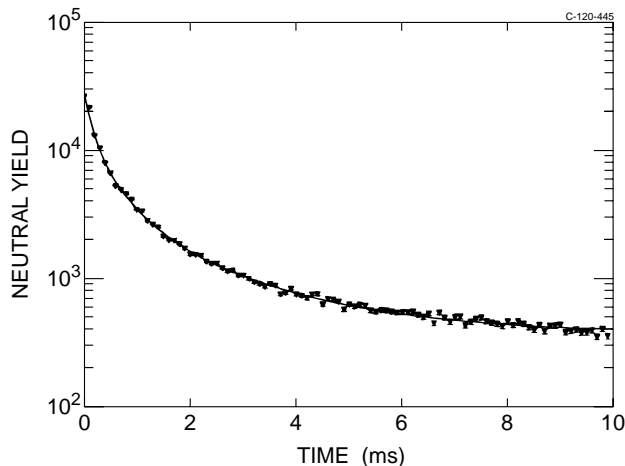


Figure 4.2: Semilogarithmic plot of the N_2 signal as a function of time after injection for a 100 keV N_2^- beam. The solid curve represents a fit to four exponentials.

number of not clearly resolvable lifetime components. A stable component is present in the decay and is attributed to the presence of Si^- . When fitting the data, two of the components were therefore fixed at the values dictated by the Si^- decay curve. The minimum number of exponentials required to give a reasonable fit is four, meaning that at least two different N_2^- lifetime components are present. Due to the very rapid initial decay, only the first three data points could be disregarded in the fit, which is just on the edge of influence from initial state effects. The result thus obtained are N_2^- lifetimes of $120 \pm 13 \mu s$ and $515 \pm 25 \mu s$, with the major contribution to the uncertainty arising from the removal of data points.

The fact that the long-lived N_2^- ions cannot be generated by charge exchange provides evidence against a long-lived quartet state of N_2^- which has as a parent a triplet state of N_2 . The present result has stimulated Veseth to re-calculate the potential-energy curves associated with the $^4\Pi_u$ and $^4\Sigma_g^-$ states, using a many-body perturbation method for general spaces [38]. An adiabatic electron affinity of -0.32 eV was obtained for the $^4\Pi_u$ state, while the $^4\Sigma_g^-$ state was found to be bound with respect to the $^3\Pi_g$ state of N_2 but unstable with respect to autodetachment to the $^3\Sigma_u^+$ state of N_2 .

Attention was subsequently drawn to the sextet states $\dots 1\pi_u^3 3\sigma_g^1 1\pi_g^2 3\sigma_u^1$ $^6\Pi_g$ and $\dots 1\pi_u^2 3\sigma_g^2 1\pi_g^2 3\sigma_u^1$ $^6\Sigma_u^+$ of N_2^- associated with the quintet parent states $\dots 1\pi_u^3 3\sigma_g^1 1\pi_g^2$ $^5\Pi_u$ and $\dots 1\pi_u^2 3\sigma_g^2 1\pi_g^2$ $^5\Sigma_g^+$ of N_2 , respectively. Using the CASSCF approach with a AUG-cc-pVTZ basis set, Olsen predicted both

of the sextet states to be located below both of the quintet parent states and to be stable with respect to autodetachment and photon emission [38]. Equilibrium bond lengths of 2.48 Å and 2.65 Å were obtained for the ${}^6\Sigma_u^+$ and ${}^6\Pi_g$ states, respectively, and the minima of the potential-energy curves were attained at equal energies within the accuracy of the calculation. These results were later found to be in qualitative agreement with CCSD(T) calculations by Dreuw and Cederbaum, predicting the ${}^6\Sigma_u^+$ state to be lowered by ~ 0.5 eV with respect to the ${}^6\Pi_g$ state [40]. They also found the ${}^5\Sigma_g^+$ minimum to be located at a somewhat lower energy, in fact coinciding with that of the ${}^6\Sigma_u^+$ state but at a very different bond length. Dreuw and Cederbaum have performed similar calculations on the iso-electronic CO^- ion, predicting a ${}^6\Pi_g$ potential-energy curve with a shallow minimum at a bond length of 3.5 Å, while that of the ${}^6\Sigma_u^+$ state is entirely repulsive [41]. The loosely bound ${}^6\Pi_g$ state of CO^- can be considered the result of a C^- ion bound with respect to the dipole that it induces to the O atom [41]. This picture certainly does not carry on to the sextet states of N_2^- due to the instability of N^- . The ${}^6\Pi_g$ state of CO^- should probably be associated with long-lived CO^- ions observed by Middleton and Klein in a mass spectrometer [10], while the long-lived N_2^- ions of the present experiment can be attributed to the ${}^6\Sigma_u^+$ state. This assignment is supported by optical emission studies of N_2 molecules formed in sputtering, providing signatures of N_2 formation in the ${}^5\Sigma_g^+$ state by the recombination of two sputtered $\text{N}(^4S)$ atoms [42]. This also agrees with the observation at the Aarhus Tandem Accelerator that long-lived N_2^- ions could be generated from TiN and BN but not from NaN_3 [38].

4.5 CO_2^-

The existence of metastable, autodetaching CO_2^- ions in the gas phase was first reported in 1970 by Paulson [43], who studied reactions of O^- with CO_2 . Subsequently, Cooper and Compton observed formation of metastable, autodetaching CO_2^- ions in collisions of electrons or Cs atoms with cyclic anhydrides containing as a basic unit CO_2 with a bend angle of 120° [44, 45]. The lifetimes of the produced species were measured with a time-of-flight spectrometer to be $26 \pm 5 \mu\text{s}$ and $60 \pm 5 \mu\text{s}$ by electron impact, and $71 \pm 10 \mu\text{s}$ and $62 \pm 10 \mu\text{s}$ by Cs collisions for succinic anhydride ($\text{C}_4\text{H}_4\text{O}_3$) and maleic anhydride ($\text{C}_4\text{H}_2\text{O}_3$), respectively. The observation of two distinct lifetimes was explained by the population of different vibrational levels of the same electronic state, with the long lifetime attributed to the lowest vibrational level, exhibiting the smallest Frank-Condon overlap with the neutral parent state. A study of CO_2^- ions formed in collisions of alkali-metal atoms with

linear CO₂ molecules resulted in a mean lifetime of $90 \pm 20 \mu\text{s}$ and a value of $-0.6 \pm 0.2 \text{ eV}$ for the adiabatic electron affinity of the CO₂ ground state which was considered the parent state of the observed metastable species [46]. If attributed to the lowest ro-vibrational state, the lifetime $90 \pm 20 \mu\text{s}$ is in agreement with calculations by Rauk *et al.* [47]. The measured electron affinity of CO₂ is also in agreement with the theoretical value of -0.67 eV reported recently by Gutsev *et al.* who have calculated the potential-energy curves for the lowest-lying electronic states of CO₂ and CO₂⁻, $^1\Sigma_g^+$ and 2A_1 , respectively [48]. While the ground state of CO₂ is linear, the minimum of the potential-energy curve of CO₂⁻ is obtained at a bend angle of 138° and energetically located below the ground-state potential-energy curve of CO₂ evaluated at this angle [48]. The metastability of the observed CO₂⁻ state and the non-existence of stable linear CO₂⁻ ions [49] are thus accounted for by the characteristics of the ground-state potential-energy curves. Recently, Middleton and Klein have detected CO₂⁻ ions by accelerator mass spectrometry upon sputtering of a Ti cathode with a 0.5 mm diameter hole drilled perpendicularly through the surface for CO₂ gas inlet [10]. A lower limit of $170 \mu\text{s}$ for the lifetime was estimated with no comments as to the possible identity of the state in question. Finally, Schröder *et al.* studied the formation of CO₂⁻ from CO₂⁺ ions by charge exchange in Xe gas and from collisional activation of carboxylate ions, by means of a mass-spectrometric technique [50]. The motivation for using Xe is the similarity of its ionization potential with that of CO₂, favouring the formation of CO₂⁻ ions in the lowest-lying electronic state, 2A_1 . A lower limit of $50 \mu\text{s}$ was estimated for the autodetachment lifetime of the generated CO₂⁻ ions.

The purpose of the present experiment was a test and improvement of the above mentioned results with the condition that the method of CO₂⁻ ion formation applied might influence the outcome of the experiment. Long-lived CO₂⁻ ions were produced either directly in a sputter-ion source [30] or by charge exchange of CO₂⁺ ions. By the sputter process, CO₂ gas was let in to a Ti cathode sputtered with Cs⁺ ions, resulting in a 0.15 nA CO₂⁻ beam. For the charge-exchange process, a $1 \mu\text{A}$ beam of CO₂⁺ ions produced in a plasma type ion source was guided through the charge-exchange cell where a minor fraction was converted to CO₂⁻ ions.

Considering first the long-lived CO₂⁻ ions formed by charge-exchange, the negative-ion beam had decayed completely after $\sim 50 \text{ ms}$. A typical decay of the neutral-molecule signal as a function of time after injection is shown on a semilogarithmic scale in figure 4.3. The spread in data points reflects betatron oscillations of the ions in the ring, causing the detection efficiency of neutrals to vary due to the finite detector size. In the data processing, the uncertainty thereby introduced is accounted for by fitting the decay curve

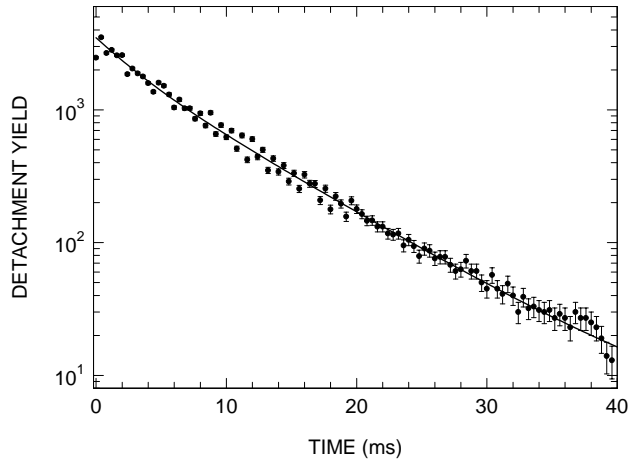


Figure 4.3: Semilogarithmic plot of the detachment yield versus time after injection for a CO_2^- beam produced by charge exchange of CO_2^+ ions. The solid curve represents a fit to two exponentials and a constant background. Error bars represent a statistical uncertainty of one standard deviation.

repeatedly, successively disregarding more and more data points from the left (short times). In any case, data points corresponding to the first few revolutions of ions in the ring are disregarded, since they could be influenced by initial state effects like, e.g., slit scattering of the beam. While the absence of a long-lived (1–5 s) component was expected, the presence of one or more millisecond components instead of the expected $\sim 90 \mu\text{s}$ component is surprising. Showing a slight systematic deviation from linearity on a semilogarithmic scale, the data were fitted to two exponentials added to a constant background, as measured with no ions in the ring. By this procedure, lifetimes of $3.3 \pm 0.4 \text{ ms}$ and $7.8 \pm 0.3 \text{ ms}$, respectively, were obtained for the data presented in figure 4.3. The two lifetimes may be attributed to different vibrational levels of the same electronic state and are sufficiently close that more than two components may be hidden in the decay. The values stated should thus be considered vibrational averages, sensitive to the conditions prevailing in the ion source.

The resolution of the experiment would have permitted observation of the $\sim 90 \mu\text{s}$ component, if represented by at least $\sim 1 \%$ of the CO_2^- ions. The apparent absence of such CO_2^- ions may be explained by the production method applied. Assuming the CO_2^+ ions from the ion source to be in the $^2\Pi_g$ ground state upon entering the charge-exchange cell and considering the ionization energies of 13.76 eV and 4.33 eV for CO_2 [51] and potassium, respectively,

the lowest-lying CO₂⁻ state is probably not reached. Electron capture by CO₂⁺(²Π_g) ions will populate highly excited states of CO₂, and subsequent electron capture may likely lead to the formation of CO₂⁻ in an excited state that happens to be long-lived. Starting out from the doublet CO₂⁺ state, the long-lived CO₂⁻ state must be bound to a singlet or triplet state of CO₂ and therefore either be a doublet or quartet state. Whether these states of CO₂ and CO₂⁻ are bent or linear are open questions, since the charge-exchange process leaves a scope of at least 2×4.33 eV for their energies. Besides, the mapping of electronic excited states of CO₂ is far from being complete with only the lowest excited singlet and triplet state energies being calculated by Spielfiedel *et al.* [52]. They have considered the ^{1,3}Σ_u⁻, ^{1,3}Σ_u⁺, ^{1,3}Δ_u and ^{1,3}Π_g states associated with the 1σ_g²1σ_u²2σ_g²2σ_u²3σ_g²3σ_u²4σ_g²1π_u⁴1π_g³2π_u¹ and ...1π_u⁴1π_g³5σ_g¹ linear electronic configurations, obtained by excitation of a 1π_g electron from the CO₂(¹Σ_g⁺) ground state of electronic configuration ...1π_u⁴1π_g⁴. According to the Walsh rules, these linear configurations correlate with bent ^{1,3}A₂ and ^{1,3}B₂ states that either raise or lower the energy with respect to the corresponding linear states [51]. If such a bent state turns out to be the energetically most favourable, it is pushed 4–5 eV down with respect to the corresponding linear state [52] and it is thus very difficult to predict the order of states without performing detailed calculations. A complete picture of the variation of equilibrium bend angle with excitation energy can therefore not yet be given. All that can be argued is that between the linear CO₂ ground state and the bent CO₂⁺ ground state there is a low-lying band of bent states and a high-lying band of linear states.

The present experimental result has stimulated theoretical investigations of the lowest-lying excited states of CO₂⁻ and their excited CO₂ parent states. The quartet states ⁴A₂ and ⁴B₂ of CO₂⁻ associated with the lowest triplet states ³B₂ and ³A₂ of CO₂, turned out to be rather short-lived [53] and further investigations therefore concentrated on higher-lying quartet states and on doublet states. The lowest-lying excited ²A₂ state of the isoelectronic NO₂ molecule is known to be metastable, decaying radiatively to the ²A₁ ground state with a lifetime of ~44 μs [54, 55]. NO₂ is bent in the ²A₁ ground state with an equilibrium angle of 133°—similar to the lowest-lying CO₂⁻ state—while the ²A₂ state is associated with a 110° geometry [56, 57]. By analogy, the observed metastable state of CO₂⁻ may be a ²A₂ state of strongly bent geometry decaying radiatively on a millisecond timescale to the CO₂⁻(²A₁) state, followed by autodetachment to the CO₂(¹Σ_g⁺) ground state with a lifetime of ~90 μs.

The possibility of an excited metastable state of CO₂⁺ surviving to the charge-exchange cell and giving rise to a CO₂⁻ state which is not a doublet or a quartet cannot be ruled out. In fact, an excited state of CO₂⁺ located

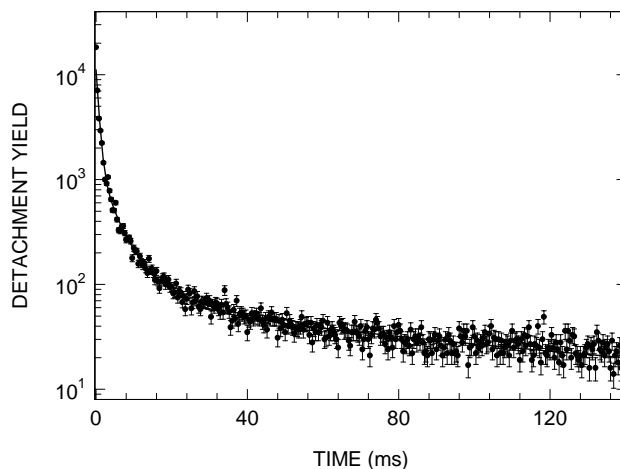


Figure 4.4: Semilogarithmic plot of the detachment yield versus time after injection for a CO_2^- beam generated by sputtering. The solid curve represents a fit to four exponentials and a constant background (see text). Error bars represent a statistical uncertainty of one standard deviation. Successive data points are separated by $400 \mu\text{s}$.

~ 10.2 eV above the CO_2^+ ground state and with a lifetime exceeding $30 \mu\text{s}$ has recently been observed and tentatively identified with the ${}^4\Pi_u$ state of 120° bend angle [58, 59]. The state was formed in an ion source by collisions of CO_2 molecules with 70 eV electrons, and with the ion source of the present experiment being operated in a similar manner, this long-lived component may have been present in the charge-exchange cell. Electron capture by such a quartet state of CO_2^+ could lead to CO_2^- ions formed in a long-lived doublet, quartet or sextet state located above as well as below the $\text{CO}_2^+({}^2\Pi_g)$ ground state. Following the present investigation, Dreuw and Cederbaum have investigated a number of sextet states as potential candidates for metastable states with a lifetime in the millisecond range [60]. Sextet states can, in terms of linear configurations, be generated from the $\dots 4\sigma_g^2 1\pi_u^4 1\pi_g^4 {}^1\Sigma_g^+$ ground state of CO_2 by exciting, e.g., two of the π -electrons to the $2\pi_u$ orbital and adding an electron to the higher-lying $5\sigma_g$ orbital. For the lowest-lying sextet, a 6A_1 state, Dreuw and Cederbaum obtained two equilibrium geometries corresponding to a linear- and a perpendicular arrangement of a C^- atom weakly bound to an O_2 molecule, respectively. The equilibrium bond lengths were rather long, 4.1 and 3.8 Å, for the linear- and perpendicular states, respectively, while the energy barriers to isomerization were 95 cm^{-1} and 19 cm^{-1} .

Turning now towards the results for the long-lived CO_2^- ions generated

by sputtering, the situation is more unclear. Present in the decay are a number of not clearly resolvable lifetime components ranging from $\sim 100 \mu\text{s}$ to $\sim 100 \text{ ms}$, as shown in figure 4.4. The decay was only monitored out to 140 ms due to a very low count rate for the $\sim 100 \text{ ms}$ component. By fixing two of the components at 3.3 ms and 7.8 ms, the decay is fitted well with four exponentials and a (separately measured) constant background if data points corresponding to the first 400 μs are disregarded. For the remaining two components, values of 89 ms and 0.68 ms are thereby obtained. The neutral yield just after injection is underestimated by this fit, shown as the solid curve in figure 4.4. Since there is no reason for believing that the distribution over (vibrational) states should resemble that of the charge-exchange process, the data have also been fitted to three- and four freely varying exponentials, respectively. With three exponentials the very fast initial decay cannot be accounted for. Disregarding only the first 200 μs and fitting to four exponentials yields values for the the shortest- and longest-living components in the ranges 80–190 μs and 120–150 ms, respectively with the remaining two components ranging in the intervals 7.5–9.6 ms and 1.1–1.3 ms, respectively. The shortest-living component may indicate the presence of CO₂⁻ ions in the lowest-lying state, ²A₁, and some of the millisecond components may be attributed to the unknown excited state(s) observed in the charge-exchange process. The $\sim 100 \text{ ms}$ component representing $\sim 20\%$ of the ions could be attributed to a very long-lived excited state of CO₂⁻ not populated by the charge-exchange process. It could, however, also indicate contamination with a stable negative ion of mass 44 with a sufficiently low binding energy that it is sensitive to photodetachment by blackbody radiation. One possible candidate is N₂O⁻, for which a positive- as well as a negative adiabatic electron affinity have been suggested [47, 61]. Previous studies of the influence of blackbody radiation on weakly-bound negative ions like Ca⁻, Sr⁻ and Ba⁻ support this conclusion [62]. In spite of the possibility for contamination by the sputter process, it may be reasonable to assume that the CO₂⁻ ions observed by Middleton and Klein [10] are formed in the same electronic state(s) as the ones prepared by charge exchange and sputtering in the present investigation. The detection mode of the present experiment is, however, not mass-specific, so the monitored neutral yield could, in principle, be fragments generated by pre-dissociation of CO₂⁻. Assuming that pre-dissociation sets the lower limit on the lifetime, the CO₂⁻ state must be even more stable with respect to autodetachment.

4.6 Conclusion

The utility of an ion-storage ring for time-of-flight measurements of autodetachment lifetimes of metastable negative ions has been demonstrated. This was illustrated by the examples of N_2^- and CO_2^- for which the lifetime measurements provided signatures of previously unobserved electronic high-spin states. The method could be used for lifetime measurements on other metastable negative ions, such as Ne_2^- [63], as well as on metastable states of stable negative ions associated with excited electronic states of the corresponding neutral molecule. In the latter case, eventual contamination of the ion beam with other stable- or metastable species would be more difficult to identify and should be carefully evaluated. In this respect, a higher degree of selectivity of the present technique would be desirable, either in the negative-ion formation or -detection process. This might be achieved by the application of a more advanced detection system, e.g. capable of mass-analyzing the neutrals generated in the autodetachment process or energy-analyzing the emitted electrons. For radiative lifetimes of bound, excited states of negative- or positive ions, selectivity can be obtained by means of laser excitation- and ionization schemes [64] or by detection of the fluorescence emitted during the decay [65]. Such approaches would obviously be very difficult to adapt to studies of autodetaching states of negative ions. The newly installed electron-beam ion source (EBIS) at ASTRID for production of multiply-charged positive ions offers an alternative possibility for selectivity in the negative-ion formation process. Recently, an experiment has been initiated, aiming at the generation of Li^- ions in the long-lived $1s2s2p^2\ ^5P$ state which may be formed from Li^{++} by the capture of three electrons in a (sequential) charge-exchange process.

The present technique is very well suited for initial tests of the existence of theoretically predicted negative-ion species, especially for ions which are expected to be on the edge of stability. Along these lines one could, e.g., search for the Mg_2^- , HeH^- , NeH^- and ArH^- ions which have been predicted to form stable, weakly-bound states [66, 67, 68]. They are examples of so-called Tango-states, representative of three-body systems consisting of two particles that are able to form a bound state and a third particle which cannot bind to any of them. The existence of such states relies entirely on electron correlation, making them important test cases for theoretical models. Other interesting ions could be H_2O^- , whose stability is still a matter of debate [69], or HCN^- which has been predicted to exist as a dipole-bound species with a 6 cm^{-1} binding energy [70].

References

- [1] C. Blondel, *Physica Scripta* **T58**, 31 (1995).
- [2] G. L. Gutsev *et al.*, *J. Phys. Chem. A* **104**, 5374 (2000).
- [3] R. D. Mead *et al.*, in *Gas Phase Ion Chemistry* (Academic Press, New York, 1984).
- [4] C. F. Bunge *et al.*, *Nucl. Inst. Meth.* **202**, 299 (1982).
- [5] C. A. Nicolaides *et al.*, *J. Molecular Structure (THEOCHEM)* **199**, 283 (1989).
- [6] N. A. Piangos and C. A. Nicolaides, *J. Phys. B* **31**, L147 (1998).
- [7] E. Träbert *et al.*, *J. Phys. B* **25**, L353 (1992).
- [8] S. Mannervik *et al.*, *J. Phys. B* **13**, L441 (1980).
- [9] C. F. Bunge, *Phys. Rev. A* **22**, 1 (1980).
- [10] R. Middleton and J. Klein, *Phys. Rev. A* **60**, 3786 (1999).
- [11] M. Hochlaf *et al.*, *J. Chem. Phys.* **110**, 11835 (1999).
- [12] C. W. Bauschlicher and S. R. Langhoff, *J. Chem. Phys.* **101**, 80 (1994).
- [13] S. R. Langhoff *et al.*, *J. Chem. Phys.* **89**, 7354 (1988).
- [14] C. W. Bauschlicher *et al.*, *Chem. Phys. Lett.* **216**, 341 (1993).
- [15] R. P. Saxon and B. Liu, *J. Chem. Phys.* **67**, 5432 (1977).
- [16] T. Kudo and M. S. Gordon, *J. Chem. Phys.* **102**, 6806 (1995).
- [17] T. Andersen *et al.*, *Phys. Rev. A* **47**, 890 (1993).
- [18] P. Balling *et al.*, *Phys. Rev. Lett.* **69**, 1042 (1992).

-
- [19] V. V. Petrunin *et al.*, Phys. Rev. Lett. **75**, 1911 (1995).
- [20] T. Andersen *et al.*, J. Phys. B **27**, 1135 (1994).
- [21] A. Wolf *et al.*, Phys. Rev. A **59**, 267 (1999).
- [22] U. V. Pedersen *et al.*, Phys. Rev. A **64**, 012503 (2001).
- [23] L. Knoll *et al.*, Phys. Rev. A **60**, 1710 (1999).
- [24] M. H. Sørensen, *Experimental Studies of Weakly-Bound Stable and Metastable Negative Ions* (Master's thesis, Institute of Physics and Astronomy, Aarhus University, Denmark, 2000).
- [25] M. J. Jensen *et al.*, Phys. Rev. Lett. **84**, 1128 (2000).
- [26] P. W. Atkins, *Molecular Quantum Mechanics* (Oxford University Press, Oxford, 1983).
- [27] G. Herzberg, *Molecular Spectra and Molecular Structure II* (D. van Nostrand Company, New York, 1960).
- [28] P. R. Bunker and P. Jensen, *Molecular Symmetry and Spectroscopy* (NRC Research Press, Ottawa, 1998).
- [29] M. Weissbluth, *Atoms and Molecules* (Academic Press, New York, 1978).
- [30] R. Middleton, Nucl. Inst. Meth. **214**, 139 (1983).
- [31] K. O. Nielsen, Nucl. Inst. Meth. **1**, 289 (1957).
- [32] L. H. Andersen *et al.*, Phys. Lett. A **162**, 336 (1992).
- [33] L. H. Andersen *et al.*, Adv. At. Mol. Phys. **38**, 155 (1997).
- [34] W. Sun *et al.*, Phys. Rev. A **52**, 1229 (1995).
- [35] H. Gnaser, Phys. Rev. A **56**, R2518 (1997).
- [36] T. Sommerfeld and L. S. Cederbaum, Phys. Rev. Lett. **80**, 3723 (1998).
- [37] Y. K. Bae *et al.*, Phys. Rev. A **29**, 2888 (1984).
- [38] T. Andersen *et al.*, Phys. Rev. A **60**, 3627 (1999).
- [39] M. Scheer *et al.*, Phys. Rev. A **58**, 2844 (1998).
- [40] A. Dreuw and L. S. Cederbaum, Int. J. Mass Spectrometry **188**, 199 (1999).

-
- [41] A. Dreuw and L. S. Cederbaum, Phys. Rev. A **59**, 2702 (1999).
- [42] K. J. Snowdon and W. Heiland, Z. Phys. A **318**, 275 (1984).
- [43] J. F. Paulson, J. Chem. Phys. **52**, 963 (1970).
- [44] C. D. Cooper and R. N. Compton, Chem. Phys. Lett. **14**, 29 (1972).
- [45] C. D. Cooper and R. N. Compton, J. Chem. Phys. **59**, 3550 (1973).
- [46] R. N. Compton *et al.*, J. Chem. Phys. **63**, 3821 (1975).
- [47] A. Rauk *et al.*, Int. J. Chem. Kinetics **26**, 7 (1994).
- [48] G. L. Gutsev *et al.*, J. Chem. Phys. **108**, 6756 (1998).
- [49] M. J. W. Boness and G. J. Schulz, Phys. Rev. A **9**, 1969 (1974).
- [50] D. Schröder *et al.*, Int. J. Mass Spectrometry **185-187**, 25 (1999).
- [51] G. Herzberg, *Molecular Spectra and Molecular Structure III* (D. van Nostrand Company, New York, 1966).
- [52] A. Spielfieldel *et al.*, J. Chem. Phys. **97**, 8382 (1992).
- [53] P. Rosmus, private communication (1999).
- [54] D. Neuberger and A. B. F. Duncan, J. Chem. Phys. **22**, 1693 (1954).
- [55] A. E. Douglas, J. Chem. Phys. **45**, 1007 (1966).
- [56] K. Aoki *et al.*, J. Chem. Phys. **105**, 2228 (1996).
- [57] E. Haller *et al.*, J. Mol. Spect. **111**, 377 (1985).
- [58] V. R. Bhardwaj *et al.*, Phys. Rev. A **58**, 2834 (1998).
- [59] R. Chawla *et al.*, Chem. Phys. Lett. **301**, 531 (1999).
- [60] A. Dreuw and L. S. Cederbaum, J. Phys. B **32**, L665 (1999).
- [61] D. G. Hopper *et al.*, J. Chem. Phys. **65**, 5474 (1976).
- [62] T. Andersen *et al.*, J. Phys. B **27**, 1135 (1994).
- [63] J. M. Millam and L. Adamowicz, Phys. Rev. A **46**, 2325 (1992).
- [64] H. B. Pedersen *et al.*, J. Chem. Phys. **109**, 5849 (1998).
- [65] J. Lidberg *et al.*, Nucl. Inst. Meth. B **152**, 157 (1999).

- [66] F. Robicheaux, Phys. Rev. A **60**, 1706 (1999).
- [67] V. Vallet *et al.*, Chem. Phys. **263**, 33 (2001).
- [68] Y. Li and C. D. Lin, Phys. Rev. A **60**, 2009 (1999).
- [69] H.-J. Werner *et al.*, J. Chem. Phys. **87**, 2913 (1987).
- [70] P. Skurski *et al.*, J. Chem. Phys. **114**, 7443 (2001).

Chapter 5

Femtosecond VUV core-level spectroscopy of surface dynamics

5.1 Introduction

Being the first and maybe only encounter of a solid with external perturbations from photons and massive particles, the surface constitutes an interesting playground for chemical processes. The most common example from everyday life is probably the corrosion of the car following its exposure to water and air. Much more beneficial are the processes of heterogeneous catalysis, in which the surface acts to increase the rate of a gas-phase reaction without being consumed itself. This is accomplished by it lowering the energy barrier which separates the chemical products from the reactants, as expressed by the so-called Arrhenius law, according to which the reaction rate scales as $\exp(-E_a/kT)$, where E_a is the activation energy of the process, T the ambient temperature and k the Boltzmann constant [1, 2]. The principle of catalysis is heavily relied on in pollution control, in the production of chemicals and for the refining of fossil fuel. The most frequently used catalyst materials are the transition metals and their compounds. These are particularly active donators or acceptors of electrons due to their partly filled electronic d -shell but not so active that the product molecules are too tightly bound to the surface to be able to escape [1]. For example, Pt, Pd and Rh are used to promote the oxidation and reduction of the harmful CO and NO_x molecules of car exhaust to CO₂ and N₂, respectively [2]. Fe is used in the synthesis of

ammonia (NH_3) from N_2 and H_2 [1] and recently, a Au-Ni alloy was found to be much more durable than pure Ni for production of the synthesis gasses H_2 and CO from methane (CH_4) [3]. The latter represents the first example of a catalyst being developed on the basis of fundamental research, aiming at an understanding on the atomic level of the mechanisms governing the action of the catalyst. Previously, catalysts have been developed on a trial-and-error basis and it was not known whether the results obtained under ultra-high vacuum conditions with well-characterized surfaces could be applied to real catalysts operating under much different conditions. Recently, it has become possible to perform well-controlled high-pressure experiments at the atomic level, and the investigated catalyst was found to behave the same way under atmospheric pressure as under ultra-high vacuum [4]. This lends support to a justification of the very large effort going on within the field of surface science towards a detailed understanding at the atomic level of the different steps involved in a surface reaction. These steps include the binding of the reactant molecules to the surface, called adsorption, the surface diffusion, bond breaking and bond formation of the reactant- and product molecules and the final escape of the product molecules from the surface, called desorption.

The focus of the present chapter is on this last desorption step of the surface reaction which on the atomic level proceeds on a femtosecond (fs) time-scale. Such a process can only be time-resolved by the application of fs laser pulses, and the past few years have seen an acceleration in experimental studies of fs laser-induced desorption, as will be described in more detail in the following section. Most of these studies have been limited to photon energies in the visible part of the spectrum, providing information about some of the time scales involved in the desorption process but only indirect information about the atomic re-arrangements associated with these time scales. Structural information can only be obtained with shorter-wavelength radiation, as applied in the traditional (static) techniques of surface science. In the present chapter an experimental setup will be described, by which the traditional synchrotron-radiation based technique of Core-Level Spectroscopy (CLS), or X-ray Photoelectron Spectroscopy (XPS), will be combined with a VUV light source of fs high-order harmonics. Previously, laser-synchrotron radiation pump-probe experiments of surface dynamics have been performed by Long *et al.* [5] and Marsi *et al.* [6], studying electron dynamics at laser-excited semiconductor surfaces and by the group of Hertel, studying the decay of an excited state of the $\text{C}_{60}/\text{Ni}(110)$ adsorbate system [7]. Semiconductor surface dynamics have, in addition, been studied by the group of Haight, using high-order harmonics tunable to ~ 80 eV [8, 9]. In these experiments a grating was applied for the wavelength selection, resulting in a time resolution in the picosecond (ps) regime. The temporal broadening is introduced by the

difference in optical path length of rays diffracted by the different grooves of the grating [10]. In order to avoid this effect, a multilayer mirror will be applied for the selection of a single harmonic order corresponding to a ~ 100 eV photon energy in our experiments.

The construction of the present setup is not complete yet, and my main contributions have been the development of the VUV light source of high-order harmonics and reflectivity tests of the multilayer mirror that will be used for the wavelength selection. In addition, I have performed the initial (static) tests at an ASTRID synchrotron-radiation beamline of systems suitable for studies with the relatively low photon energy of ~ 100 eV, achievable with the high-order harmonics. These have included the CO/Pt(111) system which was found to be inappropriate for studies with ~ 100 eV photons, and the O/Al(111) system which was considered a more "safe" candidate on account of its well-characterized core-level properties. Despite a large number of investigations of this technologically relevant system, the initial stages of the oxidation process are still not fully understood. A secondary aim of the O/Al study was to shed some more light on the oxidation mechanism, in particular the influence of the pre-treatment of the Al surface prior to adsorption.

During these preparative investigations, similar but less ambitious setups have been constructed by other groups, using either a grating for the wavelength selection or lower photon energies, created by high-harmonic generation. Karlsson and Karlsson have studied electron dynamics at a laser-excited InSb(110) surface using 9.55 eV photons [11], the group of Zacharias has recently presented a photoelectron spectrum of the CO/Ni(111) system [12] and the group of Palmer has completed a setup using 11–42 eV photons, aimed at studies of the H₂O/graphite and SF₆/graphite systems [13]. All of these groups use gratings for the wavelength selection and are thus limited to a \sim ps time resolution. Very recently, setups based on multilayer mirrors have been presented by the groups of Kapteyn [14] and Heinzmann [15], applying partially monochromatized light around 44 eV and fully monochromatized light in the 66–73 eV range, respectively. The setup of Kapteyn *et al.* was very recently applied for time-resolved measurements of valence-band photoemission spectra of the laser-excited O₂/Pt(111) system. A transient peak present in the spectra was ascribed to the dissociation of an excited superoxo (O₂⁻) or superperoxo (O₂²⁻) state while a non-transient change was attributed to desorption.

In connection with these experiments one should also mention the recent studies of anharmonic lattice dynamics [16, 17, 18] and fs laser-induced non-thermal melting [16, 19, 20, 21] of semiconductor surfaces by the groups of Falcone, Rousse, Shank and Wilson. All of these studies have applied

the technique of pico- or femtosecond X-ray diffraction, using X-rays emitted from fs laser-produced plasmas or obtained from "sliced" or time-gated synchrotron-radiation pulses (cf. chapter 1.4). The non-thermal melting process is characterized by a disordering of the crystal lattice accomplished by the sudden excitation of a large ($\sim 10\%$) fraction of the electrons from the valence band to the conduction band of the semiconductor. The lattice instability occurs before a significant amount of the electronic energy has been transferred to the lattice by electron-phonon interactions and is thus purely electronic in nature. The disordering has been observed for different laser fluences encompassing the damage threshold [19, 20, 22], below which it is found to be reversible and accompanied by a band-gap collapse for fluences near the damage threshold [23].

5.2 Laser-induced desorption

The field of photo-induced desorption of molecules from surfaces using pulsed laser light of nanosecond (ns) or femtosecond (fs) duration has undergone a rapid development within the last ten years as reflected by the large amount of review literature available on the subject [24, 25, 26, 27, 28, 29, 30, 31, 32, 33]. A chemical reaction taking place at a surface can be very different from that of the gas-phase, since the molecules are confined to aligned geometries and their chemical properties are modified by the presence of the surface [29]. In addition, a non-insulating surface acts as a heat-reservoir with an almost infinite number of degrees of freedom, interacting with the adsorbate and representing a challenge to theorists. Since the heating- or exciting laser light penetrates several atomic layers into the substrate supporting the adsorbate layer, the desorption process is much more likely the result of an adsorbate-substrate coupling than a direct laser-adsorbate interaction. The emphasis of the present chapter is on the laser-induced desorption of diatomic molecules from metal surfaces, which are the systems that have been most intensively investigated with ns–fs laser pulses. In particular, the interest has concentrated on the catalytically- and theoretically relevant systems of CO, NO or O₂ molecules adsorbed on Cu, Ru, Pd or Pt surfaces. The focus of the following discussion will therefore mainly be on the information obtained from previous all-optical studies of such systems, representing a good starting point for the application of the new technique of fs VUV core-level spectroscopy. In most of the all-optical approaches the desorbed molecules have been detected in a mass spectrometer [34, 35] or by the technique of Resonantly Enhanced Multi-Photon Ionization (REMPI) [36, 37, 38]. In this manner information was obtained about the translational-, vibrational- and rotational distributions of the desorbed molecules and the desorption prob-

ability as a function of wavelength and absorbed fluence. With fs pulses pump-probe experiments have, in addition, become feasible, measuring the desorption yield [39], the reflected probe light [40] or its second harmonic [41] as a function of the pump-probe delay [39]. Before proceeding to a discussion of the results obtained from these measurements it is necessary to consider the mechanisms by which a molecule may be bound to a surface.

5.2.1 The adsorbate-substrate bond

The unperturbed adsorbate-substrate system is usually described by a potential-energy curve (PEC), evaluated as a function of the distance of the adsorbate from the surface and exhibiting a minimum at a certain equilibrium distance. The adsorbate may be weakly bound by a van der Waals attraction in which case it is said to be physisorbed and undergoes only a slight distortion of the electronic structure [42]. This type of bonding is usually encountered for noble-gas adsorbates and/or substrates but is possible for all adsorbate-substrate systems if the temperature is sufficiently low that the adsorbate is unable to surpass the energy barrier to a more stable chemisorption state. The activation energy for desorption is at most a few tens of an eV and adsorption of more than one monolayer is possible. At higher temperatures and/or for more reactive systems, the electronic structure of the adsorbate molecule is significantly distorted and it may dissociate to form new bonds with the substrate. The adsorbate is then said to be chemisorbed and the activation energy for desorption may be significantly increased compared with the physisorbed case. The different types of bonding encountered in this case are shown in figure 5.1, illustrating the possibilities of (a) molecular adsorption, (b) activated and (c) non-activated dissociative adsorption. In the latter case the incoming molecule will most likely dissociate upon adsorption but there exists a (small) possibility that it loses some energy before dissociating and is caught in the molecular well. For a physisorbed molecule the bonding will only take place in the outer, molecular, potential well as dictated by figure 5.1 (a). The ground-state PEC of the adsorbate-substrate complex is the common starting point for the discussion of the different mechanisms by which the molecule may desorb when the system is exposed to laser light. Conventionally, a distinction is made between the processes of direct- and indirect desorption as will be outlined in the following [43].

5.2.2 Direct laser-induced desorption

In the direct desorption process the wavelength of the laser light is resonant with a vibrational transition of the adsorbate or an electronic transition of the adsorbate-substrate complex. In the vibrational case, desorption occurs

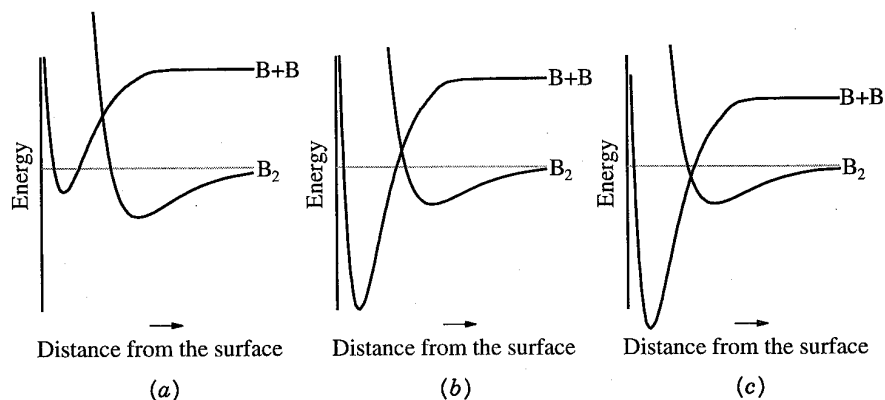


Figure 5.1: Adsorbate-substrate potential-energy curves corresponding to (a) molecular adsorption, (b) activated dissociative adsorption and (c) unactivated dissociative adsorption. From [42].

when enough energy has been transferred from the intra-molecular vibrational mode to the adsorbate-substrate bond by anharmonic couplings. The direct resonant excitation of an adsorbate-substrate vibration is considered a less likely desorption channel, the required ladder-climbing of the vibrational levels being hindered by the anharmonicity of the PEC [28]. In the electronic case, the excited state may be bound, representing, e.g., the binding of an adsorbate positive- or negative ion to its image charge, or it may be repulsive, corresponding to the promotion of an electron from a bonding to an anti-bonding orbital [24]. In either case the excitation is assumed to proceed instantaneously via a Frank-Condon transition, followed by the down-hill motion of the adsorbate towards the equilibrium distance of the excited-state PEC. Eventually the excited state will be quenched and the adsorbate brought back to the ground-state PEC by another Frank-Condon transition, as shown in figure 5.2. If the kinetic energy E'_k gained by the adsorbate from its motion on the excited-state PEC exceeds the binding energy of the ground state evaluated at the same adsorbate-substrate distance, the adsorbate will be released with a positive kinetic energy E_k . An ionic excited state can be quenched by the tunneling of an electron to or from a substrate state, corresponding to a lifetime in the 1–100 fs range. The shortest lifetime is obtained if a substrate state happens to be resonant with the adsorbate state [28]. A neutral excited state can be quenched via charge exchange or electric-field coupling with the substrate, resulting in a lifetime of a few fem-

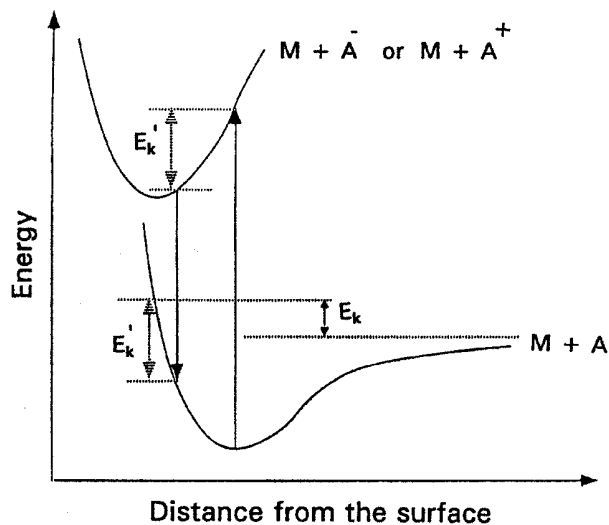


Figure 5.2: A schematic of the mechanism of desorption induced by electronic transitions. M and A denote the surface and adsorbate respectively. The excited-state potential-energy curve may (but need not) be ionic as indicated in the figure. From [24].

toseconds which is comparable to the time-scale required for bond-breaking on a repulsive PEC [28].

The electronic process outlined above is, obviously, called Desorption Induced by Electronic Transitions (DIET) and its description in terms of the excursion to an excited-state PEC is named the MGR-model after Menzel, Gomer and Redhead. It should be noted that the one-dimensionality of the MGR-model not always applies, as illustrated by the example of ammonium where the cross section for NH_3 desorption has been found to be four times larger than that of ND_3 [44]. From the MGR-model applied to the adsorbate-substrate coordinate, the desorption probability would be expected to be largest for the lightest particle which is accelerated faster on the excited-state PEC, becoming more energetic before the quenching occurs. The measured value of the cross section ratio was, however, much larger than predicted from the MGR-model and could only be accounted for by an additional desorption coordinate corresponding to an intra-molecular vibrational motion of the NH_3 molecule. This has become known as the inversion- or umbrella vibration and gives rise to a fascinating desorption mechanism: the three H "legs" of the NH_3 molecule, initially pointing away from the surface, are pushed towards the surface, implying an inversion of the molecular

geometry [45].

5.2.3 Substrate-mediated laser-induced desorption

In the indirect process the desorption is mediated by the laser-excited electron-hole pairs of the substrate which thermalize among themselves and with the substrate lattice on time scales of a sub-picosecond [46] and a few picoseconds [47], respectively. These time scales reflect the electron-electron and electron-phonon scattering times which are on the order of a few tens of femtoseconds [48, 49] and a picosecond [50], respectively. A distinction between an electron- and a lattice temperature can thus only be made with sub-picosecond laser pulses, for which the electron temperature may reach a few thousand Kelvin before approaching an equilibrium temperature with the lattice [38, 41, 47]. The lattice temperature obtained after the first few picoseconds is typically a few hundred Kelvin, not significantly increased above the ambient substrate temperature with which it equilibrates on a time-scale of ~ 100 ps [51].

Thermal- and nanosecond desorption

Substrate-mediated, or indirect, laser-induced desorption occurs as a result of the coupling of the adsorbate with the phonon- or electron heat baths. In a conventional heating process, following the illumination of the surface with quasi-continuous laser light, desorption is induced by the multiple inelastic scatterings of phonons with the adsorbate. By these interactions, energy is transferred to the adsorbate which will climb the vibrational ladder of the ground-state PEC and eventually desorb. The translational-, vibrational- and rotational degrees of freedom of the desorbed molecules can, accordingly, be described by Boltzmann distributions with temperatures that are equal to the temperature of the surface [28]. The desorption yield grows linearly with the absorbed fluence and is independent of the wavelength of the incident radiation.

For desorption induced by ns laser pulses the internal rotational, vibrational and translation degrees of freedom obey a Boltzmann distribution corresponding to a temperature significantly in excess of the substrate temperature [28]. In some experiments, bimodal rotational- and translational distributions, containing an additional low-temperature (thermal) component, have been observed, and in a few cases the distributions could not even be fitted with a two-component Boltzmann function [52]. Depending on the wavelength applied and the internal states studied, rotational-, vibrational- and translational temperatures in the ranges of 100–500 K, 1000–4000 K and 700–2000 K, respectively, have been observed. Most of the studies have been performed with Pt substrates which have been cooled to ~ 100 K to prevent

thermal desorption of the diatomic molecules (CO and NO) [53, 54, 55, 56]. As in the thermal regime, the desorption yield is independent of the wavelength, and the desorption yield and internal state temperatures are linear and constant as a function of the absorbed fluence, respectively [34]. The observations can be accounted for by electronic excitations of the adsorbate-substrate complex to an excited-state PEC, analogously to the DIET mechanism described above for the direct process. The only difference between the two situations is the way in which the energy required for the electronic excitation is provided. In the substrate-mediated process the excitation may be accomplished by the energy released by the recombination of a laser-generated electron-hole pair or by charge transfer of a laser-generated carrier to the adsorbate or the adsorbate-substrate bond. Since the laser wavelength needs not be resonant with an electronic transition in this case, substrate-mediated desorption will be possible also for long (infrared) wavelengths while the direct mechanism may be expected to be dominant for wavelengths in the UV/VUV range [43]. In fact, photon-stimulated desorption using synchrotron radiation in the VUV is an established technique for the chemical identification of adsorbates residing on a surface and their bonding relationships, as reflected by the appearance of desorption peaks at certain, characteristic photon energies [57].

Femtosecond desorption

Recently, experiments performed with fs laser pulses have revealed a dependence of the desorption yield on the wavelength [35], a non-linear dependence of the desorption yield on the absorbed fluence [35, 41, 58] and a fluence dependence of the translational temperature [34, 38]. In addition, for the O₂/Pd(111) [59] and CO/O₂/Pt(111) [60, 61] systems, the branching ratio for desorption relative to dissociation and other chemical reactions has been observed to be significantly increased over that obtained with ns pulses. Apart from the wavelength dependence of the desorption yield these observations can be explained by a generalized DIET mechanism, the so-called DIMET mechanism—Desorption Induced by Multiple Electronic Transitions. As the name indicates, this includes not only one but multiple excitations from the ground- to the excited-state PEC before desorption occurs [62]. In the fs regime multiple excitations are much more likely due to the much higher density of hot electrons and lead to an enhanced desorption probability due the enhanced accumulated time available for the adsorbate-substrate complex on the excited-state PEC. In the DIMET model the desorption probability is calculated from the transition rates between the PEC's which, in turn, are obtained from a knowledge of the energy distribution of the laser-generated electrons which is usually taken to be the Fermi-Dirac function [62]. By this

approach it is implicitly assumed that the electrons can be designated a temperature which may not be justified within the first ps after the presence of the desorbing laser pulse [46]. Since the electron temperature depends on the pulse duration and the absorbed fluence but not the wavelength, the wavelength dependence of the desorption yield observed by the group of Mazur has been attributed to the influence of non-thermalized substrate electrons [35].

Attempts have been made to deduce some of the time scales involved in the electron-mediated desorption process by means of pump-probe measurements. Most of these have applied a two-pulse correlation scheme where the desorption yield is monitored as a function of pump-probe delay [39, 47, 51, 63, 64]. These measurements have revealed a peak with a ~ 1 ps width (FWHM) on top of a broad plateau with a decay time of ~ 100 ps. The ~ 100 ps decay time has been attributed to equilibration of the laser-heated region with the ambient substrate [51] but the assignment of the ~ 1 ps spike is less clear. Bonn *et al.* have performed two-pulse correlation measurements for CO and CO₂, generated from the oxidation of CO, on Ru(0001) yielding correlation times of 20 ps and 3 ps, respectively [47]. These were taken as evidence for phonon- and electron-mediated processes, respectively, with reference to the much longer cooling time of the lattice compared with the electron gas. The short-lived component was attributed to the electron-mediated mechanism on account of a comparison with the sub-picosecond electron-phonon coupling time which determines the cooling time of the hot-electron gas [39, 47]. This was supported by the fact that the energy barrier to CO desorption is significantly lower than that for CO₂ formation, the latter being given by the activation energy for breaking of the Ru–O bond of the dissociatively adsorbed O atoms [47].

It remains unclear what the correlation time really means [35], i.e. with which physical process it should be identified. An upper limit to the actual desorption time, i.e. the time required for the breakage of the adsorbate-substrate bond, has been set to 325 fs from a measurement of the change in second-harmonic signal of the probe as a function of pump-probe delay by Prybyla *et al.* [41]. The second-harmonic signal depends on the degree of adsorbate coverage and thus allows a more unambiguous interpretation of the observed time scale. An even more direct interpretation will be allowed by the technique of fs VUV core-level spectroscopy where the size of a substrate core-level shift depends on its chemical surroundings, in this case the degree of adsorbate coverage.

5.3 The technique of core-level spectroscopy

The most common techniques in use today for structural analysis of surfaces at the atomic level are Low-Energy Electron Diffraction (LEED) [65], Surface-Extended X-ray Absorption Fine Structure (SEXAFS) [66], X-ray Photo-Electron Diffraction (PED) [67], X-ray Core-Level Spectroscopy (CLS) [68, 69, 70, 71] and Scanning-Tunneling Microscopy (STM) [72]. Apart from STM, the surface sensitivity of these techniques is accomplished by the short ($<10 \text{ \AA}$) inelastic mean-free path experienced by electrons with kinetic energies in the 20–250 eV range [73]. The inelastic mean-free path is the same for all the elements and thus constitutes a universal curve when evaluated as a function of the kinetic energy. Accordingly, electrons with energies in this interval are used in LEED and are aimed at in the other X-ray-based techniques. This is accomplished by choosing the photon energies in a range corresponding to the most appropriate kinetic-energy interval of the detected photoelectrons.

Attempts have been made to push the time resolution of LEED [74] and STM [75] towards the femtosecond regime but this is not feasible due to the Coulomb scattering among the electrons (cf. chapter 1) and the scanning principle of the STM, respectively. More promising for this purpose are the X-ray-based techniques where the time-resolution is given by the X-ray pulse duration. Among the X-ray-based techniques quantitative information about atomic- and molecular bond lengths can only be obtained with PED and SEXAFS where the photoelectron yield is measured as a function of photon energy over an extended photon-energy range, typically a few hundred eV. The bond length is extracted from the period of the oscillations appearing in these scans due to the interference of the outgoing photoelectron wavepackets with their reflections from neighboring atoms. In principle, the same information can be extracted from a scan of the photoelectron emission angle for a fixed photon energy but this gives rise to more complex oscillations and a more complicated data analysis. Because of the large photon-energy scans required in SEXAFS and PED, these techniques are feasible at a synchrotron-radiation beamline but certainly not with a VUV light source based on high-order harmonics, limited in photon energy to $\sim 100 \text{ eV}$ (cf. chapter 1).

For the present purpose it was decided to insist on the claim of a fs time-resolution and an optimum surface sensitivity and then relax the requirements to the quantity of structural information obtainable. As a consequence, the most obvious choice of technique is CLS, which is recognized as a valuable, complementary tool, allowing for a discrimination between different adsorption sites and providing information about the mutual arrangements of the adsorbates with respect to each other and the substrate [76, 77, 78]. In CLS

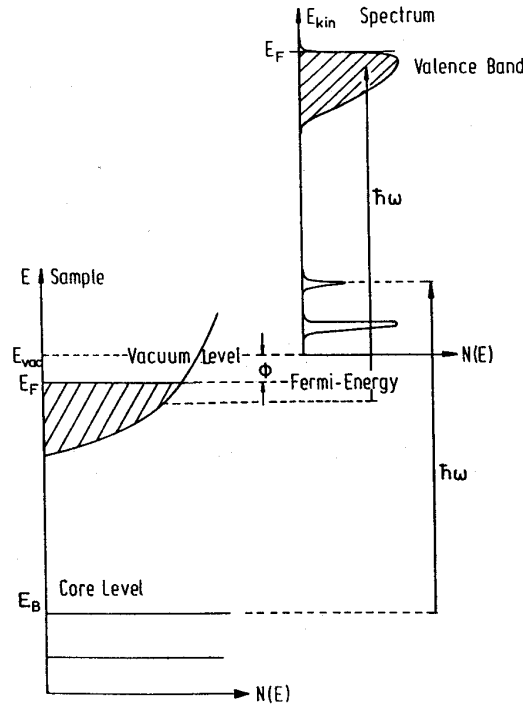


Figure 5.3: A schematic of the relation between the energy-level diagram of the solid and the kinetic-energy spectrum of the photoelectrons emitted in core-level spectroscopy, using a VUV light source with photon energy $\hbar\omega$. The work function of the solid and the electronic density of states evaluated as a function of electronic energy E are denoted by ϕ and $N(E)$, respectively. From [70].

the surface is illuminated with a VUV- or X-ray beam of fixed photon energy and a kinetic-energy spectrum of the emitted photoelectrons is recorded. The kinetic energies of the photoelectrons are given (with reference to the vacuum level) by $E_{\text{kin}} = \hbar\omega - E_B - \phi$ where $\hbar\omega$ is the photon energy, E_B the binding energy of the electron with respect to the Fermi level and ϕ the work function of the surface. Ideally, this results in a translation of the energy spectrum of the adsorbate-substrate complex into the continuum, as shown in figure 5.3 [70]. If $\hbar\omega$ is sufficiently large this spectrum will include some of the core-levels of the elements present at the surface, thus facilitating a sensitive chemical analysis of the surface. Furthermore, the core-level binding energy of the adsorbate- or substrate atom will be affected by its chemical surroundings, signified by a meV–eV "chemical shift". The shift

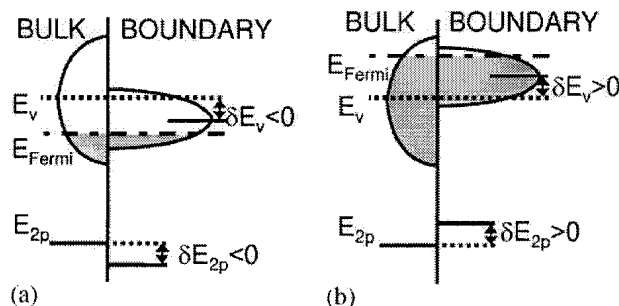


Figure 5.4: A schematic of the valence-band narrowing at the bulk-surface boundary, which implies (a) an increase in the core-level binding energy for a less than half-filled valence band and (b) a decrease in the core-level binding energy for a more than half-filled valence band. From [81].

arises from the redistribution of the electronic charge in the valence orbitals due to the chemical bonding. By the many-body nature of the surface, the calculations of these shifts represent a challenge to theorists which resort to density-functional theory [79] or the (MC)SCF methods [80] (cf. chapter 2). Often, use is made of the equivalent cores approximation by which the final-state energy of a Z -electron atom with a core-hole is replaced by the more easily calculated ground-state energy of a $Z + 1$ -electron atom [71, 80]. Correctly, the core-level binding energy is given by the energy difference between the total initial- and final-state energies, i.e. the electronic energies before and after the ionization. Most difficult is the final-state calculation where relaxation effects must be taken into account, arising from the rearrangements of the outer electrons to screen the core-hole.

By a simple electrostatic consideration, the core-level binding energy can be expected to be higher for an atom sitting in an electro-negative environment: the removal of an electronic charge δe from the valence shell with radius r causes the binding energy of an inner electron with elementary charge e to increase by the amount $e\delta e/r$ [82]. For an atom bound in the surface layer there will be a spill-out of valence charge into the vacuum (or air), i.e. the vacuum acts as an electro-negative environment, and an increase in core-level binding energy should be expected. For a metal, the narrowing of the valence band at the surface with respect to that of the bulk will give rise to an additional contribution as shown in figure 5.4. Since the electronic charge must be (approximately) conserved across the bulk-surface region, the surface valence band must adjust to align its Fermi energy with that of the bulk, resulting in down- and up-ward shifts for less- and more than half-filled valence bands, respectively [81]. This shift will be partly followed by the core-levels, im-

plying an increase in the core-level binding energy for a metal with a less than half filled valence-band and vice versa. For the transition metals with a partly filled d -shell the valence-band narrowing is dominating while for the simple sp metals the two contributions are almost equal, resulting in a small (~ 100 meV) shift towards lower binding energy for Al(100) and no shift for Al(111) [83].

The natural width of a core-level depends on the probability that the core-hole will be filled by an electron decaying from an outer (valence) shell. This probability is, in general, larger the larger the number of electrons occupying the outer shells but this picture may be modified by correlation effects and particularly strong decay channels [84]. Typically, the core-level widths vary in the 0.1–2 eV range between different elements with comparable core-level binding energies [85]. For example, the Al $2p$ level with a core-level binding energy of ~ 73 eV has an unusually narrow width of ~ 50 meV, as reflected by the presence of only three electrons in higher-lying shells. At the other extreme, the widths of the $3p$ and $4p$ levels of the first- and second-row transition elements, spanning a 30–90 eV binding-energy range, are 2–4 eV, with the lowest value attained at the left of the periodic table [85, 86]. The natural Lorentzian width is often masked by Gaussian contributions from phonon broadening and the experimental resolution of the electron-energy analyzer (each contributing at least ~ 50 meV) [87]. In addition, there will be a tail on the low-kinetic energy side of the core-level peak arising from intrinsic- and extrinsic excitation processes taking place during- and after the photoionization process, respectively. The most important intrinsic losses are due to electron-hole pair excitations which give rise to an asymmetry of the core-level peak. The extrinsic losses arise from inelastic scatterings of the photoelectrons travelling towards the surface and their contribution will be minimum when the escape depth is smallest possible, i.e. for a ~ 50 eV kinetic energy of the core-ionized electrons (which contribute the most to the spectrum). Considering all these contributions, a measured core-level peak is most often fitted with the so-called Doniach-Sunjić line-shape [88]

$$D(E) = \frac{\Gamma(1 - \alpha) \cos[\pi\alpha/2 + (1 - \alpha) \arctan(-\frac{E - E_B}{\gamma})]}{(1 + \frac{(E - E_B)^2}{\gamma^2})^{(1 - \alpha)/2}} \quad (5.1)$$

convolved with a Gaussian representing the combined effects of the phonon broadening and experimental resolution, and added to a polynomial background representing the intrinsic- and extrinsic losses. Here, E_B is the core-level binding energy, γ the natural width (HWHM), α an asymmetry parameter accounting for electron-hole pair excitations and Γ the Gamma function.

5.4 Core-level spectroscopic tests at ASTRID

5.4.1 Experimental setup

The core-level spectroscopic tests of the CO/Pt and O/Al systems were performed at the SGM I synchrotron-radiation beamline at ASTRID. SGM refers to the Spherical Grating Monochromator of the beamline which can be operated in the 25–300 eV photon-energy range, using three sets of spherical gratings and plane mirrors [89]. For the present experiments the monochromator was operated with entrance/exit-slit settings of 50/50 μm and 100/100 μm , corresponding to 30 meV and 50 meV resolutions (FWHM), respectively, for a ~ 100 eV photon energy. A target chamber is installed at the end of the beamline and the sample can be moved to a pre-chamber with standard equipment for surface preparation and -characterization. This includes an ion sputter gun, a quadrupole mass spectrometer (QMS) and LEED apparatus. The horizontally polarized synchrotron-radiation beam is incident on the surface at 40° with respect to the surface normal and photoelectrons emitted within a ~ 0.1 steradian space angle normal to the surface are collected with a SCIENTA electron spectrometer [90], as shown in figure 5.5. The electrons are focused onto the entrance slit of the spectrometer by a lens system and are dispersed according to their kinetic energy by the radial electrostatic field between the hemispheres. The lens system in addition retards the electrons to a pre-determined pass energy, E_{pass} , which is proportional to the voltage difference between the two concentric spheres. Due to the spherical symmetry of the spectrometer, the entrance slit is imaged onto the detector system, consisting of a Microchannel-Plate Detector (MCP) and a Charged-Coupled Device (CCD) camera. There is thus no need for an exit slit and energies within a window of size $E_{\text{pass}}/10$ can be simultaneously detected. The energy resolution ΔE_{spec} (FWHM) of the spectrometer is given by the width Δr of the entrance slit and the pass energy as $\Delta E_{\text{spec}} = \Delta r / (E_{\text{pass}} 2r)$ where $r = 20$ cm is the mean radius of the hemispheres. The ultimate energy resolution that can be achieved is ~ 5 meV but for the present purpose the spectrometer was operated with a resolution in the 40–150 meV range.

The base pressure of the target chamber is $\sim 1 \times 10^{-10}$ Torr and has to be at least that good if the surface is to be kept clean during a few hours of measurement. Gas doses are usually given in Langmuir, with $1 \text{ L} = 1 \times 10^{-6}$ Torr·s, which is approximately the amount required for a monolayer coverage of rest gas (N_2), assuming a sticking probability of unity. This means that if every (rest) gas molecule hitting the surface stays there, a monolayer coverage is obtained in one second at a pressure of 1×10^{-6} Torr! A surface therefore has to be cleaned every day before use, which was done by Ar^+ sputtering followed by annealing to elevated temperatures. By the

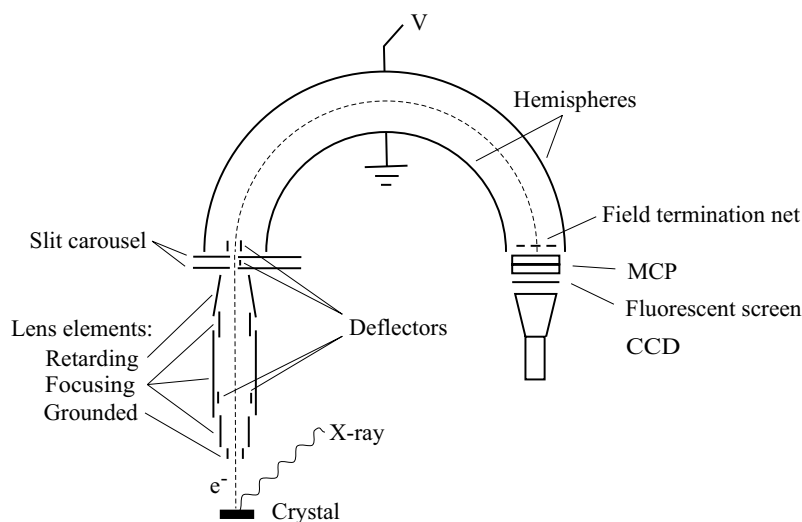


Figure 5.5: A schematic of the SCIENTA photoelectron spectrometer at the SGM I beamline at ASTRID. From [87].

sputter process, the upper surface layers are removed by bombardment with ~ 1 kV Ar^+ ions at a $\sim 1 \times 10^{-6}$ Torr pressure, thereby generating craters and implanting Ar^+ ions into the surface [91]. The craters are expected to be of $\sim \text{nm}$ dimensions for the relatively low sputter energy applied here and may develop into regular patterns, especially for sputtering at an angle near normal incidence [92]. These features are removed by the annealing process which, in turn, may induce diffusion and segregation of bulk contaminants to the surface [93, 94]. As a consequence, several sputter-annealing cycles are required to clean a newly installed, mechanically polished crystal, and the total amount of cleaning required depends on the nature and the prehistory of the crystal. For a newly installed Al crystal, for example, a relatively large effort must be invested initially in order to penetrate a 3–4 nm protective oxide layer [95]. Recently, it has been demonstrated that an extremely long sputtering time is required to produce an Al surface that exhibits a reproducible O_2 adsorption behaviour, as will be discussed in section 5.4.3.

In the present experiments a sputter-annealing cycle typically consisted of 45 min sputtering with 1 kV Ar^+ ions at 1×10^{-6} Torr Ar pressure followed by 15 min annealing to $\sim 600^\circ \text{C}$ and $\sim 450^\circ \text{C}$ for Pt and Al, respectively. The Ar^+ ion beam is incident on the surface at a 45° angle with respect to the surface normal. The annealing temperature was chosen with the melting

temperatures of the surfaces in mind and should be high enough that the craters induced by the sputtering process are smoothed out and low enough that disordering and defect formation at the surface are avoided. The Pt surface was annealed in a 2×10^{-8} Torr oxygen atmosphere (which has been proposed as a method for the removal of carbon impurities [96]), followed by a couple of minutes heating to $\sim 900^\circ$ C. The cleanness was checked by looking for core-level peaks from expected contaminants and by checking whether the core-levels to be measured for the clean surface exhibited signatures of contamination (shoulders or additional peaks).

The Pt and Al crystals were mounted on Ta and Si sample holders, respectively, and were resistively heated through a couple of wires attached to these holders. The temperature was measured with an n-type thermo-couple attached to the rear side of the sample holder and could be kept at the desired value to within a few degrees by a feedback mechanism. There was, however, problems with several degrees overshoot during initial temperature ramping, especially, for the Si mount where the resistivity undergoes a sudden decrease at a certain "breakthrough" temperature, corresponding to electron-hole pair excitations across the band-gap. The crystals could be cooled down to $\sim -110^\circ$ C by thermal contact with a liquid N₂ reservoir through a flexible copper braid fastened to the rear side of the sample holder. The core-level spectra were recorded at this temperature in order to minimize the phonon broadening, and CO was dosed at this temperature while O₂ was dosed at room temperature. Both CO and O₂ bind to Pt and Al, respectively, at room temperature, but the CO/Pt(111) system has been most intensively studied in the low-temperature regime.

5.4.2 CO/Pt(111)

As outlined in section 5.3, the magnitude of the extrinsic background level of a core-level spectrum exhibits a minimum if core-level electrons are photoionized with kinetic energies around ~ 50 eV. This ideal condition is difficult to fulfil with the ~ 100 eV photon energy aimed at for the fs studies. More precisely, a 96.4 eV photon energy has been chosen (the 63rd harmonic of the 810 nm Ti:sapphire fs laser), considering the ~ 99 eV absorption edge of the Si/Mo multilayer mirror intended for the setup. Since the inelastic mean-free path is still relatively short (< 10 Å) for kinetic energies ≥ 20 eV, it was decided to focus on systems among the transition-metal group with core-levels in the 50–75 eV range as possible candidates for the first studies of fs laser-induced desorption using the 63rd harmonic. These include the very broad $3p$ and $4p$ levels of the first- and second-row transition metals and the narrower $4f$ levels of the third row [97]. Since the resolution of the

fs setup is expected to be limited to 0.1–0.5 eV by the bandwidth of the VUV light source, the core-levels must be relatively narrow and well-defined, favouring the third-row metals. Among these elements only Pt has been the subject of fs desorption studies and in addition, the influence of CO on the $4f$ core-levels is known from previous studies with 125 eV photons [98, 99]. The CO/Pt(111) system was, accordingly, given first priority for a test measurement with ~ 96 eV photons at the SGM I beamline. The purpose was to get an idea of the appearance of the $4f$ core-level spectrum under conditions similar to those expected for the fs setup and, in case of a favourable background level, to provide reference core-level spectra for different adsorbate coverages.

CO binds non-dissociatively to the close-packed Pt(111) surface below $\sim 190^\circ\text{C}$ [100] with an activation energy towards desorption of 1.4 eV [101]. The molecule is oriented with the intra-molecular axis perpendicular to the surface, i.e. upright, and with the C atom closest to the surface [102]. The binding is accomplished by the CO molecule donating a fraction of its electronic charge from its highest occupied orbital, 5σ , to the Pt surface which, in turn, donates a fraction of a charge to the lowest un-occupied CO orbital, 2π [103]. This bonding mechanism is common for CO adsorption on all of the transition metals and leads to a weakening of the C–O bond, which for Ni and Fe is sufficiently strong that the molecule may dissociate [104]. CO molecules adsorbed on Pt(111) at ~ 100 K form different ordered structures, or phases, depending on the coverage, which saturates at 0.5 monolayer. A monolayer (ML) is defined as the coverage giving an adsorbate surface density which is equal to that of the substrate. For chemisorption systems where multi-layer adsorption does not appear, the adsorbate coverage saturates at a value ≤ 1 ML, depending on the physical size of the adsorbates with respect to the substrate atoms. Below 0.25 ML the CO molecules preferentially occupy on-top sites in a (4×4) structure but for higher coverages the energetically less favourable bridge-sites must be occupied as well, leading to a (4×2) structure with equally occupied on-top- and bridge sites at the 0.5 ML saturation coverage (in the language of surface science a $(m\times n)$ $R\Theta$ structure means the unit cell of the adsorbate structure being enlarged by a factor $m\times n$ and rotated by an angle Θ with respect to that of the substrate) [99, 105].

The $4f$ core-level spectrum of clean Pt consists of the two spin-orbit components $4f_{5/2}$ and $4f_{7/2}$ with binding energies of 74.5 and 71.2 eV, respectively [97]. Core-level spectra of the $4f_{7/2}$ level have been recorded with 125 eV photons by Björneholm *et al.* for different CO coverages [99] and for the clean Pt(111) surface a surface core-level shift of 0.4 eV towards lower binding energy was observed. Upon CO adsorption the surface peak diminished simultaneously with the appearance of two new peaks at higher binding

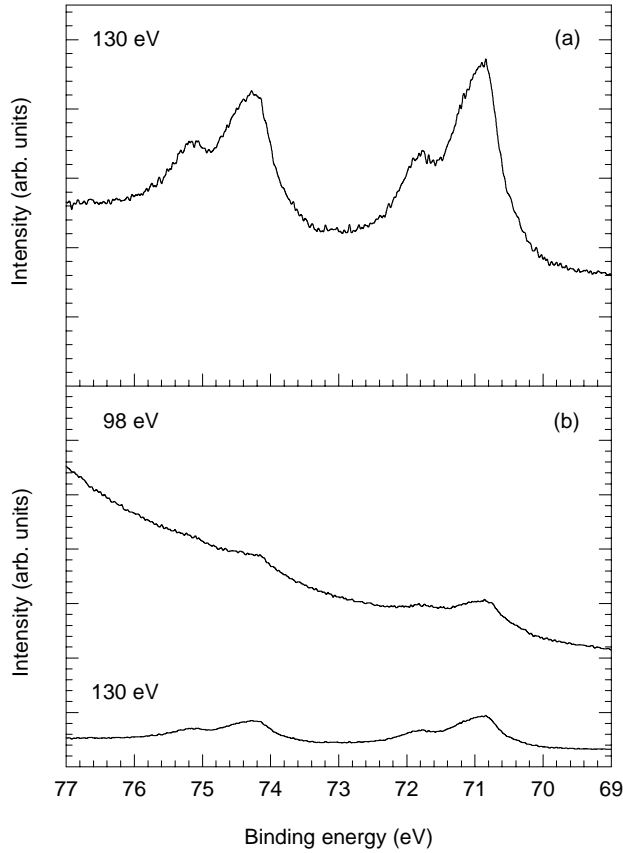


Figure 5.6: Pt 4*f* core-level spectra for the CO/Pt(111) system at saturation coverage (0.5 ML CO) measured with a photon energy of (a) 130 eV and (b) 98 eV. The spectrum of (a) is reproduced in (b) for comparison.

energies, displaced by 1.0 and 0.3 eV with respect to the $4f_{7/2}$ bulk peak. These peaks were attributed to on-top- and bridge binding, respectively, on account of the evolution of their size as a function of CO coverage. The on-top peak was clearly resolved with the 0.15 eV experimental resolution while the bridge peak was revealed as a broadening of the bulk peak.

4*f* core-level spectra for the CO/Pt(111) system were recorded at ASTRID with 130 and 98 eV photon energies and a total experimental resolution of 0.16 eV, as shown in figures 5.6 (a) and (b), respectively. The spectra were recorded at -110°C right after exposure of the Pt(111) surface to a 0.5 ML

saturation coverage of CO. With a sticking probability of 0.8 [106] the 0.5 ML saturation coverage is obtained after only a few seconds of CO dosing at 2×10^{-7} Torr but to be on the safe side the dosing was continued for a few minutes. An eventual offset in the monochromator calibration has not been corrected for, as this was of no relevance in the present context. The $4f_{5/2}$ and $4f_{7/2}$ peaks and the CO on-top features towards higher binding energy are clearly visible in the 130 eV spectrum but unfortunately almost buried in the (extrinsic) secondary-electron background at 98 eV. The 130 eV spectrum is shown for comparison in figure 5.6 (b) also, and the background levels are seen to differ by at least a factor of ~ 7 despite a difference in the inelastic mean-free path of at most a factor of 2 (cf. the universal curve). On account of the very large background level the use of Pt for the fs desorption studies can be excluded.

5.4.3 Oxidation of Al(111)

Following the negative experience with Pt, attention was drawn to Al which has some very well-defined $2p_{1/2}$ and $2p_{3/2}$ core levels at 73.1 and 72.9 eV that have been the subject of numerous studies at Aarhus University [87]. These studies have, however, mainly concentrated on the theoretically relevant alkali/Al systems which tend to form surface alloys and thus are inappropriate for laser-desorption studies [77]. On the other hand, the oxidation process of Al is not yet fully understood in spite of the very large attention that has been given to this technologically important system. Previous core-level spectroscopic measurements of oxygen adsorption on Al have shown pronounced effects of the oxygen adsorption on the appearance of the Al $2p$ peaks [107, 108]. This would make the system a good candidate for an experiment with a modest energy resolution. In addition, a photo-desorption experiment using synchrotron radiation has demonstrated that the dissociatively adsorbed oxygen atoms can be ejected as O^- ions, following the absorption of 8.7 eV photons [109]. This was ascribed to a direct electronic process on account of the 8.7 eV photon energy being in exact resonance with the transition from the ground-state to a repulsive excited-state potential-energy curve of AlO^- . No studies have been made with visible ns- or fs laser light but it may be possible to desorb the O atoms by an electron-mediated process despite an activation energy towards desorption of ~ 5 eV [110], at least by using 4-5 eV photons. For comparison, in the oxidation reaction of CO on Ru(0001) studied by Bonn *et al.* (cf. section 5.2.3) the bond breakage of the dissociatively adsorbed oxygen atoms with a 1.8 eV activation energy could be activated with 1.5 eV fs laser pulses by the electron-mediated mechanism. Following these considerations the O/Al(111) was given priority to a further

investigation at the SGM I beamline.

The Al single-crystal surface, in particular the close-packed Al(111), has been the subject of numerous experimental and theoretical investigations as reviewed up to 1984 by Batra and Kleinman [111]. The O₂ molecule is known to adsorb dissociatively on the Al surface to form a chemisorbed O/Al phase that is converted into a very stable 3–4 nm thick amorphous Al₂O₃ layer, following an increase in the temperature or oxygen coverage. The electrically insulating oxide layer protects the metal against corrosion [95] and makes Al the most widely used metal in semiconductor devices [112] and magnetic tunneling junctions [113]. Recently, the growth of an oxide layer was suggested as a method for the production of reliable single-electron transistors, providing an effective means of confining the electron in an Al quantum dot [112]. Al₂O₃ is also the most commonly used support material for the production of 1–10 nm catalyst metal particles, which are deposited in carefully prepared micropores of the oxide [1, 114]. In spite of this, the structures of the different crystallographic phases that can be attained by Al₂O₃ have still not been mapped out [115] and even the initial oxidation behaviour, the dissociative chemisorption of O₂ on Al remains a matter of debate [116, 117, 118, 119, 120].

There is general agreement that for the O/Al(111) system adsorption at room temperature initially leads to an O adlayer of randomly distributed, immobile O atoms, developing into (1×1) O islands as the coverage increases [121]. This chemisorbed phase coexists with the oxide phase which starts to develop at a 0.2 ML coverage, long before the surface is fully covered by the O islands. Around this coverage the island density saturates and further oxygen uptake leads to a growth in the island size. The oxide layer preferentially develops at the interface between the O islands and the bare Al surface, initially in the form of small (~2 nm diameter) grains as observed in STM images by Trost *et al.* [116]. The grain formation continues until the surface is completely covered with an amorphous oxide layer, growing in thickness with increasing O₂ exposure. In the chemisorbed phase the O atoms have been observed to occupy three-fold hollow sites above the Al(111) surface. No sub-surface oxygen, as required for the oxide formation process, was found below a 1 ML coverage [122, 123]. This is in agreement with recent calculations, pointing towards the on-surface site as energetically preferable below a 1 ML coverage, with a sub-surface tetrahedral site becoming equally favourable as the coverage is increased beyond this value [119].

The above observations are supported by measured core-level spectra which have shown the existence of three so-called sub-oxide peaks and one oxide peak adjacent to the 2*p* peaks on the high binding-energy side [124, 107, 108]. The three sub-oxide peaks were found to be shifted by 0.49, 0.97

and 1.46 eV with respect to the $2p_{3/2}$ level at 72.7 eV while the broad oxide peak was shifted by 2.5–2.7 eV (see also figure 5.7) [124]. The three sub-oxide peaks were observed to show up one after the other, following an increase in oxygen coverage, with the 0.49 eV peak appearing first. The latter was hidden by the $2p_{1/2}$ peak at 73.1 eV while the other peaks were clearly visible. The three sub-oxide peaks have been associated with Al atoms binding to one-, two- and three O atoms, respectively, as can be rationalized from the simple electrostatic picture of section 5.3, given the fact that the oxygen atoms represent an electro-negative environment. This corresponds to Al atoms situated at the edges and in the interior of an O island where the coordination numbers to O atoms are one (or two) and three, respectively [121]. In a single high-resolution (50 meV) study, an additional shoulder on the low binding-energy side of the Al $2p$ peaks was observed and ascribed to atoms sitting in a metallic environment, most likely in a (mono-atomic) semi-amorphous Al layer situated at the Al-Al₂O₃ interface [107]. A similar shoulder was recently resolved for the O/Al(100) system and given a similar assignment [87]. In that experiment the oxidation behaviour of Al(100) was observed to be similar to that of Al(111) apart from the three sub-oxide peaks appearing simultaneously. The above core-level measurements have been performed with photon energies in the 100–110 eV range, so the O/Al(111) system was considered a relatively safe candidate for a 96 eV measurement.

The controversy regards the mechanism of initial sticking of the O₂ molecules to the surface [120] and the observation that the rates of chemisorption (i.e. the sticking probability) and oxide formation vary considerably among different experiments [117]. The oxygen sticking probability of ~ 0.005 is abnormally low considering the ~ 5 eV chemisorption energy, and its eventual relation to an observed non-thermal behaviour of the dissociating O atoms remains unclear [120, 125]. The sticking probability has been observed to be independent of temperature by Österlund *et al.* [126] while an increase was found by the group of Yates [117, 127, 125]. Both groups agree on an activated dissociative adsorption process in the 243–600 K regime which, on account of the temperature dependence of the sticking probability, was ascribed by Yates *et al.* to the presence of an O₂ precursor state prior to dissociation [125, 127]. So far further support for a molecular precursor state has not been given experimentally [124] or theoretically [118, 128] but in the latter case this might be attributed to the approximation applied.

The experiments of Yates *et al.* were performed with an Al(111) surface that had been subjected to an extreme amount of sputtering (≥ 45 hours) and annealing which was found to be necessary in order to obtain a reproducible adsorption behaviour. With this intensive pre-treatment the sticking probability was observed to be lower than that of an "ordinarily" cleaned surface

and the conversion from the metastable chemisorbed phase to the oxide phase occurred at a higher temperature compared with previous reports [117]. This was attributed to a reduction in the concentration of defect sites with respect to that of an ordinarily cleaned surface [127]. These defects may arise from, e.g., the crude mechanical polishing of the surface prior to application, in which case several atomic layers must be peeled off by the sputter process in order to reach a depth with a lower defect concentration. Remarkably, however, at least 10 hours of sputtering was necessary after each measurement performed with only a sub-monolayer oxygen coverage for reproducible measurements to be obtained. The most obvious explanation for this would be a diffusion of oxygen atoms into the bulk but no further comments were made about this issue. One could, in principle, imagine defects to be introduced by the rather crude sputter treatment but this was apparently not the case, maybe because of the correspondingly prolonged (to 45–60 minutes) annealing treatments performed with 5–10 hours intervals [129]. The annealing process has, however, by STM measurements been observed to induce defects when performed at temperatures above $\sim 450^\circ\text{C}$ [129]. The question about the possible influence of defects on the oxidation behaviour has previously been addressed by Larson and Lauderback for the Al(100) surface and they did, in fact, provide evidence for an enhanced chemisorption and oxide formation probability for Al surfaces with a higher defect concentration [130]. The nature of the defects could not be established but the defect density could be varied by changing the mechanical polishing procedure, and for the most defect-ful surfaces a penetration depth on the order of a μm was estimated. This was rationalized on account of the persistence of defects even after several sputter-anneal cycles. The recognition that even a low concentration of surface defects or -imperfections may have a large influence on the adsorption- and desorption behaviour of a surface is not new [131] but the need for an extremely long (≥ 45 hours) sputtering time for reliable results to be obtained has not been previously reported. This could be attributed to a particularly large sensitivity of the Al oxidation behaviour to the presence of defects or, more likely, the softness of the clean Al metal, making it more vulnerable to mechanical polishing.

The purpose of the core-level measurements on O/Al(111) at the SGM I beamline was partly to check whether the secondary-electron background was still well-behaved at a ~ 96 eV photon energy, partly to investigate the effect of the surface pre-treatment on the appearance of the Al $2p$ core-level spectra. The newly installed Al(111) crystal was initially degassed for 48 hours at 400°C , and then six times repeatedly Ar^+ sputtered for half an hour at 1–1.5 kV and annealed at 400°C for 10 minutes. This was followed by a total of 9 hours sputtering during which the crystal was kept at 440°C

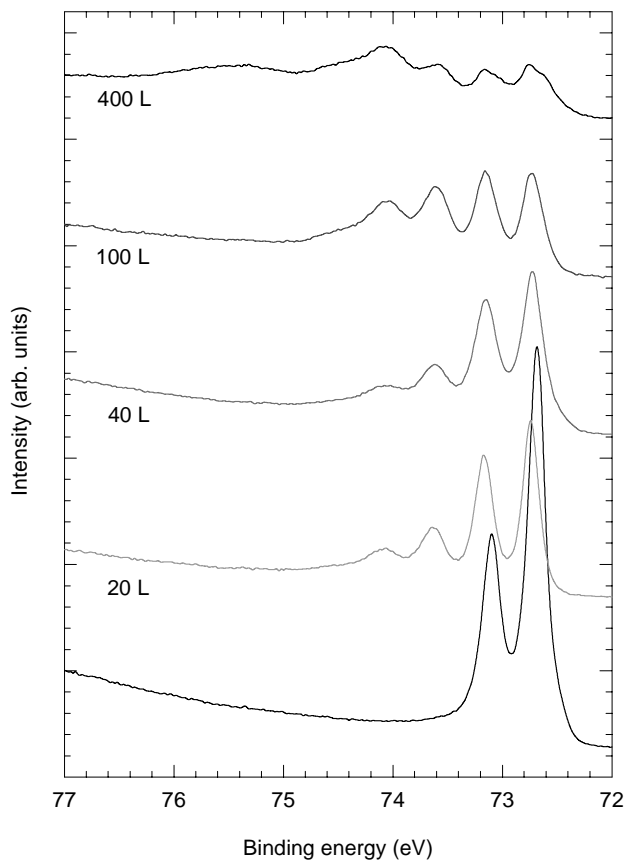


Figure 5.7: Al $2p$ core-level spectra for different oxygen coverages measured with a photon energy of 95 eV.

in order to drive out carbon impurities from the bulk. The surface then appeared chemically clean and a series of measurements was performed after another two times 1/2 hour sputtering and 10 minutes annealing to 440°C , i.e. after a total of 13 hours of sputtering. Al $2p$ spectra were recorded with a 95 eV photon energy for the clean Al surface and for the Al surface exposed to oxygen doses in the 20–400 L range, as shown in figure 5.7. This corresponds to coverages in the 0.1–2 ML range, assuming a sticking probability of 0.005 [127]. All of the Al spectra were recorded with a 50 meV resolution at -110°C with the oxygen being dosed at room temperature. The binding-energy axis has been translated by ~ 1 eV to have the $2p$ peak positions

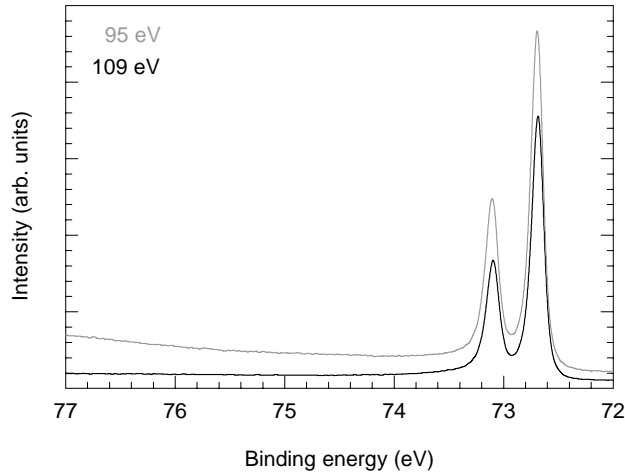


Figure 5.8: A comparison of Al 2*p* spectra measured with 95 and 109 eV photon energies.

of the clean Al surface appear at their "nominal" energies, compensating a ~ 1 eV offset in the monochromator calibration. The surface was sputtered and annealed for $\sim 1/2$ hour after each measurement in order to remove the old oxygen layer before a new was dosed. As evident from figure 5.7 the Al $2p_{1/2}$ and $2p_{3/2}$ peaks as well as the oxygen-induced peaks are clearly visible with the 95 eV photon energy and the O/Al(111) system can, as expected, be considered a suitable candidate for future fs VUV core-level spectroscopic studies. The broad oxide peak at ~ 75.5 eV binding energy is, however, somewhat buried in the secondary-electron background which is somewhat large compared with that of the previous measurements performed by other groups [107, 108]. In addition, the Al $2p$ peaks are significantly suppressed and broadened in comparison with the previous spectra [107, 108]. The broadening could be caused by randomly distributed defects which would give rise to randomly distributed core-level shifts, recognized as an apparent broadening of the $2p$ peaks.

After this measurement series it was decided to perform a ~ 50 hours sputtering, while keeping the crystal at room temperature, in order to mimic the surface pre-treatment of the Yates group. Unfortunately the sputter gun broke down somewhere between 34 and 52 hours of sputtering and could not be immediately repaired (the crystal had then been under a 1×10^{-6} Torr Ar pressure for 52 hours). Immediately after turn off of the Ar gas inlet the crystal was annealed at $\sim 450^\circ$ C for 15 minutes and core-level spectra were recorded at 95 and 109 eV photon energies, respectively, as shown in figure

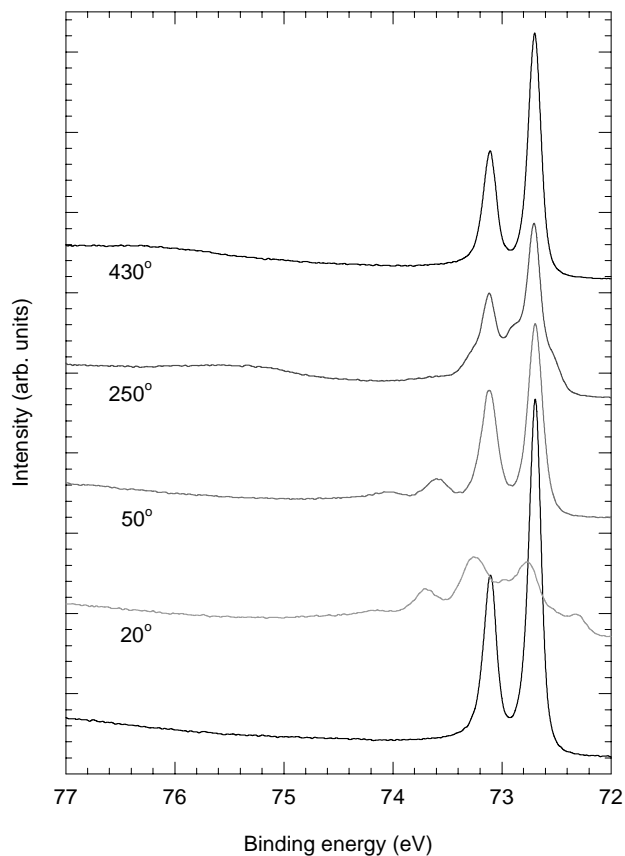


Figure 5.9: From below: Al $2p$ core-level spectra at 95 eV of the clean Al(111) surface following a long-term sputtering, the surface after 20 L oxygen exposure at room temperature (20°) and the surface after ~ 10 minutes heating to 50° , 250° and 430° .

5.8. The background level is seen to be considerably lower than that of figure 5.7 and the Al $2p$ peaks are no longer broadened. The 95 eV spectrum is depicted in figure 5.9 together with spectra measured after 20 L of O_2 dosing. The 20° spectrum was recorded (at -110°C) immediately after O_2 dosing while the following spectra were measured (at -110°C) after the surface had been heated to the indicated temperature for ~ 10 minutes. The 20° spectrum does not look like anything which has previously been observed at 20 L coverage, but the well-known characteristics of the chemisorbed phase (cf. figure 5.7) are recovered in the 50° spectrum. The 250° spectrum again

looks very different from what has previously been observed while the 430° spectrum exhibits the characteristic behaviour of an oxide-covered Al surface.

The 20° spectrum looks so peculiar that one might think that something has gone wrong during the measurement, for example that the sample has not been properly grounded. This issue was checked at a subsequent beamtime where a long-term sputtering of a new crystal was attempted. Unfortunately, the sputter gun was not sufficiently stable that the long-term pre-treatment could be done but the grounding issue was checked and the spectra found to be identical, independent of the apparent grounding conditions. The interesting features of the 20° C spectrum are the significant suppression of all of the peaks despite the very low coverage and the appearance of a peak at the low binding-energy side, shifted by ~ 0.5 eV with respect to the $2p_{3/2}$ peak at 72.7 eV. A shift in this direction can only be attributed to Al atoms which are entirely Al-coordinated since the electro-negative environment of O atoms would work in the opposite direction. As described above, a shoulder at the low binding-energy side of the of the $2p_{3/2}$ peak was previously observed by Berg *et al.* and tentatively assigned to a (mono-atomic) semi-amorphous Al layer at the Al-Al₂O₃ interface. The peak responsible for this shoulder represented a chemical shift of only 0.14 eV with respect to the $2p_{3/2}$ peak and it is at present unclear whether the present peak could be attributed to this layer also. This issue will hopefully be clarified by the peak fitting which remains to be done, and eventual input from theoretical calculations. Also, the experiment should be repeated on a new long-term sputtered surface to see if the spectra are reproducible, and spectra should be recorded at a couple of additional, more surface-sensitive, photon energies to be able to estimate the order of the crystal "layers" responsible for the different peaks. In addition, it would be interesting to investigate the characteristics of the core-level peaks as a function of oxygen coverage and to investigate how long sputtering time is needed to obtain reproducible results when changing between different coverages, i.e. to clarify whether diffusion of oxygen into the bulk plays a role.

5.5 The VUV light source of high-order harmonics

The VUV light source of high-order harmonics to be used in the fs VUV CLS setup has been optimized and characterized in order to demonstrate that the 63rd harmonic (96.4 eV) of a 810 nm, 100 fs pulsed Ti:Sapphire laser could be generated. In addition, the reflectivities of a collection of home-made multilayer mirrors optimized for this photon energy have been tested.

The 63rd harmonic represents the highest order that can be selected with a Mo/Si mirror which is intended for the future fs VUV core-level studies. Mo/Si mirrors are widely used for photon energies below the absorption edge of Si at 99 eV due to their high reflectivity; $\sim 70\%$ can be obtained at normal incidence just below the absorption edge [97, 132]. A similarly high reflectivity can be obtained with a Mo/Be mirror just below the Be absorption edge at 111 eV but such mirrors are more difficult to manufacture and a Mo/Si mirror has, accordingly, been chosen for the present purpose.

Also, the 96.4 eV represents a realistic choice of photon energy considering the previous experimental experiences with high-harmonic generation and the ≤ 10 mJ laser pulse energy available in our laboratory. The highest photon energy that has been effectively generated with ~ 100 fs pulses is 135 eV (order 87th) using ≤ 35 mJ laser pulses with a sech^2 spatial profile focused to an intensity of 10^{15} W/cm² with a 60 cm lens in a 1 mm long Ne gas cell [133]. In another experiment, focusing 6 mJ, 200 fs Gaussian pulses with a 25 cm lens to an intensity of 3.5×10^{15} W/cm² in a Ne gas jet, harmonics were effectively generated up to 107 eV (order 69th) and the cut-off frequency was observed to decrease at lower intensities [134]. With the same conditions but using He for the gas medium, harmonics could be effectively generated up to 119 eV (order 77th) but at a reduced efficiency. Finally, harmonics have been effectively generated beyond 122 eV (order 79th) in Ne and 144 eV (order 93th) in He gas jets, respectively, by focusing ≤ 250 mJ, 150 fs Gaussian pulses with a 1 or 2 m lens to an intensity around saturation (8×10^{14} W/cm² for Ne) [135]. For the present purpose Ne seems to be the best choice for the gas medium, compromising the needs for the highest possible photon flux and photon energy.

The setup used for the optimization and characterization of the VUV light source consists of a small vacuum chamber with a pulsed gas-jet valve (General Valve) for high-harmonic generation (HHG), and a McPherson VUV spectrometer (model 247) with a 600 lines/mm concave aluminum grating, as shown in figure 5.10. The concave grating and the entrance- and exit slits of the spectrometer are placed tangentially to a circle with a diameter equal to the 200 mm radius of curvature of the grating. By this configuration, proposed by Rowland, a vertical line image of a point source placed at the entrance slit is provided at the exit slit and a spectrum is obtained by scanning the exit slit along the circle [136]. Radiation with a wavelength λ incident on the grating at a fixed angle $\beta = 86^\circ$ with respect to the surface normal is dispersed according to the grating formula into the angle $\theta > 0$ given by $m\lambda = d(\sin \beta + \sin \theta)$, where m is the diffraction order and d the groove spacing [136]. The exit slit is mounted on a flexible bellow and can be scanned within the 8–120 nm wavelength range. The short-wavelength

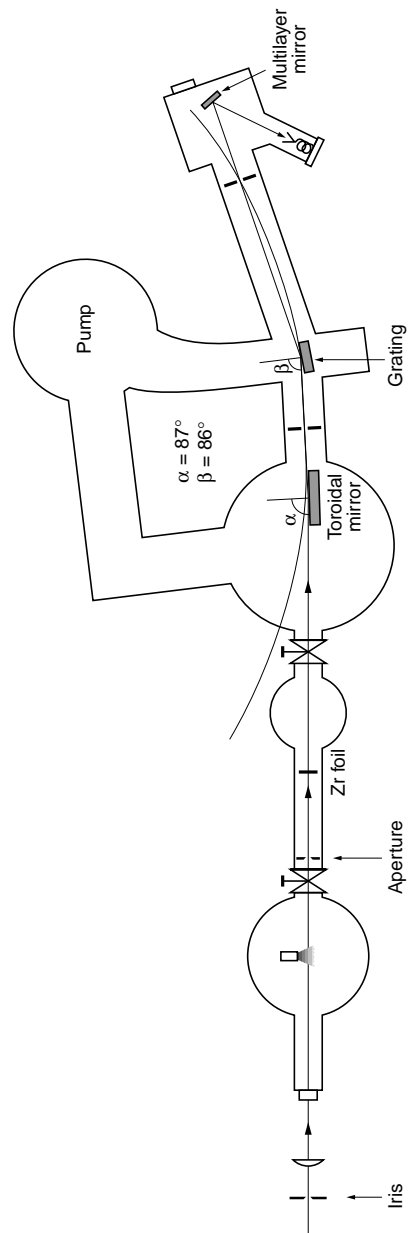


Figure 5.10: A schematic of the experimental setup used for generation and characterization of high-order harmonics.

limit is set by the absorption cut-off of the grating (probably due to pump-oil contamination) while the long-wavelength limit is given by the length of the bellow (the longer the wavelength the more stretched the bellow).

The harmonics are generated with the 810 nm, 10 Hz, 100 fs pulsed output from a Ti:Sapphire laser system, consisting of an oscillator and a regenerative amplifier system from Clark-MXR in addition to a home-built butterfly amplifier. The Ti:Sapphire gain medium of the oscillator is pumped with the 5 W, continuous-wave output from an Ar⁺ laser, and ~ 3 nJ, ~ 800 nm, ~ 100 fs pulses are generated by the mechanism of Kerr-lens modelocking [137] at a repetition rate of 91 MHz. The 3 nJ, ~ 50 fs pulses are stretched to ~ 100 ps by means of a number of reflections from a grating and subsequently regeneratively amplified to ~ 1.5 mJ in another Ti:Sapphire crystal pumped with 7 mJ, 532 nm, 1 kHz, 50–100 ns pulses from a Nd:YAlG laser. The 1.5 mJ pulses are further amplified to ~ 35 mJ by passing four times through a butterfly amplifier with a third Ti:Sapphire crystal, pumped by the ~ 220 mJ, 532 nm, 10 Hz, ns pulsed output from a second Nd:YAlG laser. The ~ 35 mJ are finally compressed to ~ 100 fs by undergoing a number of reflections from another grating, compensating for the chirp and group-velocity dispersion introduced by the stretcher and the gain media. The commercial compressor is not designed for this last amplification step as reflected by the resulting modest output of ~ 8 mJ/pulse which is limited by the damage threshold of the grating.

The resulting ~ 8 mJ, 810 nm, 100 fs pulses are focused with a 50 cm lens to an intensity of 3.4×10^{15} W/cm² in the Ne gas jet. The generated, diverging VUV light is focused ~ 10 cm in front of the entrance slit of the spectrometer by a toroidal gold mirror with estimated horizontal- and vertical radii of curvatures of 3.50 and 0.14 m, respectively. Ideally, the VUV light should be focused onto the entrance slit but this was not possible given the focusing conditions of the toroidal mirror (which had been previously used with the spectrometer for another purpose). The focusing conditions could be improved by moving the gas jet closer to the spectrometer, but this would increase the laser fluence incident on the grating, implying an enhanced risk of damage. A large fraction of the VUV light is thus wasted on the entrance slit but also on the toroidal mirror due to the grazing-incidence configuration, the angle of incidence being $\sim 87^\circ$. With the present configuration the distance from the gas jet to the toroidal mirror is ~ 1.5 m which also leaves space for two valves, an aperture and a ~ 500 Å Zr foil (home-made) in the beam-path. The purpose of the aperture is to limit the pressure rise in the spectrometer from the Ne gas flow which, in addition, is directed into a pump sitting below the chamber. The Zr foil has a transmission of 80–90 % for photon energies above ~ 50 eV and can be pushed into the beam path in order to

prevent stray laser light from reaching the spectrometer. This is necessary for the detection of the highest harmonic orders for which the dispersion angle approaches that of the zeroth-order reflection of the grating. The VUV light is detected with a channeltron detector positioned either directly after the exit slit or following the reflection of the VUV light from the multilayer mirror mounted in a small chamber. The base pressures of the HHG chamber and the spectrometer are 1×10^{-7} and 1×10^{-6} mB, respectively, with the HHG chamber pressure increasing to $\sim 2 \times 10^{-4}$ mB with the gas jet on.

The harmonic yield for the highest orders is optimized by focusing 3 cm in front of the gas jet and by slightly aperturing the laser beam, resulting in a 10 mm beam diameter and a ~ 7 mJ pulse energy. This indicates that the harmonic yield is limited by the phase-matching conditions rather than the (saturation) intensity and the use of a lens with a longer focal length could possibly be advantageous. The gas jet is operated with a Ne backing pressure of 1–2 Bar and a 750 μ s opening time and the laser-beam focus is located at the closest possible vertical distance from the orifice of the 0.8 mm diameter tube extension from which the gas jet originates. Here, the Ne gas pressure is highest and on the order of 150–200 mB, depending on the backing pressure [138]. Under the specified conditions harmonics have been generated up to 118 eV (order 77th) as shown in figure 1.1 of chapter 1. This is in very good agreement with the cut-off energy of 120 eV calculated from the cut-off law $E_{cut} = I_p + 2U_p$ (see chapter 1), assuming a saturation intensity of 8×10^{14} W/cm² [135]. The spectrum was recorded with the Zr foil in the beam path, giving a low-energy cutoff at ~ 55 eV. Assuming a slow variation of the spectrometer efficiency with wavelength, harmonics are seen to be effectively generated up to 112 eV (order 73th), in accordance with the previous experiments referred to above.

Figure 5.11 shows a high-resolution (~ 0.1 eV FWHM) spectrum of the 63rd harmonic which has been fitted to a Gaussian function to yield a width of 1.4 eV (FWHM). This width is much larger than expected and much larger than the value of 0.43 eV recently reported for the 47th–55th harmonics generated with 2.5 mJ, 800 nm, 70 fs laser pulses focused to an intensity of 5×10^{14} W/cm² in a Ne gas jet [139]. In that experiment the width was observed to increase gradually from 0.11 eV at the 7th to 0.37 eV at the 45th harmonic, then stabilizing at the 0.43 eV. The disagreement could be ascribed to the intensity of the laser beam in the present experiment being well above that of saturation. In a previous experiment the spectrum of the 15th harmonic generated in Xe was found to broaden by almost a factor of two, following an increase in the intensity by a factor of three from a value just below saturation [135]. With an estimated saturation intensity for Ne of $\sim 8 \times 10^{14}$ W/cm² [135] the intensity of the present experiment is likely

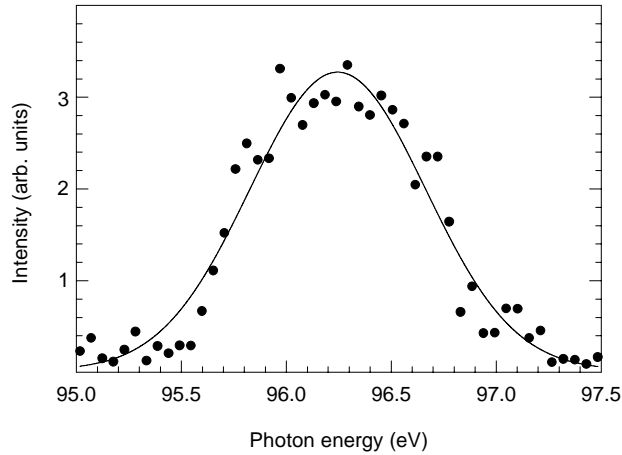


Figure 5.11: The spectral profile of the 63rd harmonic fitted to a Gaussian function with a width of 1.4 eV (FWHM).

a factor of four larger than necessary, implying a broadening by at least a factor of two. This issue could be investigated by increasing the focal length of the lens to, e.g., 100 cm, thereby reducing the intensity from 3.4×10^{15} to 8.4×10^{14} W/cm² and simultaneously improving the phase-matching conditions. With the multilayer-mirror tests being urgently needed there has, unfortunately, not yet been time for that.

The multilayer mirrors are made at Aarhus University by Jacques Chevalier, and designed for optimum (65 %) reflectivity at 96.4 eV and a 67.5° angle of incidence with respect to the mirror surface. This corresponds to a Mo/Si bilayer thickness d of 70.5 Å, given the Bragg condition $2d \sin \phi = \lambda$ where λ is the VUV wavelength and ϕ the angle of incidence with respect to the surface [97]. The bandwidth of the mirror scales approximately like $1/N$ [97], N being the number of Mo/Si bilayers, up to $N \sim 40$, which is chosen for the present mirror. Beyond this value the bandwidth is entirely determined by the ratio R of the Mo to Si thickness as can be verified by reflectivity calculations at the web-page of the Center for X-ray Optics (CXRO) at the Lawrence Berkeley National Laboratory (www-cxro.lbl.gov). From such calculations the optimum value of R has been found to be 0.2, given the fact that the reflectivity as well as the bandwidth decrease with decreasing R . A further decrease in R also implies a decrease in the Mo layer thickness below 1.4 nm which represents a challenge to the manufacturer [140]. The layer thickness could be increased by decreasing ϕ but this would give rise to an enhanced astigmatism when using a spherical focussing mirror as desired for

the present purpose. The choice of $\phi = 67.5^\circ$ is a result of these considerations in addition to the physical constraints imposed by the future setup (cf. figure 5.13). The Mo/Si mirror is fabricated by deposition of alternating layers of Mo and Si sputtered off a target material by Ar^+ bombardment in a vacuum chamber [97]. The layer thickness can be adjusted by varying the Ar pressure and the target potential but given the present uncertainty in these parameters the layer thicknesses can only be controlled to a precision of a couple of Å. Since an uncertainty in bilayer thickness of 1 Å implies an uncertainty in the photon energy of at least 1 eV it has been necessary to make a series of multilayer mirrors under slightly different conditions in the hope that one of them would exhibit the desired properties. Since appropriate equipment for characterization of the multilayer mirrors is not yet available at the institute, it has been necessary to test them directly with the high-order harmonics under conditions mimicking those of the future setup, i.e. with the harmonics incident at a 67.5° angle with respect to the mirror surface, as shown in figure 5.10.

In figure 5.12 (a) an example of a harmonic spectrum, recorded in the vicinity of the 63rd harmonic, is shown before (grey) and after (black) insertion of a representative multilayer mirror. Both spectra have been recorded without the Zr foil in the beam path and the reflected signal from the multilayer mirror has been optimized on the detector by tilting the mirror. Subtracting the ~ 1 V background level of the grey spectrum which is due to stray laser light in the spectrometer, the reflectivity of the mirror is seen to peak at the 61st harmonic and is on the order of 30 %. Theoretically, the reflectivity of the mirror should be ~ 65 %, assuming $R = 0.2$, and the reduced efficiency is attributed to the use of a dielectric mirror substrate which has not been properly grounded during the sputter-deposition process [141]. Some initial tests of mirrors produced on plane crystalline Si substrates did, indeed, yield a higher peak reflectivity but such substrates cannot be used for the fs VUV CLS setup where a spherical focusing mirror with a 100 cm radius of curvature is needed. As an additional drawback, the spherical, dielectric mirror substrates exhibit an enhanced surface roughness which could equally well be responsible for the reduced reflectivity. Unfortunately it has not been possible to "hit" the 63rd harmonic yet with the present, unsatisfactory fabrication procedure but the situation will hopefully improve in the near future, following the purchase of some more precise instruments. The apparent shift of the 61st harmonic of the multilayer-mirror spectrum towards a lower photon energy is attributed to the extra weight introduced by the multilayer-mirror chamber modifying the calibration of the spectrometer. The multilayer-mirror spectrum from figure 5.12 (a) is reproduced on an enlarged scale in figure 5.12 (b) together with the theoretical predictions

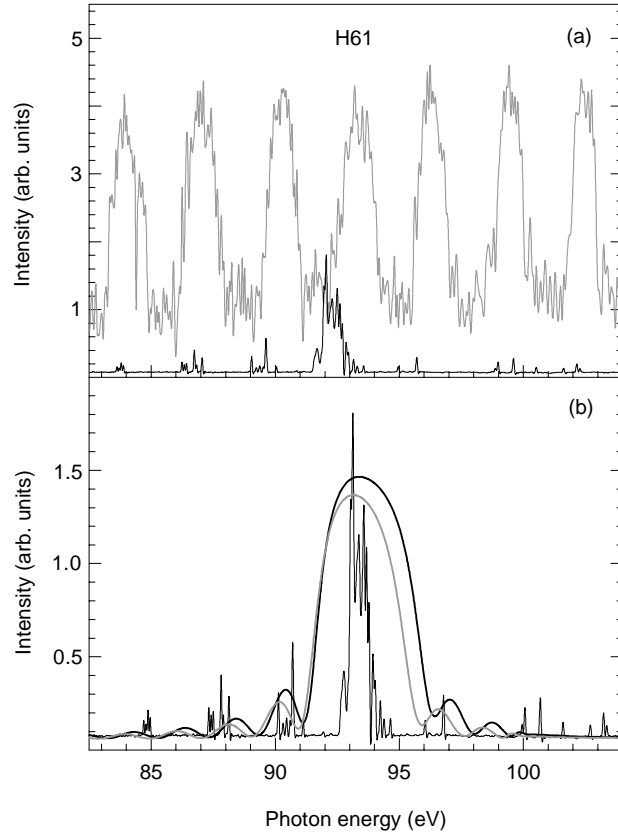


Figure 5.12: (a) A survey of the harmonic spectrum in the vicinity of the 63rd order before (grey) and after (black) reflection from a multilayer mirror. (b) The multilayer-mirror spectrum from (a) together with theoretical predictions for the reflectivity for Mo/Si layer ratios of 0.2 (grey) and 0.25 (black), respectively, assuming a 7.3 nm bilayer thickness.

for the reflectivity for $R = 0.2$ (grey) and 0.25 (black), respectively, assuming a bilayer thickness of 7.3 nm. The theoretical curves, exhibiting peak reflectivities of 65 % and 70 %, respectively, have been scaled to fit the height of the measured spectrum which has been calibrated to the actual wavelength of the 61st harmonic. The bandwidth is seen to increase by ~ 0.5 eV towards higher photon energies when going from $R = 0.25$ to $R = 0.2$, in principle leaving space for an adjacent harmonic order below the envelope.

5.6 Future prospects

Following the completion of the preparations described in the preceding three sections the next step towards fs VUV core-level spectroscopy is the test of a newly constructed electron spectrometer for kinetic-energy analysis of the core-ionized photoelectrons. Due to the modest photon flux expected from the VUV light source (see chapter 1), the electron spectrometer should have the highest possible collection efficiency, favouring a parabolic-mirror time-of-flight spectrometer. This spectrometer consists of a 1 m long flight tube and a pair of closely spaced paraboloid-shaped grids made of thin metal-wire mesh [142]. The inner- and outer grids are at ground- and negative potentials, respectively, such that photoelectrons emitted from the (approximately common) focal point of the paraboloids will be reflected into a parallel beam directed towards the flight tube. By this method all electrons emitted within $\sim \pi$ steradians are collected and recorded by an MCP detector terminating the flight tube. A schematic of the electron spectrometer mounted on the UHV target chamber is shown in figure 5.13 as it is visualized for the future setup including the fs VUV light source. The paraboloids are made of woven stainless-steel mesh with the highest available wire density and transmission (100×100 wires/inch and 81 %, respectively, from Unique Wire), stretched into paraboloidal shape and stiffened with a gold coating. A focal length of 10 mm of the paraboloids has been found to fit the diameter of the flight tube, leaving space enough for the sample holder which is attached to a manipulator extending from the top of the UHV chamber. The spacing between the grids should be small compared to the curvature of the grids in order to minimize the velocity dispersion of the photoelectrons [142], and is 1 mm in the present case. The paraboloids are mounted on a manipulator which can be retracted in order to ease the rotation of the sample towards the sputter gun. The time-of-flight tube is shielded with μ metal to avoid eventual magnetic field-induced deflection of the electrons, which will be retarded to a few eV and slightly focused by an electrostatic lens system positioned at the entrance to the flight tube. The retardation improves the energy resolution of the spectrometer and is maintained along the tube by means of a grid fastened to the hindmost of the three circularly apertured plates constituting the lens system. The electron spectrometer has very recently been mounted on the UHV chamber and will be tested in the near future—initially with 266 nm laser light incident on an Al surface and later with the 63rd harmonic. Assuming $\sim 10^4$ VUV photons/pulse incident on the surface, an electron mean-escape depth to VUV absorption-depth ratio of 1 to ~ 25 (Al at 96 eV) and a quantum efficiency of 100 %, a count rate of $\sim 2 \times 10^3$ photoelectrons per second (10 Hz) is expected which should provide

sufficient statistics for a core-level spectrum within one hour of measurement time.

For the fs laser-induced desorption studies, the almost co-propagating laser pump- and harmonic probe beams will be incident on the surface at a 45° angle through a hole in the parabolic grids drilled by the laser beam. The angle between the two beams should be kept small in order to reduce the temporal walk-off and the harmonic beam should be horizontally polarized since the photoelectrons are preferentially emitted in the polarization direction [143]. The pump beam will be focused on the sample by an external lens while the VUV beam profile from the gas jet will be imaged to a slightly astigmatic $\sim 50 \mu\text{m}$ diameter spot by the spherical multilayer mirror. The target chamber is equipped with standard equipment for surface preparation, i.e. a sputter gun, LEED apparatus, a quadropole mass spectrometer (QMS) and a pulsed valve (General Valve) for gas dosing during desorption measurements. The temperature can be measured with an Alumel-Chromel thermocouple attached to the sample holder which can be liquid-nitrogen cooled to -170°C and radiatively heated from behind by a tungsten filament. For systems like O/Al where the adsorption layer does not saturate at a given coverage, some sort of feed-back mechanism will have to be invented to ensure a constant coverage between successive desorbing laser pulses. Alternatively, the experiments may be performed in a single-shot mode where the sample is moved between successive laser pulses. The UHV environment ($\sim 10^{-10}$ Torr) of the target chamber is separated from the $\sim 10^{-6}$ Torr vacuum of the VUV light generation part by a $\sim 1000 \text{ \AA}$ thick polyimide foil (from Luxel) mounted on a VAT valve. The polyimide foil can withstand a pressure difference of a few Torr, is transparent in the visible and has a 80 % transmission around 10 nm. A $\sim 500 \text{ \AA}$ Zr foil with a 80–90 % transmission above $\sim 60 \text{ eV}$ can be inserted into the beam path to prevent the remaining fundamental laser light of the harmonic beam from propagating through the system. By switching a plane gold mirror into the VUV beam path between the gas jet and the multilayer mirror, the harmonic beam can be directed into the McPherson VUV spectrometer via the toroidal gold mirror (two mirrors are needed for a reasonable reflectivity in the VUV). This facilitates the optimization and characterization of the VUV light source without the need for a re-arrangement of the experimental equipment. An MCP detector placed in the target chamber in the VUV beam direction will be used for alignment of the VUV beam and possibly for a relative measurement of the VUV flux.

The temporal overlap between the pump- and probe pulses can be found by replacing the metal target with a non-linear crystal and looking for second-harmonic light generated by the simultaneous presence of the visible parts of the two beams. Alternatively, one could look in the core-level photoelectron

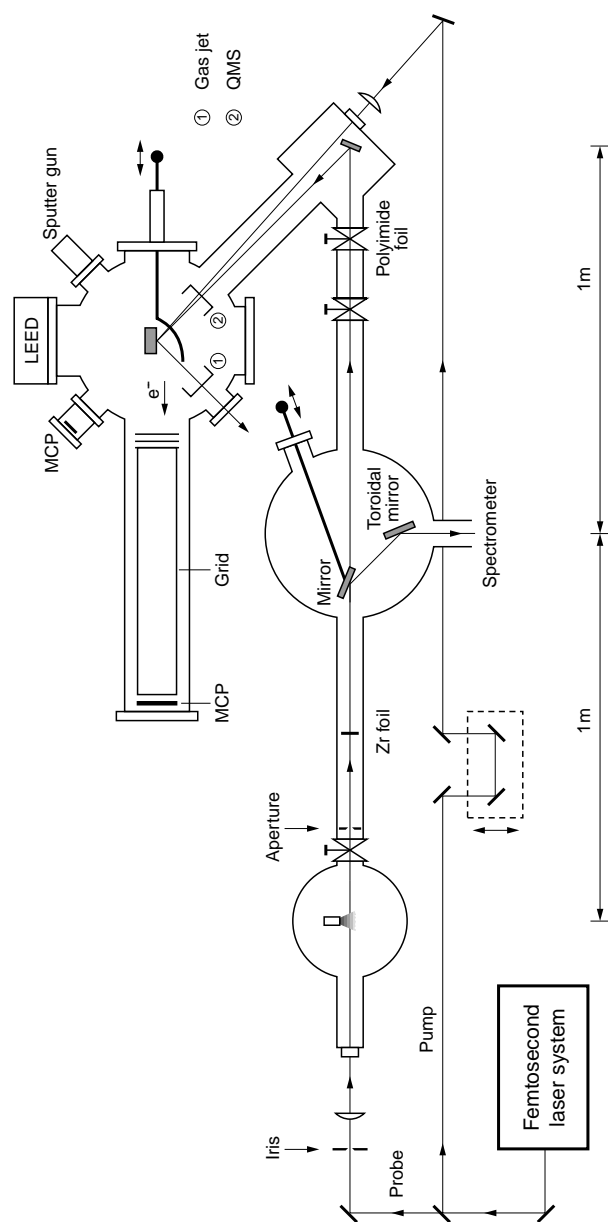


Figure 5.13: A schematic of the future experimental setup for fs VUV core-level spectroscopic studies of surface dynamics.

spectrum of the surface for evidence of laser-assisted photoionization (LAPI). As stated in section 1.3 of chapter 1, LAPI may be recognized in the kinetic-energy spectrum as side-peaks, separated from the core-level peak by an integral multiple of the photon energy of the pump. These peaks are the result of the stimulated emission or -absorption of one or more laser photons taking place during the VUV photoionization process. LAPI has so far only been studied with gaseous media [144, 145], but could also be worth a study at the surface. Denoting by σ_n the differential cross section for coupling of an ionized electron with momentum \vec{p} with n optical photons from the laser field with frequency ω_l and assuming that $\sum_n \sigma_n = \sigma^\circ$ with σ° being the differential cross section in the absence of the laser field, the probability for coupling with n photons is given by [145]

$$P_n = \frac{\sigma_n}{\sum_n \sigma_n} = \frac{\sigma_n}{\sigma^\circ} = J_n^2 \left(\frac{-e\vec{A}_{ol} \cdot \vec{p} - U_p}{m\hbar\omega_1}, 2\hbar\omega_1 \right). \quad (5.2)$$

Here, J_n is a generalized Bessel function, \vec{A}_{ol} the amplitude of the vector potential of the laser field, U_p the ponderomotive energy of a free electron in the laser field, e the elementary charge and m the electronic mass. In the above it has been assumed that \vec{p} is independent of n , equivalent to $\omega_{\text{VUV}} \gg \omega_l$, where ω_{VUV} is the VUV frequency. This expression has been derived by Glover *et al.* for the $1s$ state of the hydrogenic atom [145] but can be shown to be valid for any initial state which can be written in a basis of products of single-electron orbitals [146]. P_n is seen to depend on the angle between \vec{A}_{ol} and \vec{p} , being maximum for $\vec{A}_{ol} \parallel \vec{p}$ ($n \neq 0$). Since photoelectrons are preferentially emitted in the direction of polarization of the VUV light, \vec{A}_{VUV} , the total amount of electrons in the sidepeaks is maximum for $\vec{A}_{ol} \parallel \vec{A}_{\text{VUV}}$, and emitted in that direction. The probability P_n of generating sidepeaks increases with intensity since $A_{ol} \propto \sqrt{I}$ and $U_p \propto I$ and VUV frequency since $p \propto \omega_2$, with I being the laser peak intensity. When studying LAPI at surfaces, the intensity must be chosen with the damage threshold of the surface in mind. For Al the damage intensity for 100 fs pulses is on the order of $\sim 10^{12}$ W/cm² (100 mJ/cm² fluence [147]), yielding coupling efficiencies of $P_0 = 0.19$, $P_1 = 0.33$, $P_{-1} = 0.27$, $P_2 = 0.12$ and $P_{-2} = 0.07$ for 100 eV photons. At least the first-order sidepeaks should be clearly visible in the Al $2p$ core-level spectrum even for fluences well below the damage threshold.

Apart from the O/Al(111) system there are various other potential candidates for surface dynamical studies using the fs VUV CLS setup. Since most adsorbate-substrate systems should be expected to be amenable to laser-induced, substrate-mediated desorption, the limitations to the fs VUV CLS technique are imposed by the deviations of the actual kinetic energies of the

core-ionized photoelectrons from the optimum ~ 50 eV. Since the growth of the inelastic mean-free path is faster towards lower kinetic energies when going away from this value (staying below 10 Å in the 20–250 eV region), one should probably concentrate on systems with more loosely bound core-levels than has been done here. The $4f$ core-levels of the metals to the left of Pt in the third transition-metal group, i.e. Ta [148], W [149], Re [150], Os, and Ir [151] are all in the 20–60 eV range—increasing from the left of the periodic table—and have been clearly resolved with ≤ 100 eV photons. These systems could like-wise act as important model systems for desorption dynamics, although catalytically not quite as relevant as Pt.

The semiconductor elements Ga, Ge, As, Se, In and Sb have $3d$ or $4d$ core-levels in the 20–50 eV range which are known to behave properly for ≤ 100 eV incident photons [152, 153, 154, 155]. In addition, the photo-induced reaction dynamics of adsorbates on semiconductors—in particular Si, Ge and GaAs—is technologically highly relevant and has been the subject of numerous studies using either continuous-wave light [156, 157], synchrotron radiation [158] or ns laser pulses [159, 160, 161]. These studies have included the passivating oxidation-, nitridation- and sulfidation reactions using O_2 [157], NO [156], NH_3 [161] and H_2S [158] adsorbates, and the photo-assisted etching by adsorbed halogen molecules (Cl_2) [160]. All of these systems have been the subjects of core-level spectroscopic studies and pronounced chemical shifts induced by the presence of the adsorbate have been observed (see, e.g., [162, 163, 164, 165]).

Departing from the dynamics associated with the desorption or reaction of adsorbed species, one could follow the foot steps of the fs X-ray diffraction experiments mentioned in the introduction and study the evolution in a semiconductor core-level spectrum following the excitation of the bare surface with a visible pump pulse. The use of a completely different technique might shed some new light on, e.g., the non-thermal melting process observed in InSb [19, 21], Ge [20] and GaAs [22, 23], and the nature of the band-structure collapse (equivalent to a semiconductor-to-metal transition) which has been observed in GaAs but apparently not in InSb [166]. Another experiment could address the amorphous-to-crystalline phase-transition in GeSb of relevance for optical data storage [167] or a non-specified phase transition recently observed in fs laser-excited Al in an all-optical reflectivity measurement [168].

References

- [1] G. A. Somorjai, *Introduction to Surface Chemistry and Catalysis* (John Wiley & Sons, New York, 1994).
- [2] G. C. Bond, *Heterogeneous Catalysis* (Clarendon Press, Oxford, 1990).
- [3] F. Besenbacher *et al.*, *Science* **279**, 1913 (1998).
- [4] L. Österlund *et al.*, *Phys. Rev. Lett.* **86**, 460 (2001).
- [5] J. P. Long *et al.*, *J. Opt. Soc. Am. B* **13**, 201 (1996).
- [6] M. Marsi *et al.*, *Nucl. Inst. Meth. A* **393**, 548 (1997).
- [7] T. Quast *et al.*, *J. Appl. Phys.* **83**, 1642 (1998).
- [8] R. Haight, *Surf. Sci. Rep.* **21**, 275 (1995).
- [9] A. Rettenberger and R. Haight, *Surf. Sci.* **414**, 197 (1998).
- [10] P. Villorosi, *Appl. Opt.* **38**, 6040 (1999).
- [11] H. S. Karlsson and U. O. Karlsson, *Phys. Rev. B* **59**, 10796 (1999).
- [12] G. Tsilimis *et al.*, in *Book of Abstracts of the Adriatico Research Conference on Lasers in Surface Science*, edited by H.-J. Freund *et al.* (Miramare-Trieste, Italy, 2000).
- [13] L. Hernández-Pozos *et al.*, in *Book of Abstracts of the Adriatico Research Conference on Lasers in Surface Science*, edited by H.-J. Freund *et al.* (Miramare-Trieste, Italy, 2000).
- [14] M. Bauer *et al.*, *Phys. Rev. Lett.* **87**, 025501 (2001).
- [15] P. Siffalovic *et al.*, *Rev. Sci. Instrum.* **72**, 30 (2001).
- [16] A. M. Lindenberg *et al.*, *Phys. Rev. Lett.* **84**, 111 (2000).

-
- [17] A. Cavalleri *et al.*, Phys. Rev. Lett. **85**, 586 (2000).
- [18] C. Rose-Petruck *et al.*, Nature **398**, 310 (1999).
- [19] A. H. Chin *et al.*, Phys. Rev. Lett. **83**, 336 (1999).
- [20] C. W. Siders *et al.*, Science **286**, 1340 (1999).
- [21] A. Rousse *et al.*, Nature **410**, 65 (2001).
- [22] K. Sokolowski-Tinten *et al.*, Phys. Rev. B **51**, 14186 (1995).
- [23] L. Huang *et al.*, Phys. Rev. Lett. **80**, 185 (1998).
- [24] X.-L. Zhou *et al.*, Surf. Sci. Rep. **13**, 73 (1991).
- [25] R. R. Cavanagh *et al.*, J. Phys. Chem. **97**, 786 (1993).
- [26] E. Hasselbrink, Appl. Surf. Sci. **79/80**, 34 (1994).
- [27] *Laser Spectroscopy and Photochemistry on Metal Surfaces, part II*, edited by H.-L. Dai and W. Ho (World Scientific, Singapore, 1995).
- [28] F. M. Zimmermann and W. Ho, Surf. Sci. Rep. **22**, 127 (1995).
- [29] W. Ho, J. Phys. Chem. **100**, 13050 (1996).
- [30] A. R. Burns *et al.*, Surf. Sci. **363**, 303 (1996).
- [31] R. Finley and E. Mazur, in *Ultrafast Dynamics of Quantum Systems: Physical Processes and Spectroscopic Techniques*, edited by B. D. Bartolo (Plenum, NATO ASI Series, 1998).
- [32] R. Franchy, Rep. Prog. Phys. **61**, 691 (1998).
- [33] H. Guo *et al.*, Prog. Surf. Sci. **62**, 239 (1999).
- [34] D. G. Busch *et al.*, Phys. Rev. Lett. **75**, 673 (1995).
- [35] T.-H. Her *et al.*, J. Chem. Phys. **108**, 8595 (1998).
- [36] J. A. Prybyla *et al.*, Phys. Rev. Lett. **64**, 1537 (1990).
- [37] F. Budde *et al.*, Surf. Sci. **283**, 143 (1993).
- [38] L. M. Struck *et al.*, Phys. Rev. Lett. **77**, 4576 (1996).
- [39] F.-J. Kao *et al.*, Phys. Rev. Lett. **71**, 2094 (1993).

-
- [40] T. A. Germer *et al.*, Phys. Rev. Lett. **71**, 3327 (1993).
- [41] J. A. Prybyla *et al.*, Phys. Rev. Lett. **68**, 503 (1992).
- [42] R. I. Masel, *Principles of Adsorption and Reaction on Solid Surfaces* (John Wiley & Sons, New York, 1996).
- [43] W. Ho, in *Laser Spectroscopy and Photochemistry on Metal Surfaces, part II*, edited by H.-L. Dai and W. Ho (World Scientific, Singapore, 1995).
- [44] X.-Y. Zhu and J. M. White, Phys. Rev. Lett. **68**, 3359 (1992).
- [45] W. Nessler *et al.*, Surf. Sci. **352-354**, 189 (1996).
- [46] W. S. Fann *et al.*, Phys. Rev. Lett. **68**, 2834 (1992).
- [47] M. Bonn *et al.*, Science **285**, 1042 (1999).
- [48] E. Knoesel *et al.*, Phys. Rev. B **57**, 12812 (1998).
- [49] J. Kliewer *et al.*, Science **288**, 1399 (2000).
- [50] R. H. M. Groeneveld *et al.*, Phys. Rev. B **51**, 11433 (1995).
- [51] S. Deliwala *et al.*, Chem. Phys. Lett. **242**, 617 (1995).
- [52] E. Hasselbrink, in *Laser Spectroscopy and Photochemistry on Metal Surfaces, part II*, edited by H.-L. Dai and W. Ho (World Scientific, Singapore, 1995).
- [53] S. A. Buntin *et al.*, J. Chem. Phys. **91**, 6429 (1989).
- [54] F. Weik *et al.*, J. Chem. Phys. **99**, 682 (1993).
- [55] K. Fukutani *et al.*, Surf. Sci. **311**, 247 (1994).
- [56] K. Fukutani *et al.*, J. Chem. Phys. **103**, 2221 (1995).
- [57] V. Rehn and R. A. Rosenberg, in *Synchrotron Radiation Research, Advances in Surface and Interface Science, Vol. 1*, edited by R. Z. Bachrach (Plenum Press, New York, 1992).
- [58] S. Funk *et al.*, J. Chem. Phys. **112**, 9888 (2000).
- [59] J. A. Misewich *et al.*, Surf. Sci. **363**, 204 (1996).
- [60] F.-J. Kao *et al.*, Phys. Rev. Lett. **70**, 4098 (1993).

- [61] R. J. Finlay *et al.*, Chem. Phys. Lett. **274**, 499 (1997).
- [62] J. A. Misewich *et al.*, Phys. Rev. Lett. **68**, 3737 (1992).
- [63] F. Budde *et al.*, Phys. Rev. Lett. **66**, 3024 (1991).
- [64] J. A. Misewich *et al.*, J. Chem. Phys. **100**, 736 (1994).
- [65] G. Ertl and J. Küppers, *Low Energy Electrons and Surface Chemistry* (VCH Verlagsgesellschaft, Germany, 1985).
- [66] J. Stöhr, in *X-Ray Absorption*, edited by D. C. Koningsberger and R. Prins (John Wiley & Sons, New York, 1988).
- [67] D. P. Woodruff and A. M. Bradshaw, Rep. Prog. Phys. **57**, 1029 (1994).
- [68] W. F. Egelhoff, Surf. Sci. Rep. **6**, 253 (1987).
- [69] D. Spanjaard *et al.*, Surf. Sci. Rep. **5**, 1 (1985).
- [70] S. Hüfner, *Photoelectron Spectroscopy* (Springer, Berlin, 1995).
- [71] N. Mårtensson, in *Applications of Synchrotron Radiation*, edited by W. Eberhardt (Springer, Berlin, 1995).
- [72] F. Besenbacher, Rep. Prog. Phys. **59**, 1737 (1996).
- [73] L. Feldman and J. Mayer, *Fundamentals of Surface and Thin Film Analysis* (North-Holland, New York, 1986).
- [74] J. R. Thompson *et al.*, SPIE **2521**, 113 (1995).
- [75] H. Heinzelmann *et al.*, Phys. Rev. Lett. **70**, 3611 (1993).
- [76] J. N. Andersen *et al.*, Surf. Sci. **289**, 307 (1993).
- [77] S. V. Christensen *et al.*, Phys. Rev. Lett. **76**, 1892 (1996).
- [78] A. Baraldi *et al.*, Surf. Sci. **457**, L354 (2000).
- [79] D. P. Chong and C. Bureau, J. Electron Spect. Rel. Phenom. **106**, 1 (2000).
- [80] O. Plashkevych *et al.*, Chem. Phys. **260**, 11 (2000).
- [81] D. A. Muller, Ultramicroscopy **78**, 163 (1999).

-
- [82] K. Siegbahn *et al.*, *ESCA, Atomic, Molecular and Solid State Structure Studied by Means of Electron Spectroscopy* (Almqvist & Wiksell, Uppsala, 1967).
- [83] R. Nyholm *et al.*, Phys. Rev. B **44**, 10987 (1991).
- [84] R. Nyholm and N. Mårtensson, Chem. Phys. Lett. **74**, 337 (1980).
- [85] J. C. Fuggle and S. F. Alvarado, Phys. Rev. A **22**, 1615 (1980).
- [86] N. Mårtensson and R. Nyholm, Phys. Rev. B **24**, 7121 (1981).
- [87] J. H. Petersen, *Lithium Adsorption on Aluminum Surfaces studied by HRCLS and LEED* (Ph.D. thesis, Institute of Physics and Astronomy, Aarhus University, Denmark, 2000).
- [88] S. Doniach and M. Sunjic, J. Phys. C **3**, 285 (1970).
- [89] J. van Elp *et al.*, Nucl. Inst. Meth. A **381**, 548 (1996).
- [90] N. Mårtensson *et al.*, J. Electron Spect. Rel. Phenom. **70**, 117 (1994).
- [91] G. Carter *et al.*, in *Sputtering by Particle Bombardment, Vol. II*, edited by R. Behrisch (Springer, Berlin, 1983).
- [92] S. Facsko *et al.*, Science **285**, 1551 (1999).
- [93] E. Taglauer, Appl. Phys. A **51**, 238 (1990).
- [94] K. Kern *et al.*, Surf. Sci. **261**, 118 (1992).
- [95] A. Kuznetsova *et al.*, Langmuir **14**, 2502 (1998).
- [96] R. G. Musket *et al.*, Appl. Surf. Sci. **10**, 143 (1982).
- [97] D. Attwood, *Soft X-rays and Extreme Ultraviolet Radiation, Principles and Applications* (Cambridge University Press, United Kingdom, 2000).
- [98] C. Puglia *et al.*, Surf. Sci. **342**, 119 (1995).
- [99] O. Björneholm *et al.*, Surf. Sci. **315**, L983 (1994).
- [100] H. Hopster and H. Ibach, Surf. Sci. **77**, 109 (1978).
- [101] H. Steininger *et al.*, Surf. Sci. **123**, 264 (1982).
- [102] D. A. Wesner *et al.*, Phys. Rev. B **33**, 8837 (1986).
- [103] H. Aizawa and S. Tsuneyuki, Surf. Sci. **399**, L364 (1998).

- [104] R. W. Joyner, in *The Chemical Physics of Solid Surfaces*, edited by D. A. King and D. P. Woodruff (Elsevier, Amsterdam, 1993), Vol. 6.
- [105] W. D. Mieher *et al.*, J. Chem. Phys. **91**, 3228 (1989).
- [106] J. Liu *et al.*, J. Phys. Chem. **99**, 6167 (1995).
- [107] C. Berg *et al.*, Phys. Rev. B **47**, 13063 (1993).
- [108] S. M. Driver *et al.*, Surf. Sci. **391**, 300 (1997).
- [109] S. G. Walton *et al.*, Phys. Rev. B **58**, 15430 (1998).
- [110] J. Jacobsen *et al.*, Phys. Rev. B **52**, 14954 (1995).
- [111] I. P. Batra and L. Kleinman, J. Electron Spect. Rel. Phenom. **33**, 175 (1984).
- [112] T. Hoshino *et al.*, Appl. Surf. Sci. **162-163**, 435 (2000).
- [113] W. Zhu *et al.*, Appl. Phys. Lett. **78**, 3103 (2001).
- [114] A. Jimenez and D. Schmeisser, Surf. Sci. **250**, 59 (1991).
- [115] R. Baxter *et al.*, Surf. Sci. **445**, 448 (2000).
- [116] J. Trost *et al.*, J. Chem. Phys. **108**, 1740 (1998).
- [117] V. Zhukov *et al.*, Surf. Sci. **441**, 240 (1999).
- [118] K. Honkala and K. Laasonen, Phys. Rev. Lett. **84**, 705 (2000).
- [119] A. Kiejna and B. I. Lundqvist, Phys. Rev. B **63**, 085405 (2001).
- [120] R. Chakarova *et al.*, Surf. Sci. **472**, 63 (2001).
- [121] H. Brune *et al.*, J. Chem. Phys. **99**, 2128 (1993).
- [122] E. R. Wouters *et al.*, Surf. Sci. **296**, 141 (1993).
- [123] B. C. Mitrovic and D. J. O'Connor, Surf. Sci. **405**, 261 (1998).
- [124] C. F. McConville *et al.*, Surf. Sci. **188**, 1 (1987).
- [125] V. Zhukov *et al.*, Surf. Sci. **441**, 251 (1999).
- [126] L. Österlund *et al.*, Phys. Rev. B **55**, 15452 (1997).
- [127] V. Zhukov *et al.*, J. Vac. Sci. Technol. **17**, 1727 (1999).

-
- [128] T. Sasaki and T. Ohno, *Surf. Sci.* **454**, 337 (2000).
- [129] I. Popova, private communication (2001).
- [130] S. A. Larson and L. L. Lauderback, *Surf. Sci.* **254**, 161 (1991).
- [131] K. D. Rendulic, *Appl. Phys. A* **47**, 55 (1988).
- [132] J. M. Slaughter *et al.*, *J. Appl. Phys.* **76**, 2144 (1994).
- [133] J. J. Macklin *et al.*, *Phys. Rev. Lett.* **70**, 766 (1993).
- [134] K. Miyazaki and H. Takada, *Phys. Rev. A* **52**, 3007 (1995).
- [135] C.-G. Wahlström *et al.*, *Phys. Rev. A* **48**, 4709 (1993).
- [136] J. A. R. Samson, *Techniques of Vacuum Ultraviolet Spectroscopy* (Cruithne Press, Great Britain, 2000).
- [137] C. Rullière, *Femtosecond Laser Pulses* (Springer, Berlin, 1998).
- [138] C. Altucci *et al.*, *J. Opt. Soc. Am. B* **13**, 148 (1996).
- [139] L. Nugent-Glandorf *et al.*, *Phys. Rev. A* **62**, 023812 (2000).
- [140] P. Dhez, in *Proc. 4th Int. Conf. X-Ray Microscopy* (Moscow, Russia, 1993).
- [141] G. Gutman *et al.*, *Appl. Opt.* **32**, 6981 (1993).
- [142] D. J. Trevor *et al.*, *Rev. Sci. Instrum.* **60**, 1051 (1989).
- [143] V. Schmidt, *Rep. Prog. Phys.* **55**, 1483 (1992).
- [144] J. M. Schins *et al.*, *Phys. Rev. Lett.* **73**, 2180 (1994).
- [145] T. E. Glover *et al.*, *Phys. Rev. Lett.* **76**, 2468 (1996).
- [146] L. B. Madsen, private communication (1999).
- [147] D. M. Riffe *et al.*, *J. Opt. Soc. Am. B* **10**, 1424 (1993).
- [148] D. Sébilleau *et al.*, *J. Phys. C* **21**, 287 (1988).
- [149] G. K. Wertheim and P. H. Citrin, *Phys. Rev. B* **38**, 7820 (1988).
- [150] N. T. Barrett *et al.*, *Surf. Sci.* **286**, 150 (1993).
- [151] J. F. van der Veen *et al.*, *Phys. Rev. Lett.* **44**, 189 (1980).

-
- [152] T.-C. Chiang, *Comments At. Mol. Phys.* **13**, 299 (1983).
- [153] A. B. McLean, *Surf. Sci.* **220**, L671 (1989).
- [154] J. N. Andersen and U. O. Karlsson, *Phys. Rev. B* **41**, 3844 (1990).
- [155] G. L. Lay *et al.*, *Prog. Surf. Sci.* **48**, 145 (1995).
- [156] S. K. So and W. Ho, *Appl. Phys. A* **47**, 213 (1988).
- [157] Y. Chen *et al.*, *J. Chem. Phys.* **95**, 8442 (1991).
- [158] S. Conrad *et al.*, *Surf. Sci.* **382**, 79 (1997).
- [159] L. J. Richter and R. R. Cavanagh, *Prog. Surf. Sci.* **39**, 155 (1992).
- [160] V. Liberman *et al.*, *J. Chem. Phys.* **96**, 1590 (1992).
- [161] X.-Y. Zhu *et al.*, *J. Chem. Phys.* **97**, 5856 (1992).
- [162] R. D. Schnell *et al.*, *Phys. Rev. B* **32**, 8052 (1985).
- [163] W. Ranke and J. Wasserfall, *Surf. Sci.* **292**, 10 (1993).
- [164] B. Murphy *et al.*, *Surf. Sci.* **317**, 73 (1994).
- [165] K. Prabhakaran and T. Ogino, *Surf. Sci.* **325**, 263 (1995).
- [166] I. L. Shumay and U. Höfer, *Phys. Rev. B* **53**, 15878 (1996).
- [167] K. Sokolowski-Tinten *et al.*, *Phys. Rev. Lett.* **81**, 3679 (1998).
- [168] C. Guo *et al.*, *Phys. Rev. Lett.* **84**, 4493 (2000).

Chapter 6

Two-colour pump-probe experiments on He using high-order harmonics

6.1 Introduction

Knowledge about basic atomic and molecular properties such as radiative transition probabilities and excitation- and ionization cross sections is important for the interpretation of astrophysical spectra and in the modelling of stellar properties [1]. For the latter purpose the opacities of stellar envelopes are of particular importance as reflected by the launch of the international Opacity Project [2, 3]. The opacity determines the degree of penetration of radiation through matter and depends on atomic transition frequencies, oscillator strengths and excitation- and ionization cross sections [4]. The Opacity Project aims at systematic and accurate calculations of these quantities using the R-matrix method, in order to compensate for the lack of experimental data [5]. Recently, a synchrotron radiation beamline was constructed at Aarhus University, dedicated to measurements of absolute photoionization cross sections of astrophysically relevant ions. So far, experimental data have been recorded for C^+ , N^+ , O^+ , Mg^+ , Al^+ and S^+ , providing a test ground for the opacity calculations (see, e.g., [6, 7]).

Oscillator strengths (or transition probabilities) are related to the estimated abundances of the elements in the stars, thus constituting important input parameters for models dealing with the origin and evolution of the universe [8]. Since the oscillator strength is proportional to the square of the

matrix element connecting the initial- and final states of a given transition, it provides, in addition, a sensitive test of atomic- and molecular structure theory. In fact, the accuracy of laboratory measurements has reached a level where electron correlation and—especially for larger systems—relativistic effects can no longer be ignored. The many-body approaches are basically the same as those discussed in chapter 2, i.e. relativistic MCHF [9, 10], variational configuration interaction [11], many-body perturbation theory [12] and—for two-electron systems—the hyperspherical-coordinate approach [13]. In fact, the R-matrix method used in negative ion calculations was first applied in connection with—and has thus been adopted from—the Opacity Project [14].

Although fairly accurate, theoretical calculations cannot always be trusted and must be tested against experiments, especially when used in spectral analysis where a higher precision is required [15]. Due to the increased experimental difficulties associated with the UV and VUV regions, the lack of accurately measured oscillator strengths is particularly severe in this wavelength range where demands are increasing with the launches of the EUVE (Extreme Ultraviolet Explorer) and FUSE (Far UltraViolet Spectroscopic Explorer) satellites in 1992 and 1999, respectively [16]. The oscillator strength can be determined either from a measurement of the radiative lifetime of the upper level of the transition combined with a knowledge of the branching ratio for decay to the specific lower level, or from a measurement of either the real or imaginary part of the refractive index of the gas medium [17]. In the latter case, knowing the column density (the volume density times unit length), the oscillator strength can be inferred by exploiting its dependence on the refractive index (i.e. the dispersion or absorption) [18]. In practice, one measures either interferometrically the phase shift, or dispersion, of a (spectrally white) light beam passing through the gas, or—with a spectrometer—the absorption- or emission spectrum of the gas. The column density is, however, not easily determined, and unless the medium is optically thin, the absorption coefficient will depend on the line shape of the transition in a non-trivial way [17]. As a consequence, oscillator strengths are most often determined from lifetime measurements, the branching ratio being known from emission- or absorption experiments using a grating spectrometer or a so-called Fourier-transform spectrometer [19, 20]. The Fourier-transform spectrometer is in essence a Michelson interferometer which, when used with a spectrally (absorption-modulated) white light source gives an intensity variation as a function of delay whose Fourier-transform is the spectral content of the light source [21]. As opposed to a grating spectrometer this has the advantage of using all of the available light for the measurement but due to the presence of the transmittive optics it cannot be applied below ~ 120 nm. Denoting by W_{ka} and W_{ki} the transition rates from the upper level k to the

lower levels a and i , the radiative lifetime τ_k of the upper level is given by

$$\frac{1}{\tau_k} = \sum_i W_{ki} = \frac{W_{ka}}{BR}, \quad (6.1)$$

where $BR = W_{ka}/\sum_i W_{ki}$ is the branching ratio for decay from k to a . The emission oscillator strength f_{ka} (equivalent to the absorption oscillator strength apart from the statistical weights $2J_k + 1$ and $2J_a + 1$ of the upper and lower levels) can then be determined from the relation

$$W_{ka} = \frac{2\omega_{ka}^2}{mc^3} \frac{e^2}{4\pi\epsilon_0} f_{ka} \frac{2J_k + 1}{2J_a + 1}, \quad (6.2)$$

where J_k and J_a are the total orbital angular momenta, ω_{ka} is the transition frequency and e , m , c and ϵ_0 the electronic mass, the elementary charge, the speed of light and the vacuum permittivity, respectively [22].

Lifetimes can be measured by a variety of methods, comprising the atomic- or molecular medium in the form of a vapour or a fast ion beam, some means of excitation of the level of interest and some mechanism for detection of the decay [23, 24, 25]. The excitation is normally induced non-selectively by collisions with an electron beam [26] or a foil [27], or selectively by absorption of laser light, either directly from the ground state [28, 29] or following collisional pre-excitation [30, 31]. The exponential decay is detected by measuring as a function of time the population of the excited state [32] or—with a fast detector—the emitted fluorescence by e.g. the methods of laser-induced fluorescence (LIF) or delayed coincidence [24]. Using a fast beam compromises the need for a fast detector since the time delay is scanned by moving the detection system along the beam line. This technique has provided lifetime values for Li and Na to an accuracy $\sim 0.2\%$ [33] which, however, have been questioned by subsequent theoretical predictions and a less accurate lifetime measurement [34]. With an uncertainty of a few per cent, LIF has proven successful for a vast number of lifetime measurements on laser-produced vapours in the nanosecond regime, using laser pulses of nanosecond- or picosecond duration for the excitation [35]. The applicability of the method is, however, limited by a time resolution of ~ 1 ns and less efficient detection in the VUV spectral region.

For measurements of sub-nanosecond lifetimes the most appealing method is the pump-probe technique, using laser pulses for excitation as well as detection. Using high-order harmonics for the excitation, this technique was demonstrated in the VUV in 1995 by Larsson *et al.* [37]. The 0.57 ns lifetime of the He $1s2p\ ^1P^o$ state located 21.22 eV above the He $1s^2\ ^1S^e$ ground state (see figure 6.1) and well known from previous absorption measurements, was

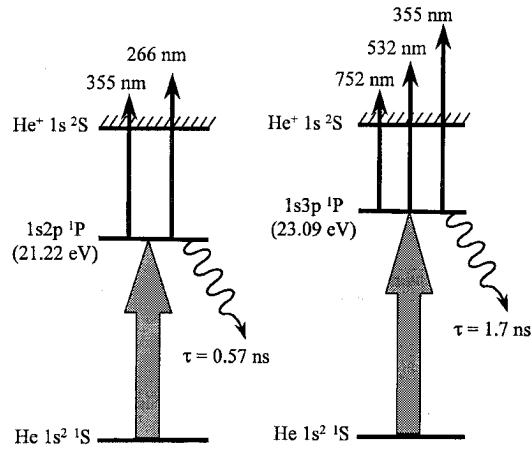


Figure 6.1: Energy level diagram of He indicating the atomic states and laser excitation schemes involved in the photoionization cross-section measurements of Gisselbrecht *et al.* in 1999 [36].

determined to an accuracy of 5 %. The state was resonantly excited with the 13th harmonic of the ~ 50 ps, ~ 759 nm pulsed output from a tunable distributed feedback dye laser (DFDL) and subsequently ionized with ~ 50 ps, 355 nm pulses from a Nd:YAG laser. The ~ 50 ps pulse duration was sufficiently short that the lifetime could be measured and sufficiently long that the mis-match between the laser bandwidth and the atomic linewidth was not too large. This technique was later used for measurements of unknown lifetimes of excited electronic states of CO [32] and N₂ [38], respectively.

By keeping the time delay fixed at a certain value and scanning the pulse energy of the probe while monitoring the ion signal, the technique can, in addition, be used to determine absolute, total, excited-state photoionization cross sections as demonstrated in 1999 by Gisselbrecht *et al.* [36]. Absolute cross sections were obtained for the $1s2p\ ^1P^o$ and $1s3p\ ^1P^o$ states of He for three different photon energies of the probe (cf. figure 6.1) and found to be in good agreement with theory. This method [39, 40] and a variant hereof [41, 42], measuring the fluorescence signal from the excited state decay, have previously been applied to excited states of alkali- and alkaline- earth atoms. Other recent absolute excited-state photoionization cross-section measurements have concentrated on the heavier noble-gas elements Ne [43], Ar, Kr [44, 45] and Xe [46, 47] with reference to their similarity to the theoretically interesting alkali atoms and their relevance in connection with excimer lasers and discharges. All of the noble-gas cross sections were determined

with reference to the theoretically calculated values for He by comparing the excited-state photoelectron spectra of He with that of the other species.

In the 1995 experiment on He a significant increase in the number of He⁺ ions—a "spike"—at zero time delay had sometimes been observed in the exponential decay curve at zero time delay (cf. figure 6.3), and the spike was, in fact, present during all of the 1999 measurements. The purpose of the experiment described in the present chapter was a closer investigation of the origin of this spike and its eventual influence on the measured value of the lifetime for the $1s2p$ state. This issue is important for the applicability of the pump-probe technique to measurements of unknown lifetimes. A secondary purpose of the experiment was a measurement of the ratio of the partial photoionization cross sections for release of either an s - or d -wave electron into the He⁺ continuum, starting from the $1s2p$ state. This can be done by varying the angle of polarization between the pump and the probe as was recently demonstrated in measurements on excited states of Ar [45, 48]. In those experiments the excited states were populated by excitation with synchrotron radiation [48] or by laser excitation of a metastable Ar beam produced in a discharge [45]. By measuring the He⁺ signal as a function of the probe-pulse energy (cf. the 1999 experiment) for two different polarizations, absolute partial photoionization cross sections can, in principle, be obtained.

6.2 Experimental approach

A schematic of the experimental setup, common to the lifetime- and photoionization cross-section measurements, is shown in figure 6.2. The tunable ~ 759 nm laser pulses needed for the resonant excitation of the $1s2p$ level were generated by a distributed feedback dye laser (DFDL) similar to that of Schade *et al.* [49, 50]. The oscillator consists of a mirror-less dye cell in which a dynamic grating—corresponding to a periodic variation of the refractive index—is created by two interfering light beams. The two light beams are the +1st and -1st orders of the 532 nm, 10 Hz, 70 ps pulsed output from a Nd:YAlG laser diffracted from a 1200 lines/mm holographic grating and recombined onto the surface of the dye cell by two mirrors. The period of the interference pattern is given by $\Lambda = \lambda_o / 2n_1 \sin \theta$ where λ_o is the wavelength of the pump, $n_1 = 1$ the refractive index of air and θ the angle of incidence with respect to the surface normal of the dye cell. For parallel mirrors θ is equal to the diffraction angle given by $\sin \theta = \lambda_o / d$ with d being the grating constant, such that $\Lambda = d/2$ is independent of the pump wavelength [51]. The dynamic grating acts like a Bragg mirror, giving constructive interference, i.e. maximum reflectance, of the wavelength λ_{DFDL} fulfilling the Bragg condition $\lambda_{\text{DFDL}} = 2n\Lambda = \lambda_o n / 2 \sin \theta$ where n is the refractive index

of the dye solution. The output wavelength of the DFDL oscillator, λ_{DFDL} , can thus be tuned by adjusting θ (by turning the mirrors) or—on a finer scale—by tuning the refractive index. In order to obtain tunability around the ~ 759 nm required for the present experiment while keeping the mirrors parallel, the angle of incidence θ was increased from that of the +1st and -1st order diffractions by means of a prism inserted in front of the dye cell. The refractive index was tuned by tuning the temperature of the dye solution, resulting in a wavelength change of -0.217 nm/°C. In the experiment, the absolute wavelength could be measured to an accuracy of ~ 0.01 nm with a commercial spectrometer.

Only a fraction of the ~ 25 mJ, 532 nm, 70 ps output from the Nd:YAlG laser was used to pump the DFDL oscillator, the rest being distributed to two dye-cell amplifiers for amplification of the DFDL output to ~ 1.5 mJ/pulse. In addition, a few mJ were split off and mixed with the fundamental 1064 nm output from the Nd:YAlG laser in order to generate ~ 0.5 mJ, 355 nm probe pulses. Further amplification of the DFDL output to ~ 35 mJ/pulse was obtained by five passages through a Ti:Sapphire butterfly amplifier pumped with a total of ~ 400 mJ/pulse from a 532 nm, 10 Hz, 10 ns Nd:YAlG laser. The DFDL pulses are expected to be approximately Fourier-transform limited (time-bandwidth product 0.41) with a pulse duration similar to that of the 70 ps pump laser, implying a bandwidth of ~ 0.05 nm [50].

The resulting DFDL laser beam, consisting of 35 mJ, ~ 759 nm, ~ 70 ps pulses, was focused to an intensity of $\sim 5 \times 10^{14}$ W/cm² in a Kr gas jet with a lens of 12 cm focal length. Harmonic orders were generated up to the 15th with the 13th of 21.22 eV (58.4 nm) photon energy being selected by a 1200 lines/mm holographic grating. The harmonic beam was intersected by the 355 nm probe beam at a 45° angle in a vacuum chamber equipped with a gas jet for He inlet and an Electron-Multiplier Tube (EMT) for detection of the harmonic signal. A flight tube extending from the top of the vacuum chamber and terminated with an EMT, was used for time-of-flight detection of He⁺ ions repelled from the interaction region by a 1 kV potential. The probe beam was focused with a 30 cm lens to a ~ 17 μ m diameter focal spot ~ 7 cm before the interaction region, corresponding to a maximum in the detected He⁺ signal. The corresponding beam diameter in the interaction region was ~ 1 mm. With a probe energy of ~ 350 μ J in the chamber this corresponds to an intensity of $\sim 5 \times 10^8$ W/cm² in the interaction region—very close to the intensity which can be estimated to saturate the transition (using the cross-section value stated in [36]). The probe beam passed through a delay line on its way to the interaction region, and a halfwave plate was positioned in front of the 30 cm lens for rotation of the polarization vector of the (initially) vertically polarized probe beam with respect to the (vertically

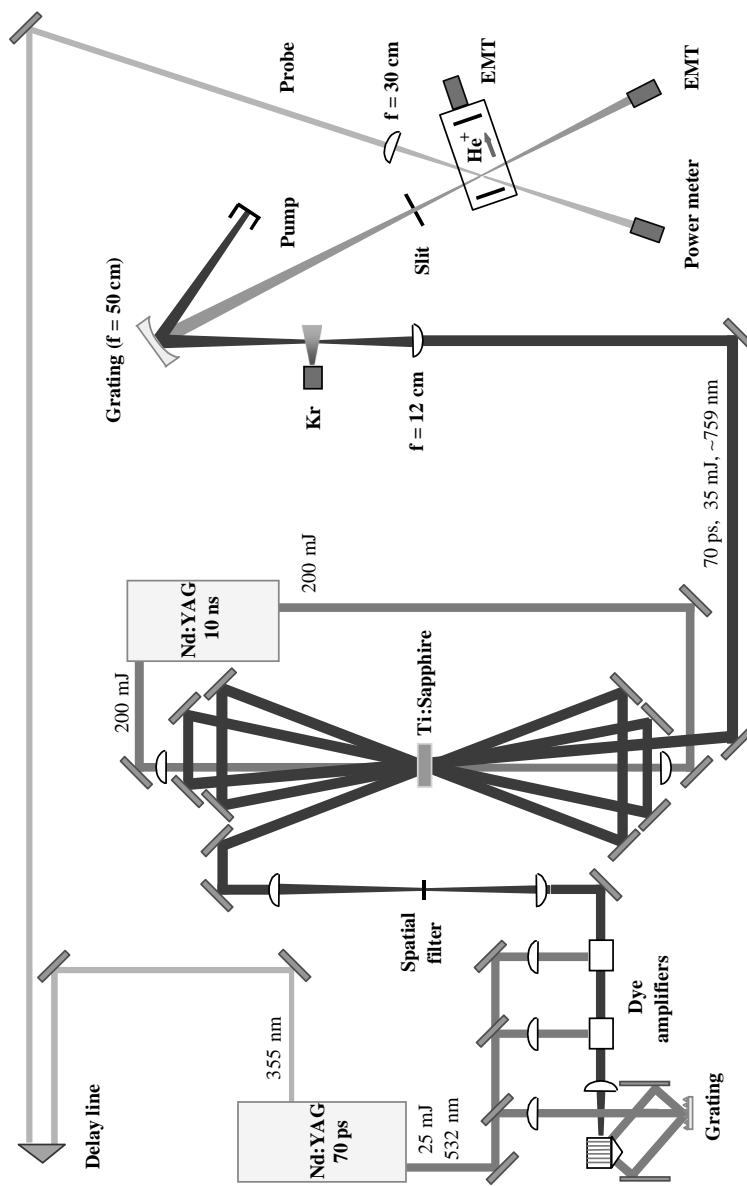


Figure 6.2: A schematic of the experimental setup used for the He 1s2p lifetime and cross-section measurements

polarized) harmonic beam.

The grating of 50 cm focal length created an image of the DFDL beam spot from the Kr gas jet ~ 2 cm before the interaction region, corresponding to a ~ 0.2 mm diameter harmonic beam in the interaction region. This value was confirmed by focusing the probe beam to a ~ 17 μm diameter spot in the center of the interaction region and scanning the 30 cm lens vertically while measuring the He^+ signal. Due to the physical construction of the experimental setup it was not possible to move the vacuum chamber, i.e. the interaction region, closer towards the grating. The base pressure in the chamber was $\sim 1 \times 10^{-6}$ mB with the gas jets turned off and could be kept around this value with the Kr jet on due to a ~ 2 mm slit positioned at the entrance to the chamber. The He gas jet could be operated either in a pulsed mode or with a continuous flow with pressures in the 2×10^{-5} – 6×10^{-4} mB range. For the 13th harmonic, on the order of $\sim 5 \times 10^6$ photons/pulse were present after the grating and the ~ 2 mm slit, as estimated with a calibrated VUV diode placed after an aluminum foil. The bandwidth of the harmonic was determined by measuring the He^+ signal as a function of the DFDL wavelength (cf. figure 6.5), giving a value of 0.0035 nm (1 meV) for a 0.23 ns delay of the probe with respect to the probe (in order to avoid any influence from the spike). For comparison, a value of 0.005 nm was found in the 1999 experiment [36] while 0.01 nm was measured in 1995 [37]. The spectral overlap with the Doppler-broadened width of 0.2 meV of the He $1s2p$ level is reasonable.

6.3 Results and discussion

6.3.1 Lifetime measurements and the role of the spike

From the beginning of the experiment the spike was present at zero time delay in the exponential decay and it turned out that getting rid of it was not so easy (unfortunately, the exact conditions under which the spike-free decay curves had been recorded in 1995 could not be recalled)! Running the He gas jet in pulsed mode and varying the probe-pulse energy and the focusing conditions of the harmonic as well as the probe did not help. The focusing of the harmonic could only be changed by moving the chamber, and the harmonic could only be further defocused since the chamber could only be moved further away from the Kr gas jet. In the end it was decided to reduce the pressure in the interaction region by running the He gas jet with a continuous, static flow, and, in fact, the spike disappeared for pressures below 6×10^{-5} mB. This is illustrated in figure 6.3 which shows the monitored He^+ signal on a semilogarithmic scale as a function of pump-probe delay for

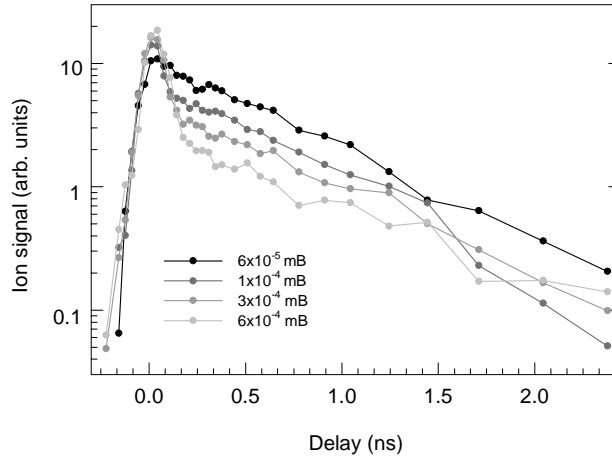


Figure 6.3: Semilogarithmic plot of the He^+ ion signal as a function of pump-probe delay for four different He pressures.

four different pressures. For all of the measurements presented, a probe-pulse energy of $\sim 350 \mu\text{J}/\text{pulse}$ was used. The point of zero delay has been (arbitrarily) chosen as the delay corresponding to a maximum in the ion signal. From figure 6.3 the spike is seen to develop when the pressure is increased from $6 \times 10^{-5} \text{ mB}$ to $6 \times 10^{-4} \text{ mB}$, the latter being the maximum pressure applied considering the presence of the EMT's. The development of the spike is seen to be accompanied by an almost one order-of-magnitude decrease in the ion signal at long delays, implying a much reduced statistics in the tails of the decay curves. Abstracting from the consequent scatter in the data points it is evident that the slopes of the curves are constant, and "only" the uncertainty on the measured lifetime is affected by the presence of the spike. The influence of the pressure is further illustrated in figure 6.4 where the magnitude of the ion signal at zero (black) and 0.23 ns (grey) delays, respectively, is depicted as a function of pressure. The off-spike ion signal increases up to $\sim 2 \times 10^{-5} \text{ mB}$ and then decreases, while the on-spike signal increases up to $\sim 6 \times 10^{-4} \text{ mB}$ and then saturates. The presence of the spike is also signified in the harmonic spectral profile which is broadened by almost a factor of two when the pump- and probe pulses overlap in time. This is illustrated in figure 6.5, showing the apparent harmonic profile at zero (black) and 0.23 ns (grey) delays, respectively, for a pressure of $6 \times 10^{-4} \text{ mB}$. Subsequent fits of the profiles to a Gaussian function yielded widths (FWHM) of 0.0057 and 0.0035 nm for the on- and off-spike conditions, respectively, and corresponding mean wavelengths of 58.4292 and 58.4295 nm.

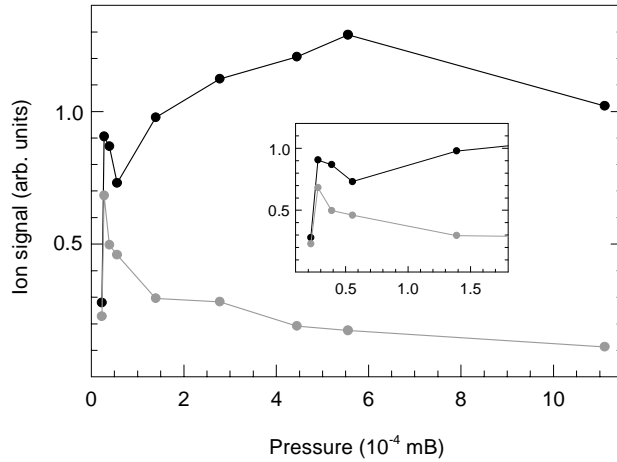


Figure 6.4: The He^+ ion signal as a function of pressure on- (black) and off-spike (grey), respectively

The observed pressure-dependent characteristics of the decay curves and the harmonic spectral profile can be explained by an enhanced absorption of the harmonic by the He gas, combined with an AC Stark broadening [52] of the $1s2p$ state at zero time delay where the probe is present. The absorption arises from the propagation of the harmonic through at least 15 cm of He gas, determined by the radius of the vacuum chamber. Only the spectral region corresponding to the unbroadened profile is affected by the absorption, and a "hole" is burned in the harmonic spectral profile. As a consequence, the ion signal is enhanced when the pump- and probe pulses overlap in time and exhibits a spike as a function of time delay. Assuming an ionization cross section at 355 nm of 16.6 Mb [36] and a probe intensity of 5×10^8 W/cm², the Stark contribution to the ionization width can be estimated to be 0.0056 nm, in very good agreement with the experimental observations. The probe pulse is expected to give rise to an AC Stark shift of the $1s2p$ level also, since the atomic ionization potential is known to be shifted up by the ponderomotive energy (cf. chapter 1), equivalent to 0.0005 nm in the present experiment. The higher-lying Rydberg levels shift upwards by approximately the same amount whereas the ground state is slightly downshifted [53]. With the He $1s2p$ level being intermediate between these limiting cases, the experimentally observed shift of 0.0003 nm may likely be in agreement with theory. The conditions necessary for the observation of the spike are thus: (i) a probe intensity sufficiently high to induce a significant broadening of the $1s2p$ level

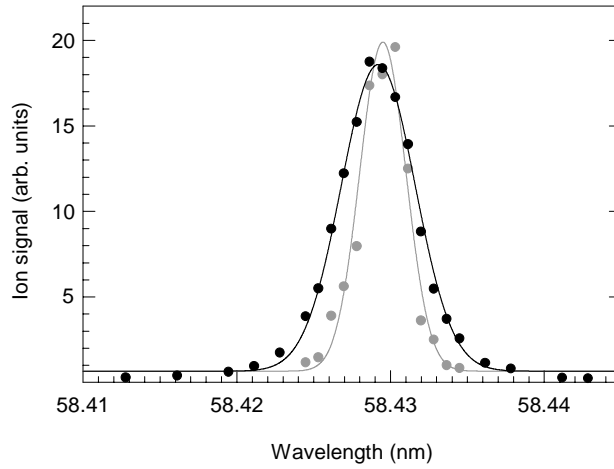


Figure 6.5: The apparent harmonic spectral profile on- (black) and off-spike (grey), respectively, for a He pressure of 6×10^{-4} mB.

(by saturating the ionization) and (ii) a significant absorption of the harmonic by the He gas medium.

The observations can be qualitatively accounted for by a rate-equation model where the He^+ signal $N_i(t)$ is calculated as a function of time delay t from a knowledge of the time-dependent population $N_r(t)$ of the $1s2p$ resonant level [54]. Rate equations are well known in atomic physics [18] and have previously been applied in studies of resonant two-photon ionization [55, 56] but without including the absorption, which plays the key role in the present context. $N_r(t)$ can be expressed in terms of the excitation rate $\Omega(t)$ from the ground state to the resonant level [52] which is assumed to be proportional to the "area" of the Lorentzian profile of the Stark-broadened atomic transition. The absorption from the harmonic during its propagation towards the interaction region is accounted for in a phenomenological way by multiplying the Stark-broadened Lorentzian profile with the exponential absorption factor of the Lambert-Beer law [24], using the wavelength-dependent field-free Lorentzian absorption cross section in the exponent. In this manner the time dependence of the Stark-broadening, following the time-dependent overlap between the harmonic and the probe, is transferred into a time-dependence of $\Omega(t)$. Neglecting the contribution to the ground-state population from the radiative decay, the rate equations to be solved are

$$\frac{dN_g}{dt} = -\Omega(t)N_g, \quad (6.3)$$

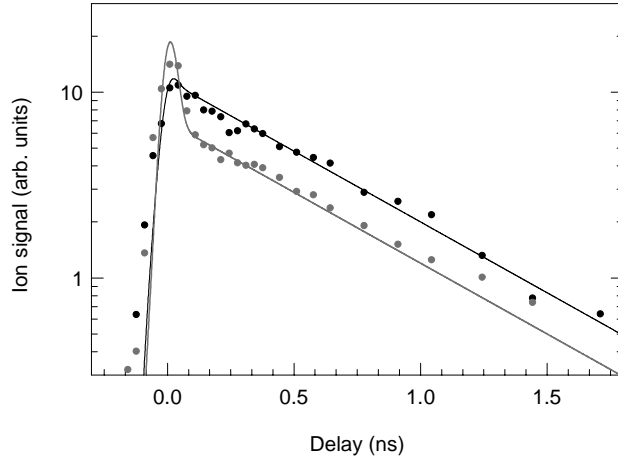


Figure 6.6: The two low-pressure decays from figure 6.3 together with theoretical predictions from a rate-equation model (solid curves).

$$\frac{dN_r}{dt} = \Omega(t)N_g - \Gamma_r^{\text{UV}}N_r - A_rN_r \quad (6.4)$$

and

$$\frac{dN_i}{dt} = \Gamma_r^{\text{UV}}N_r, \quad (6.5)$$

where Γ_r^{UV} is the intensity- and thus time-dependent ionization width of the resonant level, $A_r = 0.57$ ns the radiative lifetime and N_g the ground state population. As indicated above, $\Omega(t)$ is calculated as the "area" of the Stark-broadened, "hole-burned" Lorentzian atomic transition profile, multiplied by the Gaussian time-varying intensity of the harmonic. The $\Omega(t)$ obtained this way is used as the input to equation 6.3 which is solved to get $N_g(t)$. $N_g(t)$ and $\Omega(t)$ are inserted into equation 6.4 which is solved numerically with respect to $N_r(t)$. Finally, $N_r(t)$ is inserted into equation 6.5 from which $N_i(t)$ is obtained.

Preliminary results from the application of this procedure for pressures of 5×10^{-8} and 1×10^{-4} mB are shown as the black- and grey solid curves in figure 6.6, respectively. By normalizing the low-pressure theoretical curve to the decay curve measured at 6×10^{-5} mB, the best agreement of the high-pressure theoretical curve (in terms of the on- to off-spike ion signal level) was found with the decay curve measured at 1×10^{-4} mB, as indicated in the figure. The development of the spike is predicted by the rate-equation model

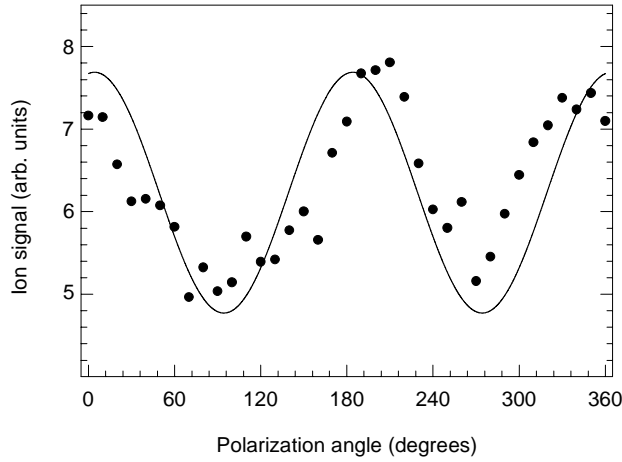


Figure 6.7: The He^+ ion signal as a function of angle of polarization between the pump and the probe for a pressure of 6×10^{-5} mB. The theoretically predicted cross section is indicated by the solid curve.

to occur at somewhat lower pressure ($\sim 10^{-7}$ mB) than found experimentally. The model may need some fine adjustment—for example, the Stark shift of the $1s2p$ level has been assumed to be equal to the ponderomotive energy—but it is evidently capable of predicting the essential features in the decay. It should be noted that without taking the absorption, or hole-burning, into account the spike cannot be reproduced unless an artificially high probe intensity (several times saturation) is used in the model. Finally, it remains to be checked how closely the pressure dependence of the ion signal measured on- and off spike, as given in figure 6.4, is reproduced by the model. The influence of radiation trapping and pressure broadening [25, 26] can be considered insignificant in the present experiment due to the low harmonic photon flux and given the pressure-independent slopes of the decay curves in figure 6.3.

6.3.2 Photoionization cross-section measurements

Concurrently with the spike investigations discussed above, experiments were performed to show that relative partial photoionization cross sections of the $1s2p$ state could be determined by varying the angle between the pump- and probe polarization vectors. The measurements presented below were obtained with the time delay fixed at 0.23 ns and at a pressure of 6×10^{-5} mB in order to minimize an eventual influence from the spike. By conservation of angular

momentum, single-photon ionization from the He $1s2p\ ^1P_1$ state, leaving the He⁺ ion in the $1s\ ^2S_{1/2}$ ground state, leads to the emission of either an s - or d -wave electron, corresponding to a total final-state momentum of 1S_0 or 1D_2 , respectively. The total cross section can be shown theoretically to be given by

$$\sigma(\theta) = \sigma_s + \sigma_d + 2 \left(\sigma_s + \frac{1}{10}\sigma_d \right) P_2(\cos\theta) \quad (6.6)$$

or

$$\sigma(\theta) = \frac{9}{10}\sigma_d + \left(\frac{3}{10}\sigma_d + 3\sigma_s \right) \cos^2\theta \quad (6.7)$$

$$= A + B\cos^2\theta, \quad (6.8)$$

with $A = \frac{9}{10}\sigma_d$ and $B = \frac{3}{10}\sigma_d + 3\sigma_s$ [57, 58]. Here $P_2(\cos\theta) = \frac{1}{2}(3\cos^2\theta - 1)$ is the second-order Legendre polynomial, θ the angle between the polarization vectors of the pump and the probe and σ_s (σ_d) the partial cross sections for s (d)-electron emission. Thus, by measuring (relatively) σ as a function of angle and fitting to the above expression to yield A and B , a value for the ratio $\sigma_d/\sigma_s = 10A/(3B - A)$ can be deduced. In principle, it suffices to measure the ion signal for two different angles, e.g. $\sigma_{\parallel} = \sigma(\theta = 0^\circ)$ and $\sigma_{\perp} = \sigma(\theta = 90^\circ)$, corresponding to parallel- and perpendicular polarizations, respectively. The ion signal N_i can be expressed in terms of the cross section as [36]

$$N_i \propto \int (1 - \exp(-\sigma_j R_{\text{probe}})) dV, \quad (6.9)$$

where R_{probe} is the space-dependent number of probe photons per cm² and $\sigma_j = \sigma_{\parallel}$ or σ_{\perp} . When measuring N_i as a function of angle, the cross section is most easily deduced if the probe-pulse energy is kept well below saturation such that $N_i \propto \sigma(\theta)$, assuming R_{probe} to be spatially constant across the interaction region. Due to the crossed-beam configuration the latter condition was, however, not fulfilled in the present experiment and, more importantly, the $\sigma(\theta)$ measurements were performed with a saturated probe-pulse energy. In spite of this, an attempt has been made in figure 6.7 to compare the measured angle-dependent ion signal with the theoretical curve given by equation 6.6, using the theoretically calculated ratio $\sigma_d/\sigma_s = 13/1$ [59]. The agreement is seen to be reasonable but the scatter among the data points does not allow a precise value for σ_d/σ_s to be extracted from a fit to equation 6.6;

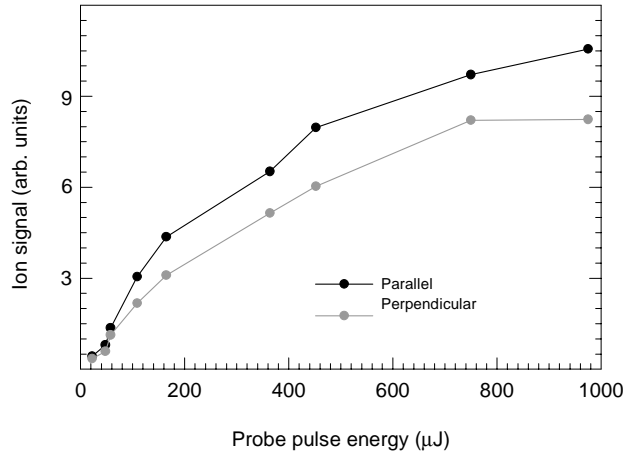


Figure 6.8: The He^+ ion signal as a function of probe-pulse energy for a pressure of 6×10^{-5} mB for parallel and perpendicular polarizations of the probe with respect to the pump.

the σ_d/σ_s ratio is too sensitive to the amplitude of the cosine modulation. Although the method works in principle it needs to be applied with much better statistics if quantitative results are to be obtained.

A plot of the ion signal as a function of probe-pulse energy is shown in figure 6.8 for parallel- (black) and perpendicular (grey) polarizations, respectively. The ion signal is seen to increase far beyond the probe-pulse saturation energy of $\sim 350 \mu\text{J}$, underlining the importance of accounting for the spatial variation of R_{probe} when evaluating the volume integral 6.9. From equation 6.6 a ratio $\sigma_{\parallel}/\sigma_{\perp} = 1.6$ is expected, assuming $\sigma_d/\sigma_s = 13/1$, which is in agreement with the experimental observations (figure 6.8). From similar saturation data the absolute cross sections (σ_{\parallel}) for ionization of the $1s2p$ and $1s3p$ states could be determined in [36] from a knowledge of the spatial variation of R_{probe} .

6.4 Conclusion

The usefulness of the two-colour pump-probe technique, using high-order harmonics, for lifetime- and photoionization cross-section measurements of excited states in the VUV has been demonstrated by measurements on the He $1s2p$ level. A spike present in the lifetime curves at zero time delay for pressures above 6×10^{-5} mB could be explained by a combination of absorp-

tion and Stark broadening of the $1s2p$ level. This effect was found to have no influence on the value of the lifetime measured but led to a reduced ion-signal level and should thus be avoided by working at low pressures.

An attempt was made to determine relative partial cross sections for ionization of the $1s2p$ level by measuring the ion signal as a function of the angle between the pump- and probe polarization vectors. The uncertainty on the data was, however, too large and the cross-section values to be deduced too sensitive to the scatter among the data points that quantitative results could be obtained. This situation might be improved by a more careful alignment of the setup and by minimizing and taking more carefully into account the fluctuations (on the order of 10–15 %) and drifts in laser-pulse energies.

The two-colour pump-probe technique has only been used for a limited number of experiments of the kind described above but could easily be applied for studies of many other systems. Also, the method should be considered a serious alternative to the pump-probe technique using synchronized laser- and synchrotron radiation pulses which has been applied for studies of resonances and many-body effects in atoms [60, 61, 62, 63]. In this respect the present method has the advantages of inherent synchronization of the pump- with the probe, a simplified setup and a competitive bandwidth—at least in the <40 eV range photon energy range (cf. chapter 1). This has been demonstrated in a study of autoionizing resonances of NO in the 11–12 eV photon energy region, using the 7th harmonic of the DFDL [64].

References

- [1] A. Dalgarno and S. Lepp, in *Atomic, Molecular and Optical Physics Handbook*, edited by G. W. F. Drake (AIP Press, New York, 1996).
- [2] C. Mendoza, *Physica Scripta* **T65**, 198 (1996).
- [3] K. A. Berrington, in *Astrophysical Applications of Powerful New Databases*, edited by S. J. Adelman and W. L. Wiese (ASP Conference Series, San Francisco, 1995), Vol. 78.
- [4] M. J. Seaton, *J. Phys. B* **20**, 6363 (1987).
- [5] K. A. Berrington *et al.*, *J. Phys. B* **20**, 6379 (1987).
- [6] H. Kjeldsen *et al.*, *Astrophys. J.* **524**, L143 (1999).
- [7] H. Kjeldsen *et al.*, *J. Phys. B* **33**, 1403 (2000).
- [8] E. Biémont *et al.*, *Physica Scripta* **16**, 39 (1977).
- [9] C. F. Fischer, *Physica Scripta* **T83**, 49 (1999).
- [10] T. Brage *et al.*, *J. Phys. B* **32**, 3183 (1999).
- [11] M.-K. Chen, *J. Phys. B* **27**, 865 (1994).
- [12] E. N. Avgoustoglou *et al.*, *Phys. Rev. A* **57**, 4286 (1998).
- [13] M. Masili *et al.*, *J. Phys. B* **33**, 2641 (2000).
- [14] S. J. Buckman, *Rev. Mod. Phys.* **66**, 539 (1994).
- [15] S. Johansson, in *Model Atmospheres and Spectrum Synthesis*, edited by S. J. Adelman and W. L. Wiese (ASP Conference Series, San Francisco, 1996), Vol. 108.

- [16] *Information available from the web-page "Spectroscopy in space"* (<http://violet.pha.jhu.edu/wpb/spectroscopy/space.html>, 2001).
- [17] M. C. E. Huber and R. J. Sandeman, *Rep. Prog. Phys.* **49**, 397 (1986).
- [18] P. W. Milonni and J. H. Eberly, *Lasers* (John Wiley & Sons, New York, 1988).
- [19] J. E. Lawler *et al.*, *Physica Scripta* **T47**, 29 (1993).
- [20] J. C. Pickering, *Physica Scripta* **T83**, 27 (1999).
- [21] R. Guenther, *Modern Optics* (John Wiley & Sons, New York, 1990).
- [22] I. I. Sobelman, *Atomic Spectra and Radiative Transitions* (Second Edition, Springer, Berlin, 1996).
- [23] J. Carlsson, *Physica Scripta* **39**, 442 (1989).
- [24] W. Demtröder, *Laser Spectroscopy, Basic Concepts and Instrumentation* (Springer, Berlin, 1998).
- [25] A. Thorne *et al.*, *Spectrophysics, Principles and Applications* (Springer, Berlin, 1999).
- [26] D. J. Chornay *et al.*, *J. Phys. B* **17**, 3173 (1984).
- [27] E. H. Pinnington, *Nucl. Inst. Meth. B* **9**, 549 (1985).
- [28] Z. Li *et al.*, *Eur. Phys. J. D* **2**, 11 (1998).
- [29] E. Biémont *et al.*, *Mont. Not. R. Astron. Soc.* **303**, 721 (1999).
- [30] W. Schade *et al.*, *Phys. Rev. A* **42**, 1454 (1990).
- [31] J. A. Aguilers *et al.*, *Phys. Rev. A* **45**, 2753 (1992).
- [32] P. Cacciani *et al.*, *Astrophys. J.* **499**, L223 (1998).
- [33] A. Gaupp *et al.*, *Phys. Rev. A* **26**, 3351 (1982).
- [34] W. I. McAlexander *et al.*, *Phys. Rev. A* **51**, R871 (1995).
- [35] Z. Li, *Time-Resolved Laser Spectroscopic Studies of Atoms, Ions and Molecules* (Ph.D. thesis, Department of Physics, Lund Institute of Technology, Sweden, 2000).
- [36] M. Gisselbrecht *et al.*, *Phys. Rev. Lett.* **82**, 4607 (1999).

-
- [37] J. Larsson *et al.*, J. Phys. B **28**, L53 (1995).
- [38] W. Ubachs *et al.*, Chem. Phys. **270**, 215 (2001).
- [39] C. E. Burkhardt *et al.*, Phys. Rev. A **38**, 5949 (1988).
- [40] L.-W. He *et al.*, Phys. Rev. Lett. **67**, 2131 (1991).
- [41] S. L. Gilbert *et al.*, Phys. Rev. A **29**, 3150 (1984).
- [42] H. Maeda and F. Ambe, Phys. Rev. A **56**, 3719 (1997).
- [43] R. Kau *et al.*, J. Phys. B **29**, 5673 (1996).
- [44] R. Kau *et al.*, J. Phys. B **31**, 1011 (1998).
- [45] S. Schohl *et al.*, J. Phys. B **30**, 609 (1997).
- [46] R. Kau *et al.*, Z. Phys. D **36**, 23 (1996).
- [47] R. Kau *et al.*, Z. Phys. D **39**, 267 (1997).
- [48] K. Mitsuke *et al.*, J. Phys. B **33**, 391 (2000).
- [49] W. Schade *et al.*, Appl. Opt. **29**, 3950 (1990).
- [50] C. Lyngå *et al.*, Appl. Phys. B **72**, 913 (2001).
- [51] Z. Bor *et al.*, Opt. Comm. **29**, 103 (1979).
- [52] A. L'Huillier *et al.*, J. Opt. Soc. Am. B **6**, 1790 (1989).
- [53] R. R. Freemann *et al.*, in *Atoms in Intense Laser Fields*, edited by M. Gavrilá (Academic Press, New York, 1992).
- [54] A. L'Huillier, private information (2001).
- [55] T. Freudenberg *et al.*, Z. Phys. D **36**, 349 (1996).
- [56] K. Johst and H. Johansen, Appl. Phys. B **48**, 479 (1989).
- [57] S. Baier *et al.*, J. Phys. B **27**, 3363 (1994).
- [58] M. Meyer, private information (1999).
- [59] T. N. Chang and T. K. Fang, Phys. Rev. A **52**, 2052 (1995).
- [60] D. Cubaynes *et al.*, Phys. Rev. Lett. **63**, 2460 (1989).
- [61] M. Wedowski *et al.*, Phys. Rev. A **55**, 1922 (1997).

- [62] S. Baier *et al.*, J. Phys. B **27**, 1341 (1994).
- [63] M. Gisselbrecht *et al.*, J. Phys. B **31**, L977 (1998).
- [64] P. Erman *et al.*, Chem. Phys. Lett. **239**, 6 (1995).

Summary

For an atom or molecule in the gas phase or at a solid surface, the spatial distributions of the electrons with respect to the nucleus and of the nuclei with respect to each other are reflected in the electronic-, vibrational- and rotational energies of the system. By the quantum-mechanical rules governing such a system, only certain (discrete) energies, so-called stationary states, are allowed, and the elucidation of these states and their stabilities, or lifetimes, is at the heart of atomic- and molecular spectroscopy. According to the Heisenberg uncertainty relation, the decay of a stationary excited state is associated with a broadening of the corresponding energy level. As a consequence, the stability of the state can be determined from a measurement of either the lifetime or the spectral width of the energy level.

Following an external, non-perturbative disturbance by, e.g., a light field, the nuclei of the atoms bound in a molecule or a solid may undergo a spatial re-arrangement, as reflected by a dynamical change in the energy-level diagram. A structural dynamical transition involves the breaking (and possible formation) of intra- or inter-molecular chemical bonds and proceeds on the atomic level on a femtosecond (10^{-15} s) time scale. Examples of such transitions are the dissociation of a molecule following its excitation to a repulsive state, a chemical reaction or a solid-liquid phase transition.

The present thesis is concerned with the spectroscopic investigations of electronically excited, stationary states of gas-phase atoms and -molecules, in particular negative ions, and of structural dynamical transitions of molecules bound to solid surfaces. A common element of most of these studies is the use of laser light in the vacuum-ultraviolet (VUV) part of the electromagnetic spectrum, i.e. the 10–200 nm wavelength range. The generation of light with a narrow spectral bandwidth or a femtosecond pulse duration, as required for the studies of the thesis, is not as straightforward in the VUV as in the visible regime. An overview of the present status of VUV light generation with emphasis on the present spectroscopic possibilities and limitations imposed by the quality of the light source is the subject of chapter 1.

The following three chapters are devoted to the spectroscopy of negative ions which are particularly interesting from an astrophysical- and a theoretical point of view. The structure, or energy-level diagram, of a negative ion is markedly different from that of a neutral atom or -molecule due to the correlation effects introduced by the presence of the extra electron. In general, only a single bound state exists but the single-electron continuum may reveal a rich structure of doubly-excited states, resonances, that are often associated with excited states of the corresponding neutral atom or -molecule. A doubly-excited state typically decays by electron emission in a process known as autodetachment, leaving the resulting neutral system in its ground state or a lower-lying excited state. In chapter 2 a general introduction to the properties of negative ions is given, including an overview of the present knowledge obtained from spectroscopic studies and the theoretical approaches currently applied to model their structure.

An experimental technique for Doppler-tuned VUV spectroscopy of high-lying doubly-excited states of the fundamental negative-ion system H^- , has previously been implemented at the storage ring ASTRID. In these studies use was made of a fixed-frequency VUV light source based on the non-linear frequency-upconversion of visible laser light by a process known as harmonic generation. The unprecedented spectral resolution achieved with this technique has allowed the observation of previously un-resolved resonances and has recently been improved by the application of the electron cooler of the storage ring. This has allowed the first precise measurement of the spectral width of one of these resonances, providing the first critical test of a number of theoretical models as described in chapter 3.

The ASTRID storage ring has also previously been successfully used for lifetime measurements of metastable, doubly-excited, autodetaching states of atomic negative ions with lifetimes in the μs – ms range. The spectral widths of such states are too narrow that they can be resolved by ordinary laser-spectroscopic methods. In the storage ring the ions are allowed to circulate for several lifetimes, facilitating a precise measurement of the decay rate as a function of time. In the experiments described in chapter 4 this method has been applied to lifetime measurements on unknown metastable states of N_2^- and CO_2^- which do not exist as stable ground-state ions. By a co-operation with theorists, the lifetimes observed have been assigned to a previously un-explored class of high-spin negative-ion states.

The focus of chapter 5 is on the construction of an experimental setup aiming at studies of structural dynamical processes at surfaces with a femtosecond time resolution. Emphasis is given to chemical reactions of gas-phase molecules which are enhanced, or catalyzed, by the presence of the surface, in particular to the desorption step, by which the product molecules escape

from the surface. A source of femtosecond X-rays would allow such processes to be followed on the atomic level simultaneously in time as well as in space, but is at present not readily available. In the present setup the claim for a femtosecond time resolution has been maintained and the spatial resolution relaxed by combining the traditional surface-science technique of X-ray core-level spectroscopy with a femtosecond VUV light source based on the process of high-harmonic generation. Following an introduction to the field of laser-induced desorption and the technique of core-level spectroscopy, a description of some of the preparations needed prior to the femtosecond VUV core-level spectroscopic studies is given. These have included the (static) core-level spectroscopic measurements at a synchrotron-radiation beamline at ASTRID of the CO-covered Pt- and the O-covered Al surfaces, showing the O/Al system to be most suitable for the future femtosecond laser-induced desorption experiments. In a subsequent section the generation and optimization of the VUV light source of high-order harmonics is reported, and the chapter is concluded with a description of the future setup and its possibilities.

In the final chapter 6 a laser-spectroscopic study of the lifetime of the excited $1s2p$ state of He is described. The $1s2p$ state was excited and subsequently ionized with VUV- and visible laser pulses, respectively, and the lifetime was measured by scanning the time delay between the light pulses. The emphasis of the experiment was not on the all-ready well-known lifetime but on some coherent ionization effects present under sufficiently high He-gas pressures. These effects could be explained by an enhanced absorption of the VUV light by the He gas, combined with a Stark-broadening of the $1s2p$ state implied by the high intensity of the visible laser beam.